
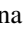


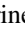
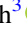
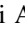
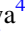
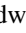




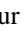
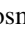






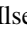


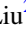
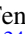

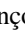

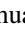


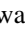

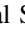

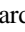





# Molecules with ALMA at Planet-forming Scales (MAPS). I. Program Overview and Highlights

Karin I. Öberg<sup>1</sup> , Viviana V. Guzmán<sup>2</sup> , Catherine Walsh<sup>3</sup> , Yuri Aikawa<sup>4</sup> , Edwin A. Bergin<sup>5</sup> , Charles J. Law<sup>1</sup> , Ryan A. Loomis<sup>6</sup> , Felipe Alarcón<sup>5</sup> , Sean M. Andrews<sup>1</sup> , Jaehan Bae<sup>7,8,27</sup> , Jennifer B. Bergner<sup>9,27</sup> , Yann Boehler<sup>10</sup> , Alice S. Booth<sup>3,11</sup> , Arthur D. Bosman<sup>5</sup> , Jenny K. Calahan<sup>5</sup> , Gianni Cataldi<sup>4,12</sup> , L. Ilesdore Cleeves<sup>13</sup> , Ian Czekala<sup>14,15,16,17,18,27</sup> , Kenji Furuya<sup>12</sup> , Jane Huang<sup>1,5,27</sup> , John D. Ilee<sup>3</sup> , Nicolas T. Kurtovic<sup>19,20</sup> , Romane Le Gal<sup>1,10,21,22</sup> , Yao Liu<sup>23</sup> , Feng Long<sup>1</sup> , François Ménard<sup>10</sup> , Hideko Nomura<sup>12</sup> , Laura M. Pérez<sup>19</sup> , Chunhua Qi<sup>1</sup> , Kamber R. Schwarz<sup>24,27</sup> , Anibal Sierra<sup>19</sup> , Richard Teague<sup>1</sup> , Takashi Tsukagoshi<sup>12</sup> , Yoshihide Yamato<sup>4</sup> , Merel L. R. van 't Hoff<sup>5</sup> , Abygail R. Waggoner<sup>25</sup> , David J. Wilner<sup>1</sup> , and Ke Zhang<sup>5,26,28</sup> 

<sup>1</sup> Center for Astrophysics | Harvard & Smithsonian, 60 Garden St., Cambridge, MA 02138, USA; [koberg@cfa.harvard.edu](mailto:koberg@cfa.harvard.edu)

<sup>2</sup> Instituto de Astrofísica, Pontificia Universidad Católica de Chile, Av. Vicuña Mackenna 4860, 7820436 Macul, Santiago, Chile

<sup>3</sup> School of Physics and Astronomy, University of Leeds, Leeds, LS2 9JT, UK

<sup>4</sup> Department of Astronomy, Graduate School of Science, The University of Tokyo, Tokyo 113-0033, Japan

<sup>5</sup> Department of Astronomy, University of Michigan, 323 West Hall, 1085 S. University Ave., Ann Arbor, MI 48109, USA

<sup>6</sup> National Radio Astronomy Observatory, 520 Edgemont Rd., Charlottesville, VA 22903, USA

<sup>7</sup> Earth and Planets Laboratory, Carnegie Institution for Science, 5241 Broad Branch Road NW, Washington, DC 20015, USA

<sup>8</sup> Department of Astronomy, University of Florida, Gainesville, FL 32611, USA

<sup>9</sup> University of Chicago, Department of the Geophysical Sciences, Chicago, IL 60637, USA

<sup>10</sup> Univ. Grenoble Alpes, CNRS, IPAG, F-38000 Grenoble, France

<sup>11</sup> Leiden Observatory, Leiden University, 2300 RA Leiden, The Netherlands

<sup>12</sup> National Astronomical Observatory of Japan, 2-21-1 Osawa, Mitaka, Tokyo 181-8588, Japan

<sup>13</sup> Department of Astronomy, University of Virginia, Charlottesville, VA 22904, USA

<sup>14</sup> Department of Astronomy and Astrophysics, 525 Davey Laboratory, The Pennsylvania State University, University Park, PA 16802, USA

<sup>15</sup> Center for Exoplanets and Habitable Worlds, 525 Davey Laboratory, The Pennsylvania State University, University Park, PA 16802, USA

<sup>16</sup> Center for Astrostatistics, 525 Davey Laboratory, The Pennsylvania State University, University Park, PA 16802, USA

<sup>17</sup> Institute for Computational & Data Sciences, The Pennsylvania State University, University Park, PA 16802, USA

<sup>18</sup> Department of Astronomy, 501 Campbell Hall, University of California, Berkeley, CA 94720-3411, USA

<sup>19</sup> Departamento de Astronomía, Universidad de Chile, Camino El Observatorio 1515, Las Condes, Santiago, Chile

<sup>20</sup> Max-Planck-Institut für Astronomie, Königstuhl 17, D-69117, Heidelberg, Germany

<sup>21</sup> IRAP, Université de Toulouse, CNRS, CNES, UT3, 31400 Toulouse, France

<sup>22</sup> IRAM, 300 rue de la piscine, F-38406 Saint-Martin d'Hères, France

<sup>23</sup> Purple Mountain Observatory & Key Laboratory for Radio Astronomy, Chinese Academy of Sciences, Nanjing 210023, People's Republic of China

<sup>24</sup> Lunar and Planetary Laboratory, University of Arizona, 1629 E. University Blvd., Tucson, AZ 85721, USA

<sup>25</sup> Department of Chemistry, University of Virginia, Charlottesville, VA 22904, USA

<sup>26</sup> Department of Astronomy, University of Wisconsin–Madison, 475 N. Charter St., Madison, WI 53706, USA

Received 2021 February 14; revised 2021 May 31; accepted 2021 June 3; published 2021 November 3

## Abstract

Planets form and obtain their compositions in dust- and gas-rich disks around young stars, and the outcome of this process is intimately linked to the disk chemical properties. The distributions of molecules across disks regulate the elemental compositions of planets, including C/N/O/S ratios and metallicity (O/H and C/H), as well as access to water and prebiotically relevant organics. Emission from molecules also encodes information on disk ionization levels, temperature structures, kinematics, and gas surface densities, which are all key ingredients of disk evolution and planet formation models. The Molecules with ALMA at Planet-forming Scales (MAPS) ALMA Large Program was designed to expand our understanding of the chemistry of planet formation by exploring disk chemical structures down to 10 au scales. The MAPS program focuses on five disks—around IM Lup, GM Aur, AS 209, HD 163296, and MWC 480—in which dust substructures are detected and planet formation appears to be ongoing. We observed these disks in four spectral setups, which together cover ~50 lines from over 20 different species. This paper introduces the Astrophysical Journal Supplement's MAPS Special Issue by presenting an overview of the program motivation, disk sample, observational details, and calibration strategy. We also highlight key results, including discoveries of links between dust, gas, and chemical substructures, large reservoirs of nitriles and other organics in the inner disk regions, and elevated C/O ratios across most disks. We discuss how this collection of results is reshaping our view of the chemistry of planet formation.

*Unified Astronomy Thesaurus concepts:* [Astrochemistry \(75\)](#); [Protoplanetary disks \(1300\)](#); [Planet formation \(1241\)](#); [Astrobiology \(74\)](#); [Millimeter astronomy \(1061\)](#); [Submillimeter astronomy \(1647\)](#)

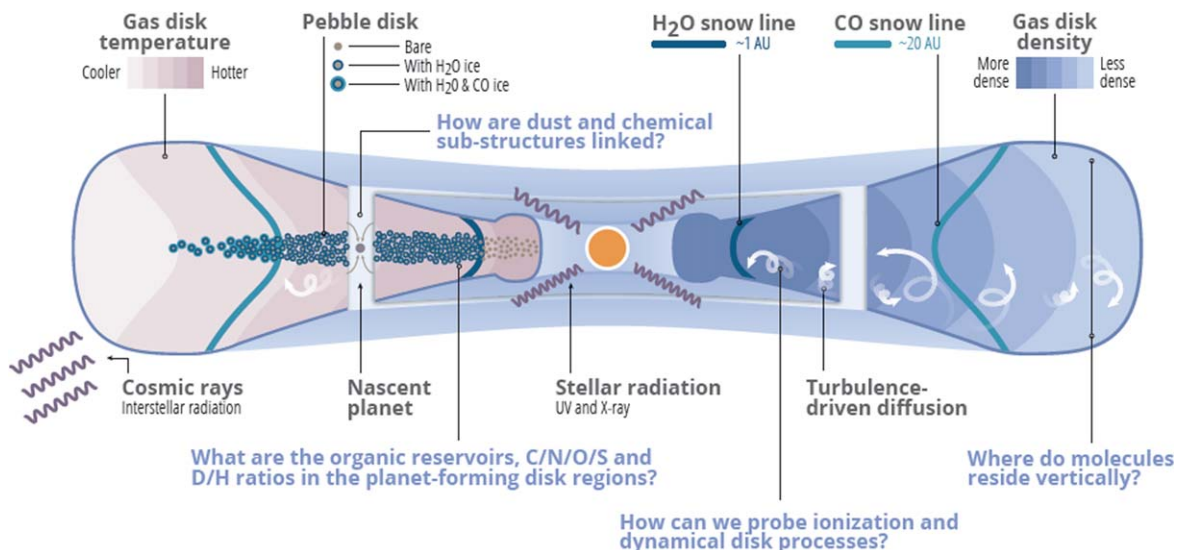
## 1. Introduction: The Chemistry of Planet Formation

Planets form in disks of dust and gas around young stars. The distributions of volatile elements and organics in these disks

affect multiple aspects of planet formation (see Henning & Semenov 2013; Dutrey et al. 2014; Pontoppidan et al. 2014; Öberg & Bergin 2021, for recent reviews). Radial and vertical chemical gradients may impact where in disks planets form, planet formation efficiencies, planet elemental and organic compositions, and the isotopic ratios in planets and planetesimals. Furthermore,

<sup>27</sup> NASA Hubble Fellowship Program Sagan Fellow.

<sup>28</sup> NASA Hubble Fellow.



**Figure 1.** Illustration of the protoplanetary disk structure on a logarithmic scale and its coupling to different gas and grain dynamical processes. Note the temperature gradient inward and upward (pink shading), which results in a series of midplane snow lines (shown at typical locations for a disk around a T Tauri star) and 2D snow surfaces reaching up into the disk atmosphere, as well as the inward and downward density gradient (blue shading). Disk surfaces are characterized by photon processes. Disk midplanes are, by contrast, cold and UV-poor, and the main volatile reservoirs (other than  $\text{H}_2$  and He) are in icy grain and pebble mantles, especially exterior to the CO snow line. The four guiding questions used to design MAPS are written in blue. Image credit: K. Peek, adapted from Öberg & Bergin (2021).

molecular line observations often provide the best, and sometimes our only, probes of disk characteristics relevant to planet formation, such as surface density, ionization, temperature, metallicity, C/N/O/S ratios, and disk kinematics. The overall goal of the Molecules with ALMA at Planet-forming Scales (MAPS) Large Program is to use high spatial resolution observations of a large number of molecular lines to promote a deeper understanding of the links between chemistry and planet formation in protoplanetary disks.

The context within which MAPS was conceived is our current understanding of the structure, dynamics, and chemistry of protoplanetary disks, as illustrated in Figure 1. Globally, protoplanetary disks are characterized by radial and vertical gradients in temperature, density, ionization, and radiation fields (e.g., van Zadelhoff et al. 2001; Dartois et al. 2003; Kamp & Dullemond 2004; Meijerink et al. 2012; Woitke et al. 2016). These disk characteristics are important in their own right; ionization levels, surface densities, and temperature gradients are all key players in planet formation models (e.g., Baruteau et al. 2016; Mordasini et al. 2016). They also regulate the distribution, formation, and destruction of molecules in disks. For the purpose of introducing the disk chemistry most relevant to MAPS, we will treat these gradients as static. It is, however, important to note that protoplanetary disks are dynamical objects and that this can have a large impact on the distribution of molecules (e.g., Willacy 2007; Semenov & Wiebe 2011; Akimkin et al. 2013; Rab et al. 2017; Price et al. 2020). Globally, these accretion disks spread and deplete mass onto the star over time (Lynden-Bell & Pringle 1974; Hartmann et al. 2016). Within the disks, accretion flows transport gas and entrained grains both inward and outward, while grain settling and drift transport solids toward the midplane and pressure maxima, and turbulence may mix gas and grains vertically and radially (Weidenschilling & Cuzzi 1993; Hartmann 2000; Birnstiel et al. 2012).

Of the disk properties illustrated in Figure 1, temperature gradients have long been of special interest. Radial temperature gradients are expected to produce a sequence of condensation fronts or snow lines, where abundant volatiles transition from gas to ice, in the planet-forming midplane (Lewis 1974;

Hayashi 1981; Qi et al. 2013; van 't Hoff et al. 2017; Qi et al. 2019). These snow lines may impact the planet formation efficiency (e.g., Lewis 1974). At the snow lines, dust coagulation properties change with changing grain compositions (Dominik & Tielens 1997; Güttler et al. 2010; Wada et al. 2013; Gundlach & Blum 2015; Pinilla et al. 2017), while rapid disintegration of pebbles crossing the snow line results in traffic jams (Birnstiel et al. 2010), and diffusive flows across snow lines result in large reservoirs of solids directly outside of the snow line location (Stevenson & Lunine 1988; Ciesla & Cuzzi 2006; Ros & Johansen 2013). Snow lines may also regulate the elemental compositions of planets and planetesimals (e.g., Whipple 1972; Lewis 1974; Öberg et al. 2011a; Piso et al. 2016). Because major carriers of common volatiles freeze out at different temperatures, C, O, N, and S are expected to deplete out of the gas at different disk radii, resulting in a sequential change in solid and gas composition. This should, in turn, translate into a dependence of planet core and atmosphere elemental composition on assembly location (e.g., Helling et al. 2014; Cridland et al. 2020). It is worth noting that a combination of observations and theory suggest that the nature of the major carriers may change over time, especially due to the conversion of CO into other molecules (Favre et al. 2013; Reboussin et al. 2015; Yu et al. 2017; Bosman et al. 2018; Dodson-Robinson et al. 2018; Schwarz et al. 2018).

Condensation fronts also exist in the vertical dimension, resulting in 2D snow surfaces (Aikawa et al. 2002; van 't Hoff et al. 2017; Qi et al. 2019), due to vertical temperature gradients. The vertical temperature structure is set by a combination of attenuating radiation from the central star, chemical feedback on heating and cooling, and, in the inner disk, accretion (e.g., D'Alessio et al. 1999; Woitke et al. 2009), but it is also sensitive to dust growth and settling to the midplanes (e.g., D'Alessio et al. 2006; Tilling et al. 2012). The changing elemental ratios across the resulting snow surfaces are expected to induce chemical gradients due to changing gas-phase and grain-surface elemental inventories.

The vertical chemical structure is also strongly influenced by gradients in UV radiation and other ionizing agents (e.g., Aikawa & Herbst 2001; Bergin et al. 2003; Semenov et al. 2006; Dutrey et al. 2007; Nomura et al. 2007; Willacy 2007; Woitke et al. 2009; Walsh et al. 2010; Kamp et al. 2010; Fogel et al. 2011; Cazzoletti et al. 2018), because many chemical reactions are regulated by either UV photodissociation or ion–molecule reactions. The ionization structures of disks depend on a combination of UV and X-ray disk surface fluxes and their radiative transfer, as well as on cosmic-ray ionization (Glassgold et al. 1997; Cleeves et al. 2014a; Drabek-Maunder et al. 2016; Woitke et al. 2016; Rab et al. 2018). The total UV flux further depends on a combination of stellar UV radiation, UV from accretion shocks, and external UV fields. Because of the important role of UV radiation, disk atmospheres have sometimes been described as analogs to photon-dominated regions (PDRs), where different molecular photodissociation cross sections determine the molecular emitting layers (e.g., van Dishoeck et al. 2006; Agúndez et al. 2018; Cazzoletti et al. 2018).

Millimeter and submillimeter astronomy has been used since the late 1980s to explore disk molecular lines and the underlying disk chemistry (e.g., Weintraub et al. 1989; Koerner et al. 1993; Dutrey et al. 1997; Kastner et al. 1997; Thi et al. 2004). Spatially and spectrally resolved molecular line observations enable us to trace radial disk chemical structures (see Dutrey et al. 2007; Qi et al. 2008; Henning et al. 2010, for pioneering work). Over the past cycles, observations with the Atacama Large Millimeter/submillimeter Array (ALMA) have been used to characterize the CO gas abundance, identify CO snow lines, and map out gradients in other abundant volatiles and organic molecules (e.g., Qi et al. 2013; Du et al. 2015; Öberg et al. 2015a; Bergin et al. 2016; Schwarz et al. 2016; Walsh et al. 2016; Miotello et al. 2017; Zhang et al. 2017; Cleeves et al. 2018; Kastner et al. 2018; Loomis et al. 2018a; Semenov et al. 2018; Le Gal et al. 2019a; Tsukagoshi et al. 2019; van Terwisga et al. 2019; Zhang et al. 2020; Facchini et al. 2021; Nomura et al. 2021; Rosotti et al. 2021). Millimeter observations of edge-on disks present perhaps the most straightforward path toward characterizing vertical chemical gradients (Dutrey et al. 2017; Louvet et al. 2018; Podio et al. 2020; Teague et al. 2020; van ’t Hoff et al. 2020), but vertical chemical structures are also accessible in moderately inclined disks (Piétu et al. 2007; Semenov et al. 2008; Rosenfeld et al. 2013; Pinte et al. 2018b; Paneque-Carreno et al. 2021; Rich et al. 2021), such as the ones pursued in this program.

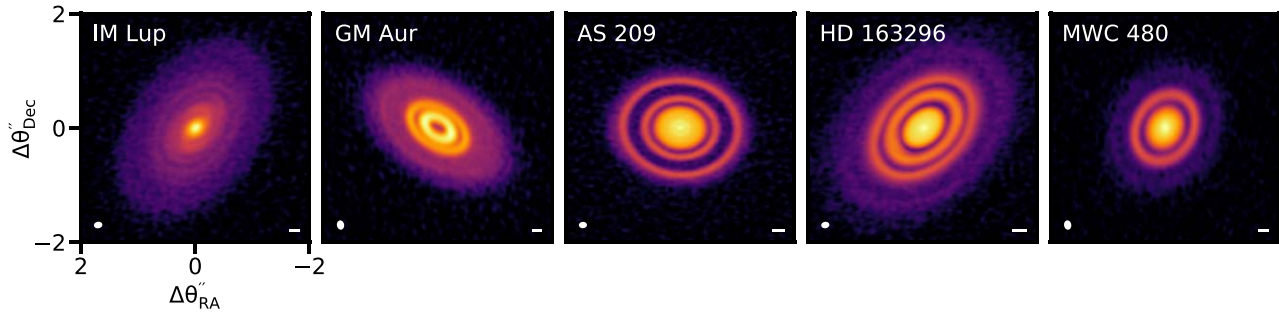
Most disk chemistry observations have been confined to angular scales of  $\gtrsim 0''.5$  or 50–75 au (at a source distance of 100–150 pc), which has made it difficult to directly connect observed chemical structures with the material feeding planet formation. We note that the precise molecular inventory on small scales is especially interesting when considering how disk chemistry may impact the volatile composition of temperate, Earth-like planets where the subsequent chemistry may result in the development of life. While we do not know how life originated on Earth, nitriles and other small, reactive organics are implicated in several origins-of-life scenarios (Powner et al. 2009; Patel et al. 2015; Pearce et al. 2017), and their distributions in the inner regions of disks are of special interest. To assess the molecular inventory in the disk regions most commonly associated with planet formation (Pollack et al. 1996) requires high-resolution observations.

Higher spatial resolution observations are also needed to explore the relationship between dust and chemical substructures. One of the great discoveries in protoplanetary disk science in the

past decade is that disks frequently display substructures—rings, gaps, spirals, and clumps—in millimeter continuum emission, tracing the distribution of small pebbles (e.g., ALMA Partnership et al. 2015; Andrews et al. 2016, 2018; Huang et al. 2018b; Long et al. 2018; Andrews 2020; Cieza et al. 2021). The observed gaps have often been connected to ongoing planet formation (e.g., Flock et al. 2015; Fedele et al. 2017; Keppler et al. 2019), though other plausible explanations exist as well (see Andrews 2020, for a review). Existing observations suggest that the distribution of dust can be important for explaining and predicting the distribution of different molecules. In particular, the edges of pebble disks are sometimes associated with dramatic changes in the molecular line emission pattern (e.g., Öberg et al. 2015a; Bergin et al. 2016). Similarly, observations of bright HCO<sup>+</sup> emission in the large gaps associated with transition disks indicate high gas-to-millimeter-grain ratios compared to their surroundings, which should result in chemically distinct disk regions (e.g., Drabek-Maunder et al. 2016; Huang et al. 2020). Together with model predictions (e.g., Facchini et al. 2018; van der Marel et al. 2018; Alarcón et al. 2020), these observations suggest that dust and pebble gaps may cause observable chemical changes. This chemical response to the opening of pebble gaps in the disk will determine the local chemical environment within which massive gap-opening planets form.

In addition to providing direct measures of chemical abundances, molecular lines provide constraints on the elemental composition, surface density, temperature, ionization, and kinematics of disk gas (some recent examples can be found in van der Marel et al. 2016; Dutrey et al. 2017; Flaherty et al. 2017; Miotello et al. 2017; Huang et al. 2018a; Pinte et al. 2018b; and Calahan et al. 2021; but see also the reviews above for references to earlier work). Some of these molecular probes work because some molecular abundances sensitively depend on C/N/O/S ratios, “metallicity” (C/H and O/H ratios), disk ionization, UV radiation, density, temperature, and D/H levels. Elemental ratios and gas metallicity are, for example, expected to affect the ratios of common disk molecules such as C<sub>2</sub>H/CO, CS/SO, and HCN/CO, as well as the abundances of more complex molecules like CH<sub>3</sub>CN (Du et al. 2015; Cleeves et al. 2018; Semenov et al. 2018; Le Gal et al. 2019b; Miotello et al. 2019), while other molecular pairs are proposed to be sensitive to ionization (HCO<sup>+</sup>/CO) or UV (CN/HCN) (Bergin et al. 2003; Teague et al. 2015). Molecular isotopologues are proposed to be especially powerful diagnostics (Ceccarelli et al. 2014). Deuterium enhancements are commonly used to trace the origins of solar system volatiles, but these conclusions currently depend largely on theoretical expectations of D/H levels in volatiles in disks (e.g., Aikawa & Herbst 1999, 2001; Willacy 2007; Willacy & Woods 2009; Cleeves et al. 2014b, 2016a). A few resolved observational studies have helped elucidate important drivers for deuterium chemistry (e.g., Öberg et al. 2012; Mathews et al. 2013; Huang et al. 2017; Salinas et al. 2017; Carney et al. 2018; Öberg et al. 2021), but the distribution of D/H in the planet-forming disk regions is still largely unknown.

Molecular emission lines are also potential probes of disk gas masses and gas surface densities (e.g., Williams & Best 2014; Miotello et al. 2016; Molyarova et al. 2017) and can be used to constrain what types of planetary systems could form in disks (e.g., Rab et al. 2020). Molecular emission may also constitute our best tool to characterize how and where planets form in disks. Observations of molecular lines are key to characterizing the distribution and dynamics of gas in disks



**Figure 2.** The 220 GHz continuum images from MAPS displaying the diversity of continuum structure present at the same spatial resolutions as probed by the MAPS molecular lines. The images are shown with an *arcsinh* color stretch, which accentuates low surface brightness features. The synthesized beams are indicated in the bottom left corner and a 20 au scale bar in the bottom right corner of each panel. See Law et al. (2021a) and Sierra et al. (2021) for a detailed presentation and analysis of these images.

(e.g., Dartois et al. 2003; Isella et al. 2007; Rosenfeld et al. 2012). More specifically, spatially and spectrally resolved lines can be used to identify chemical and kinematic signatures of planets in the making (e.g., Cleves et al. 2015; Kanagawa et al. 2015; Perez et al. 2015; Pinte et al. 2018b; Teague et al. 2018a; Dong et al. 2019; Tsukagoshi et al. 2019; Nomura et al. 2021). This is an exciting new development, since direct planet detections in disks remain rare (Keppler et al. 2018; Wang et al. 2021).

With this background in mind, we designed MAPS to address the following goals (see also Figure 1):

1. to assess the relationship between dust substructures and gas and chemical substructures in disks;
2. to constrain the emitting heights of observed molecules and assess how well we probe planet-forming layers;
3. to take astrochemistry studies into the planet-forming disk regions and address the C/N/O/S ratios, deuterium fractionation, and organic compositions at scales down to 10 au; and
4. to constrain disk dynamics, temperatures, gas surface densities, and ionization across disks, especially in disk gaps and rings, using a variety of molecular probes.

This paper introduces the special issue of the *Astrophysical Journal Supplement* reporting our results from MAPS, including both analysis of the ALMA data and models aimed at providing an interpretive framework. In particular, the purpose of this paper is to present the MAPS observational program, introduce the other papers in the special issue, and discuss how the results of the individual MAPS papers are advancing our understanding of disk chemistry and its relationship to planet formation. In Section 2, we describe and motivate the disk sample and the lines targeted with MAPS. Section 3 presents the observations, our calibration strategy, and a brief summary of the imaging strategy. The latter is described in detail in Czekala et al. (2021). Section 4 provides an overview of the results presented in the MAPS papers in this special issue of the *Astrophysical Journal Supplement*, while Section 5 discusses how this ensemble of results has changed our view of the chemistry of planet formation, and Section 6 provides a brief summary and some concluding remarks.

## 2. MAPS Disks and Lines

### 2.1. MAPS Disk Sample

The MAPS sample consists of five disks that were selected to achieve a diversity of dust substructures and stellar

properties and ensure line detections. In brief, we selected the sample based on the following considerations.

1. The sample should include both T Tauri and Herbig Ae stars to explore the role of the stellar luminosity and radiation field on disk chemistry.
2. The sample should include different kinds of dust substructures to enable identifications of links between dust and chemical substructures.
3. No disks should be substantially obscured by cloud material or include substantial envelope emission that would complicate the interpretation of line observations.
4. All disks should have been previously observed in at least a subset of the targeted molecular lines.

Practically, we selected the MAPS disk sample by first identifying sources that had resolved continuum observations at  $\sim 0''.1$  or better with ALMA and that had been included in disk chemistry-related observational programs with the Plateau de Bure Interferometer (PdBI), the Northern Extended Millimeter Array (NOEMA), the Submillimeter Array (SMA), or ALMA (Dutrey et al. 2007; Öberg et al. 2010, 2011b; Huang et al. 2017; Bergner et al. 2018). We first explored the disks observed within the ALMA Large Program DSHARP (Andrews et al. 2018), and five of the DSHARP disks met our criteria. Of these, we selected two disks around T Tauri stars (IM Lup and AS 209) and one around a Herbig Ae star (HD 163296) based on their diversity of dust substructures. We supplemented this sample with an additional disk around the Herbig Ae star MWC 480, whose continuum was characterized by Long et al. (2018), and a transition disk (a disk with a large inner gap or cavity) around the T Tauri star GM Aur, which was recently observed at high resolution by Huang et al. (2020).

The resulting MAPS sample consists of three T Tauri (IM Lup, AS 209, and GM Aur) and two Herbig Ae (HD 163296 and MWC 480) star-disk systems. All disks have dust gaps and rings, but the nature of these gaps and rings varies substantially among the five disks (Andrews et al. 2018; Huang et al. 2018b, 2020; Long et al. 2018), as illustrated in Figure 2. Additional dust features include a large central gap in the GM Aur disk, spiral arms in the IM Lup disk (Huang et al. 2018c), a clear dust asymmetry in the HD 163296 disk (Isella et al. 2018), and faint extended dust emission beyond the bright outermost disk ring toward GM Aur, IM Lup, and HD 163296. The sample star and disk properties are summarized in Table 1. In particular, Table 1 lists stellar spectral types, masses, effective temperatures, luminosities, approximate ages, accretion rates, and Gaia distances; disk inclinations and position angles; and source

**Table 1**  
Stellar and Disk Properties

Source	Spectral Type	Dist. <sup>a</sup> (pc)	Incl. (deg)	PA (deg)	$T_{\text{eff}}$ (K)	$L_*$ <sup>b</sup> ( $L_{\odot}$ )	Age <sup>c</sup> (Myr)	$M_*$ <sup>d</sup> ( $M_{\odot}$ )	$\log_{10}(\dot{M})^b$ ( $M_{\odot} \text{ yr}^{-1}$ )	$v_{\text{sys}}$ ( $\text{km s}^{-1}$ )	References
IM Lup	K5	158	47.5	144.5	4266	2.57	~1	1.1	-7.9	4.5	1, 2, 3, 4, 5, 12
GM Aur	K6	159	53.2	57.2	4350	1.2	~3-10	1.1	-8.1	5.6	1, 6, 7, 8, 9, 10, 11
AS 209	K5	121	35.0	85.8	4266	1.41	~1-2	1.2	-7.3	4.6	1, 2, 12, 13, 14
HD 162396	A1	101	46.7	133.3	9332	17.0	$\gtrsim 6$	2.0	-7.4	5.8	1, 2, 12, 15, 16
MWC 480	A5	162	37.0	148.0	8250	21.9	~7	2.1	-6.9	5.1	1, 17, 18, 19, 20, 21

#### Notes.

<sup>a</sup> Gaia DR2 distances, which were adopted because DR3 distances were not available at the start of the project. The DR3 distances were checked for all sources and have differences of at most a few au for IM Lup, GM Aur, and MWC 480, which does not alter our results.

<sup>b</sup> Stellar luminosities and accretion rates extracted prior to Gaia have been updated with the new distances following Andrews et al. (2018) for IM Lup, AS 209, and HD 162396 and Macías et al. (2018) for GM Aur. Due to their large relative uncertainties, those for MWC 480 have not been rescaled. The accretion rate of GM Aur is variable (Ingleby et al. 2015), so we adopted an average value, following Macías et al. (2018).

<sup>c</sup> The stellar ages are uncertain by at least a factor of 2 and should be considered provisional.

<sup>d</sup> All stellar masses have been dynamically determined as described in Teague et al. (2021).

**References.** (1) Gaia Collaboration et al. (2018), (2) Huang et al. (2018b), (3) Alcalá et al. (2017), (4) Pinte et al. (2018a), (5) Mawet et al. (2012), (6) Huang et al. (2020), (7) Macías et al. (2018), (8) Espaillat et al. (2010), (9) Kraus & Hillenbrand (2009), (10) Beck & Bary (2019), (11) Ingleby et al. (2015), (12) Andrews et al. (2018), (13) Salyk et al. (2013), (14) Huang et al. (2017), (15) Fairlamb et al. (2015), (16) Teague et al. (2019a), (17) Liu et al. (2019), (18) Montesinos et al. (2009), (19) Simon et al. (2019), (20) Piétu et al. (2007), (21) Mendigutía et al. (2013).

velocities based on millimeter spectral lines. We note that the ages of young stars are notoriously difficult to constrain and often vary by a factor of 2 or more between different studies. The values noted in Table 1 constitute recent estimates for the MAPS sources but may be further revised by future studies. Mass accretion rates also vary substantially between different literature sources, which is due at least in part to accretion variability on short timescales (Mendigutía et al. 2013; Ellerbroek et al. 2014; Ingleby et al. 2015). This uncertainty in average accretion rates makes it difficult to use literature accretion rate values to explain disk chemical properties, since bursts in accretion may have a substantial impact on the chemistry (Rab et al. 2017). Pertinent information about individual sources is described below.

*IM Lup.* Located in the Lupus star-forming region, IM Lup likely hosts the youngest (~1 Myr) disk in the sample (Mawet et al. 2012), though a range of age estimates exist in the literature. It is approximately solar-mass and can be viewed as a young analog to the Sun. Its disk was observed by van Kempen et al. (2008) and characterized by Pinte et al. (2008) and Panić et al. (2009). Despite its youth, the IM Lup disk shows clear evidence for grain growth (Lommen et al. 2007). It stands out among other Lupus sources due to its disk mass, estimated to be 0.1–0.2  $M_{\odot}$  based on continuum (spectral energy distribution (SED), scattered-light images, and resolved millimeter images) and CO multi-isotopologue, multiline data (Pinte et al. 2008; Cleeves et al. 2016b). Such a high disk mass would typically be associated with a high accretion rate (D’Alessio et al. 1999), and while early studies failed to find signs of accretion (Padgett et al. 2006; Günther et al. 2007), more recent studies have shown that IM Lup is a rather typical T Tauri accretor (Alcalá et al. 2017).

The IM Lup disk is not only massive but also spatially very extended in both dust and gas. The pebble disk has a radius of ~264 au, which was the largest one observed within the DSHARP project (Huang et al. 2018b). It also stands out for its size in other surveys where it was included and when compared to derived disk size scaling laws (Andrews et al. 2018; Hendl et al. 2020). The CO disk extends far beyond the dust pebble disk (Panić et al. 2009), out to ~900 au, though the outer CO disk regions appear fluffy or envelope-like (Panić et al. 2009;

Cleeves et al. 2016b). IM Lup has also been observed in scattered light (Pinte et al. 2008), revealing a beautifully flared, multiringed disk in small dust grains (Avenhaus et al. 2018). The disk spiral in millimeter emission is noteworthy, since in the DSHARP sample, spirals around single stars are otherwise rare (Huang et al. 2018c).

The molecular inventory of IM Lup beyond CO was first cataloged by Öberg et al. (2011b) using the SMA as a part of the Disk Imaging Survey of Chemistry with SMA (DISCS). With ALMA, IM Lup has been observed in CO isotopologues ( $J=2-1$  and  $3-2$ ; Cleeves et al. 2016b; Pinte et al. 2018a),  $\text{H}^{13}\text{CO}^+$  and  $\text{DCO}^+ 3-2$  (Öberg et al. 2015a; Cleeves et al. 2016b), DCN and HCN  $3-2$  (Huang et al. 2017),  $\text{H}_2\text{CO } 4_{04}-3_{03}$  (Pegues et al. 2020),  $\text{C}_2\text{H } 3-2$  (Bergner et al. 2019), and  $\text{N}_2\text{H}^+ 3-2$  (Seifert et al. 2021). Notably, IM Lup shows a stunning double-ring structure in  $\text{DCO}^+ 3-2$ , which has been attributed to a change in the gas-phase C and O abundances at the pebble disk edge (Öberg et al. 2015a). It is undetected in complex nitriles (Bergner et al. 2018). The IM Lup disk was modeled in detail in Cleeves et al. (2016b, 2018) and found to be underabundant in CO by about a factor of 20 compared to molecular clouds, indicative that both oxygen and carbon are missing from the gas phase. By contrast, nitrogen does not appear to be depleted, resulting in elevated gas-phase N/O.

Using Herschel, IM Lup was searched for water vapor in the far-IR (van Dishoeck et al. 2011; Du et al. 2015). While there was no detection, indicative of water and O depletion, the upper limits were less constraining compared to some other disks, and these data have not yet been used to quantify the IM Lup  $\text{H}_2\text{O}$  reservoir. IM Lup was included in Spitzer surveys of disk volatiles but initially undetected in most molecules ( $\text{H}_2\text{O}$ , OH, HCN, and  $\text{C}_2\text{H}_2$ ) except for  $\text{CO}_2$ , indicating that its inner disk atmosphere is chemically poor (Pontoppidan et al. 2010; Salyk et al. 2011). However, IM Lup was revisited by Banzatti et al. (2017), who detected weak OH and  $\text{H}_2\text{O}$  emission, but in the case of  $\text{H}_2\text{O}$ , only at longer (33  $\mu\text{m}$ ) IR wavelengths. They suggested that IM Lup was at an intermediate stage of water depletion and still retains some water vapor in its inner disk.

*GM Aur.* The  $\sim 3$ –10 Myr T Tauri star GM Aur is in the Taurus–Auriga star-forming region and has a so-called “transition” disk, i.e., a disk with a large inner gap or cavity. Strom et al. (1989) noted it for its weak near-IR excess compared to other T Tauri stars and speculated that this and similar sources were disks in transition, which led to the name “transition disks.” Its large dust cavity of  $\sim 35$  au in radius was first inferred from SED modeling (Marsh & Mahoney 1992; Calvet et al. 2005; Espaillat et al. 2010) and later directly imaged using millimeter observations (Hughes et al. 2008). More recently, Macías et al. (2018) and Huang et al. (2020) used high-resolution ALMA observations to reveal that the outer disk consists of nested rings. Huang et al. (2020) also identified a small disk inside the gap and observed that the outer rings are surrounded by low-intensity continuum emission extending to 270 au. The mass of the GM Aur disk was recently constrained using Herschel observations of HD to 0.03–0.2  $M_{\odot}$  (McClure et al. 2016).

GM Aur has also been observed in multiple gas tracers at millimeter wavelengths. Both Dutrey et al. (2008) and Hughes et al. (2009) found that the CO emission was not entirely Keplerian toward the GM Aur disk and hypothesized that the disk is warped by a planet. A range of other common molecular tracers was clearly detected with the SMA (Öberg et al. 2010), revealing that GM Aur is bright in molecular lines associated with photochemistry and small organics. In contrast with all other disks in this program, GM Aur was not part of any early ALMA disk chemistry surveys, and there are therefore fewer subarcsecond-resolution molecular observations. Notable exceptions are  $\text{H}_2\text{CO}$ ,  $\text{DCO}^+$ , and  $\text{N}_2\text{H}^+$  (Qi et al. 2019; Pegues et al. 2020). The  $\text{N}_2\text{H}^+$  was further used to constrain the CO and  $\text{N}_2$  snow line locations to 48 and 78 au (Qi et al. 2019). In addition, Huang et al. (2020) observed the GM Aur disk in  $\text{HCO}^+ J=3-2$  at a higher spatial resolution,  $\sim 0''.1$ , and found that the radial emission profile has substantial substructure, most of which could be attributed to continuum absorption.

GM Aur was included in Herschel spectral line surveys and found to be somewhat depleted in oxygen ([O I]; Keane et al. 2014), not detected in water (Du et al. 2017), and not detected in [C II] (Howard et al. 2013). It was not included in the large Spitzer surveys of disk molecular lines due to its low IR flux (Pontoppidan et al. 2010), and its inner disk molecular content is therefore unknown.

*AS 209.* AS 209 is a young ( $\sim 1$ –2 Myr) T Tauri star in the Ophiuchus star-forming region. The global disk structure was modeled by Qi et al. (2019) and found to have a thin isothermal midplane layer and an inner wall. The disk is highly structured in millimeter continuum emission with at least seven nested rings (Andrews et al. 2009, 2018; Fedele et al. 2018; Guzmán et al. 2018; Huang et al. 2018a), some of which have been associated with ongoing planet formation (Guzmán et al. 2018; Favre et al. 2019). In addition, observations at millimeter and centimeter wavelengths show clear evidence for both grain growth and pebble size-dependent grain drift (Pérez et al. 2012; Tazzari et al. 2016). Observations in scattered light also indicate the presence of three rings (Avenhaus et al. 2018).

Based on CO isotopologue observations, the radial gas surface density and/or CO abundance profiles are highly structured as well. Huang et al. (2016) first showed that  $\text{C}^{18}\text{O}$  has a substantial gap and a ring close to the millimeter dust edge. This observation was confirmed by Favre et al. (2019) using higher-resolution and higher-sensitivity observations,

which enabled them to associate the  $\text{C}^{18}\text{O}$  gap with a dust gap. Observing the main CO isotopologue, Guzmán et al. (2018) found multiple depressions in the CO radial profile that could be related to either peaks or gaps in the dust emission radial profile. Furthermore, Teague et al. (2018b) found that the continuum and near-IR structures are associated with gas surface density perturbations, derived from the rotational velocity of  $^{12}\text{CO}$ .

The AS 209 disk is known to have a rich molecular line inventory at millimeter wavelengths (Öberg et al. 2011b; Huang et al. 2017; Bergner et al. 2018, 2019). Most of the millimeter molecular emission appears to be depleted toward the disk center, and whether this is an effect of dust opacity, excitation, C/N/O abundance, or gas surface density has not been resolved. This is addressed within MAPS in Bosman et al. (2021a). The inner disk chemistry of AS 209 has not been well characterized, and there are only upper limits from Herschel on the water reservoir (Du et al. 2017).

*HD 163296.* Due to its relative proximity and massive disk, HD 163296 is one of the most well-studied Herbig Ae star–disk systems at millimeter wavelengths; it is estimated to contain 0.1–0.5  $M_{\odot}$  (Isella et al. 2007; Tilling et al. 2012; Muro-Arena et al. 2018; Powell et al. 2019; Kama et al. 2020). The age of HD 163296 is somewhat unclear, but most studies suggest it is at least 6 Myr old (Fairlamb et al. 2015; Wichittanakom et al. 2020). The disk presents multiple features that suggest the presence of planets and ongoing planet formation, including dust rings, azimuthal asymmetries, deviations from Keplerian velocities due to gas pressure variations, “kinks” in the CO emission, and meridional flows (Isella et al. 2016, 2018; Pinte et al. 2018b, 2020; Teague et al. 2018a, 2019a; Rodenkirch et al. 2021). The three large circular gaps in the millimeter continuum at 45, 87, and 140 au are especially visible in Figure 2. The HD 163296 disk has been observed in scattered light at optical and infrared wavelengths, revealing substantial radial substructure also at these shorter wavelengths (Monnier et al. 2017; Muro-Arena et al. 2018; Rich et al. 2020).

As part of a number of single-dish, SMA, and ALMA projects, HD 163296 has been observed in CO and other molecular tracers at millimeter wavelengths (e.g., Thi et al. 2004; Öberg et al. 2011b; Qi et al. 2011; de Gregorio-Monsalvo et al. 2013; Klaassen et al. 2013; Mathews et al. 2013; Rosenfeld et al. 2013; Flaherty et al. 2015; Huang et al. 2017; Salinas et al. 2017; Guzmán et al. 2018; Bergner et al. 2019; Booth et al. 2019; Notsu et al. 2019; Pegues et al. 2020; Zhang et al. 2021). Its popularity in previous surveys can be explained by its bright molecular lines, not only in CO isotopologues but also in HCN,  $\text{HCO}^+$ , deuterated species, and larger organics. It was subject to a deep search for  $\text{CH}_3\text{OH}$ , which yielded an abundance upper limit well below what has been seen toward the nearby TW Hya disk, indicative of a hostile environment for some families of organic molecules (Carney et al. 2019). The CO snow line was first estimated by Qi et al. (2011) and then revised by Qi et al. (2015) to 75 au, assuming a 101 pc (Gaia) distance.

Similar to most disks around Herbig Ae stars, the HD 163296 disk is relatively line-poor at IR wavelengths (Pontoppidan et al. 2010; Salyk et al. 2011), which may simply be a result of high continuum flux levels (Antonellini et al. 2016). However,  $\text{H}_2\text{O}$  and OH have been detected in the HD 163296 disk at both mid-IR (33  $\mu\text{m}$ ) and far-IR wavelengths (Fedele et al. 2012; Banzatti et al. 2017), revealing

a disk atmosphere that is not completely dry. HD 162396 has also been observed, though not detected, in high-J CO lines with Herschel (Du et al. 2017), which, together with continuum data and [O I] and low-J CO line detections, have provided constraints on the disk temperature structure and atmospheric gas-to-dust ratio (Tilling et al. 2012). The inner disk also appears asymmetric, potentially hosting a large-scale vortex, which may impact its chemistry (Varga et al. 2021).

*MWC 480.* The  $\sim 7$  Myr old Herbig Ae star MWC 480 is in the Taurus–Auriga star-forming region (Montesinos et al. 2009). Its disk has been characterized through millimeter continuum observations (Piétu et al. 2006), and recent  $0''.1$  observations with ALMA show that the disk has an outer dust gap and ring, as well as low-level millimeter emission extending out to  $\sim 200$  au (Long et al. 2018; Liu et al. 2019). Scattered-light images of the disk reveal that the smaller grains are similarly extended but do not present any substructure (Kusakabe et al. 2012).

The gas structure of the MWC 480 disk has been probed using CO observations, and the outer disk exhibits a vertical temperature gradient (Piétu et al. 2007). Hughes et al. (2008) showed that the CO gas is much more extended than the millimeter pebbles.

MWC 480 was included in both the Chemistry in Disks (CID) and DISCS programs and has therefore had its disk chemistry extensively explored at medium spatial resolution at both 1 and 3 mm (Dutrey et al. 2007, 2011; Henning et al. 2010; Öberg et al. 2010). These early observations showed that while the disk is very bright in some lines, e.g.,  $\text{HCO}^+$  and HCN, it is weak in others, including  $\text{N}_2\text{H}^+$  and  $\text{H}_2\text{CO}$  (Dutrey et al. 2007; Pegues et al. 2020). MWC 480 was the first disk where  $\text{CH}_3\text{CN}$  was detected (Öberg et al. 2015b), the most complex molecule seen in disks so far, and it has since been probed at  $\sim 0''.5$  resolution in simple and complex nitriles, deuterated molecules,  $\text{H}_2\text{CO}$ , and sulfur-bearing species (Guzmán et al. 2015; Huang et al. 2017; Bergner et al. 2018; Le Gal et al. 2019a; Pegues et al. 2020). Most recently, MWC 480 has been the target of an unbiased spectral line survey (Loomis et al. 2020), which resulted in detections of several new disk molecules, including  $\text{C}_2\text{D}$  and  $\text{H}_2\text{CS}$ .

The MWC 480 water content was probed in depth by Herschel as a part of the Water In Star-forming regions with Herschel key program (van Dishoeck et al. 2011) but was not detected (Du et al. 2017). A stacked detection was obtained when combining the MWC 480 data with three other disks, but its implications for the MWC 480 water budget are difficult to ascertain (Du et al. 2017). The inner disk chemistry of MWC 480 is unknown.

## 2.2. Line Targets

Within MAPS, we observed the five disks in four spectral setups (Tables 2 and 3). These were selected to address the largest number of science goals in the smallest number of spectral settings. We mainly focused on molecules that had been previously detected in disks, and all lines targeted in ALMA Band 6 had been detected in at least some of the disks in the sample. By contrast, the majority of lines targeted in ALMA Band 3 had not been observed in any disks prior to MAPS.

The full set of molecules includes tracers of gas structure, mass, and kinematics (CO isotopologues); C/N/O/S ratios

( $\text{C}_2\text{H}$ , HCN, CO isotopologues, and CS); disk organic inventories and chemistry ( $\text{C}_2\text{H}$ , HCN,  $\text{H}_2\text{CO}$ ,  $c\text{-C}_3\text{H}_2$ ,  $\text{HC}_3\text{N}$ , and  $\text{CH}_3\text{CN}$ ); deuterium fractionation (DCN and  $\text{N}_2\text{D}^+$ ); disk ionization ( $\text{HCO}^+$ ,  $\text{H}^{13}\text{CO}^+$ , and  $\text{N}_2\text{D}^+$ ); and photochemistry (CN and  $\text{C}_2\text{H}$ ). A substantial subset of species is covered in at least two transitions with different upper energy levels— $^{13}\text{CO}$ ,  $\text{C}^{18}\text{O}$ , HCN,  $\text{C}_2\text{H}$ ,  $\text{HC}_3\text{N}$ , and  $\text{CH}_3\text{CN}$ —which enables excitation analysis using, e.g., rotational diagrams. In addition, HCN, CN,  $\text{C}^{17}\text{O}$ , and  $\text{C}_2\text{H}$  lines present resolvable fine or hyperfine structure, which are used to empirically determine line excitation conditions such as density, temperature, and line optical depth, and from there column densities. The  $c\text{-C}_3\text{H}_2$  was also detected in two lines with similar excitation temperatures. The main molecular targets of MAPS— $^{13}\text{CO}$ ,  $\text{C}^{18}\text{O}$ , HCN,  $\text{C}_2\text{H}$ ,  $\text{HC}_3\text{N}$ , and  $\text{CH}_3\text{CN}$ —were observed at both 1 mm (ALMA Band 6) and 3 mm (ALMA Band 3).

Tables 2 and 3 list the molecular properties used within the MAPS program.

## 3. Observational Details, Calibration, and Imaging

### 3.1. Observations

MAPS (2018.1.01055.L) was executed between 2018 October and 2019 September (with some remaining executions scheduled for 2021). The short-baseline executions were observed between 2018 October and 2019 April, while all long-baseline executions were taken in 2019 August and September. In total, 80 executions have been carried out, most of which consisted of  $\sim 45$  minutes on target and 20–45 minutes of calibration, with longer calibration times required for the longer-baseline observations. Tables 9 and 10 in Appendix A list the observational details, including observing dates, number of antennas, integration times, baselines, approximate angular resolution, maximum recoverable scale, and phase and flux calibrators for each execution. Note that GM Aur and MWC 480 always shared tracks, and their listed integration times were exactly split between the two sources in each execution.

A key aspect of the MAPS project is the correlator setup, which is outlined in Table 4 for the two ALMA Band 3 (B3-1 and B3-2) and Band 6 (B6-1 and B6-2) observing modes. Each correlator setup consist of six to nine spectral windows (SPWs), one of which is a continuum band with a coarse ( $1.4\text{--}3.4\text{ km s}^{-1}$ ) velocity resolution. The latter is needed to self-calibrate (see next section). The remaining SPWs are designed to have a velocity resolution of  $0.19\text{--}0.49\text{ km s}^{-1}$  in B3-1 and B3-2 and  $0.09\text{--}0.20\text{ km s}^{-1}$  in B6-1 and B6-2, and no online spectral binning was applied. These velocity resolutions are well below the typical disk-averaged line widths of a few kilometers per second but comparable to the intrinsic line widths of  $<0.5\text{ km s}^{-1}$ . The highest resolution of  $0.09\text{ km s}^{-1}$  is used for the CO 2–1 line, to enable kinematic studies. Other expected strong lines were observed at  $<0.2\text{ km s}^{-1}$  and weaker lines at coarser resolution unless paired with a strong line. In each case, we used the maximum resolution possible for the chosen bandwidth. For the delivered data products, the velocity resolutions have been coarsened to achieve more uniformity between spectral line cubes, as described in Czekala et al. (2021).

**Table 2**  
Lines Targeted at 3 mm (ALMA Band 3)

Molecule	QN	Rest Freq. (GHz)	$\log_{10}(A_{ij}/s^{-1})$	$g_u$	$E_u$ (K)	Cat. <sup>a</sup>	Detected				
							IM Lup	GM Aur	AS 209	HD 163296	MWC 480
<b>B3-1</b>											
HC <sup>15</sup> N	$J = 1-0$	86.054966	-4.6569	3	4.1	CDMS	N	N	N	N	N
H <sup>13</sup> CN <sup>b</sup>	$J = 1-0$	86.339921	-4.6526	9	4.1	CDMS	N	(Y) <sup>c</sup>	N	N	N
H <sup>13</sup> CO <sup>+</sup>	$J = 1-0$	86.754288	-4.4142	3	4.2	LAMDA	(Y) <sup>c</sup>	Y	(Y) <sup>c</sup>	Y	(Y) <sup>c</sup>
C <sub>2</sub> H	$N = 1-0,$ $J = \frac{3}{2}-\frac{1}{2}, F = 2-1$	87.316898	-5.6560	5	4.2	CDMS	Y	Y	Y	Y	Y
	$N = 1-0,$ $J = \frac{3}{2}-\frac{1}{2}, F = 1-0$	87.328585	-5.7367	3	4.2	CDMS	Y	Y	Y	Y	Y
HCN <sup>b</sup>	$J = 1-0, F = 1-1$	88.630416	-4.6184	3	4.3	CDMS	Y	Y	Y	Y	Y
	$J = 1-0, F = 2-1$	88.631848	-4.6185	5	4.3	CDMS	Y	Y	Y	Y	Y
	$J = 1-0, F = 0-1$	88.633936	-4.6184	1	4.3	CDMS	Y	Y	Y	Y	Y
HCO <sup>+</sup>	$J = 1-0$	89.188525	-4.3715	3	4.3	CDMS	Y	Y	Y	Y	Y
HC <sub>3</sub> N	$J = 11-10$	100.076392	-4.1096	23	28.8	CDMS	N	Y	Y	Y	Y
H <sub>2</sub> CO	$(J_{K_a, K_c}) = 6_{15}-6_{16}$	101.332991	-5.8037	39	87.6	CDMS	N	N	N	N	N
<b>B3-2</b>											
CS	$J = 2-1$	97.980953	-4.7763	5	7.1	CDMS	Y	Y	Y	Y	Y
C <sup>18</sup> O	$J = 1-0$	109.782173	-7.2030	3	5.3	LAMDA	Y	Y	Y	Y	Y
<sup>13</sup> CO	$J = 1-0$	110.201354	-7.2011	3	5.3	LAMDA	Y	Y	Y	Y	Y
CH <sub>3</sub> CN	$J = 6-5, K = 5$	110.330345	-4.4697	26	197.1	CDMS	N	N	N	N	N
	$J = 6-5, K = 4$	110.349471	-4.2098	26	132.8	CDMS	N	N	N	N	N
	$J = 6-5, K = 3$	110.364354	-4.0792	52	82.8	CDMS	N	N	N	N	N
	$J = 6-5, K = 2$	110.374989	-4.0054	26	47.1	CDMS	N	(Y) <sup>c</sup>	Y	N	N
	$J = 6-5, K = 1$	110.381372	-3.9664	26	25.7	CDMS	N	(Y) <sup>c</sup>	Y	(Y) <sup>c</sup>	Y
C <sup>17</sup> O	$J = 1-0, F = \frac{3}{2}-\frac{5}{2}$	112.358777	-7.1739	4	5.4	CDMS	(Y) <sup>c</sup>	Y	(Y) <sup>c</sup>	Y	Y
	$J = 1-0, F = \frac{7}{2}-\frac{5}{2}$	112.358982	-7.1739	8	5.4	CDMS	(Y) <sup>c</sup>	Y	(Y) <sup>c</sup>	Y	Y
	$J = 1-0, F = \frac{5}{2}-\frac{5}{2}$	112.360007	-7.1739	6	5.4	CDMS	(Y) <sup>c</sup>	Y	(Y) <sup>c</sup>	Y	Y
CN	$N = 1-0,$ $J = \frac{3}{2}-\frac{1}{2}, F = \frac{3}{2}-\frac{1}{2}$	113.488120	-5.1716	4	5.4	CDMS	Y	Y	Y	Y	Y
	$N = 1-0,$ $J = \frac{3}{2}-\frac{1}{2}, F = \frac{5}{2}-\frac{3}{2}$	113.490970	-4.9236	6	5.4	CDMS	Y	Y	Y	Y	Y
	$N = 1-0,$ $J = \frac{3}{2}-\frac{1}{2}, F = \frac{1}{2}-\frac{1}{2}$	113.499644	-4.9735	2	5.4	CDMS	Y	Y	Y	Y	Y
	$N = 1-0,$ $J = \frac{3}{2}-\frac{1}{2}, F = \frac{1}{2}-\frac{1}{2}$	113.508907	-5.2848	4	5.4	CDMS	Y	Y	Y	Y	Y
	$N = 1-0,$ $J = \frac{3}{2}-\frac{1}{2}, F = \frac{3}{2}-\frac{3}{2}$	113.508907	-5.2848	4	5.4	CDMS	Y	Y	Y	Y	Y

**Notes.**

<sup>a</sup> Spectroscopic data are compiled from the CDMS (Müller et al. 2001, 2005; Endres et al. 2016), JPL (Pickett et al. 1998), and LAMBDA (Schöier et al. 2005) catalogs. See individual MAPS papers for complete spectroscopic references for each line.

<sup>b</sup> See Cataldi et al. (2021) for the full list of hyperfine components.

<sup>c</sup> Tentatively detected with a  $3\sigma$ – $5\sigma$  significance (Aikawa et al. 2021; Cataldi et al. 2021; Ilee et al. 2021; Zhang et al. 2021).

### 3.2. Calibration Strategy

Our calibration strategy closely follows the one developed for the DSHARP ALMA Large Program, which is described in detail by Andrews et al. (2018). We summarize the strategy here and provide more extensive descriptions of any procedures that deviated from the DSHARP script.

All data were initially calibrated by ALMA staff using the ALMA calibration pipeline. The short- and long-baseline data were calibrated separately, and because some of the short-baseline data were observed a year before the last long-baseline observations were completed, not all data were calibrated with the same pipeline version. CASA 5.4 was used for the observations carried out in 2018, and CASA 5.6 was used for

the observations carried out in 2019. The observations typically have  $T_{\text{sys}} \sim 50$ – $80$  K, and the rms phase variations after water vapor radiometer corrections were generally within a range of  $\sim 15^\circ$ – $50^\circ$ .

All data were self-calibrated. Prior to self-calibration, we carried out a number of data processing steps. Unless otherwise noted, we used CASA 5.6 for these steps, as well as for self-calibration. We used CASA in parallel mode for all tasks where it is supported, but due to a bug in CASA 5.6, we had to switch to CASA 5.4 when running the `gaincal` and `virtualconcat` tasks.

As a first step toward self-calibration, we created pseudo-continuum visibilities by flagging the line emission in each SPW. Except for the case of CO 2–1 toward HD 163296, we



**Table 3**  
Lines Targeted at 1 mm (ALMA Band 6)

Molecule	QN	Rest Freq. (GHz)	$\log_{10}(A_{ij}/s^{-1})$	$g_u$	$E_u$ (K)	Cat. <sup>a</sup>	Detected				
							IM Lup	GM Aur	AS 209	HD 163296	MWC 480
B6-1											
DCN <sup>b</sup>	$J = 3-2$	217.238538	-3.3396	21	20.9	CDMS	Y	Y	Y	Y	Y
<sup>13</sup> CN	$N = 2-1, J = \frac{3}{2}-\frac{1}{2}$	217.264639	-3.9547	1	15.7	CDMS	N	N	N	N	N
	$F1 = 1-0, F = 0-1$										
	$N = 2-1, J = \frac{3}{2}-\frac{1}{2}$	217.277680	-3.4953	3	15.7	CDMS	N	N	N	N	N
	$F1 = 1-0, F = 1-1$										
	$N = 2-1, J = \frac{3}{2}-\frac{1}{2}$	217.286804	-3.6541	5	15.6	CDMS	N	N	N	N	N
	$F1 = 2-1, F = 2-2$										
	$N = 2-1, J = \frac{3}{2}-\frac{1}{2}$	217.290823	-3.6567	3	15.6	CDMS	N	N	N	N	N
	$F1 = 2-1, F = 1-1$										
H <sub>2</sub> CO	$(J_{K_a, K_c}) = 3_{03}-2_{02}$	218.222192	-3.5504	7	21.0	JPL	Y	Y	Y	Y	Y
C <sup>18</sup> O	$J = 2-1$	219.560354	-6.2211	5	15.8	LAMDA	Y	Y	Y	Y	Y
<sup>13</sup> CO	$J = 2-1$	220.398684	-6.2191	5	15.9	LAMDA	Y	Y	Y	Y	Y
CH <sub>3</sub> CN	$J = 12-11, K = 3$	220.709017	-3.0624	100	133.2	CDMS	N	(Y) <sup>c</sup>	N	(Y) <sup>c</sup>	Y
	$J = 12-11, K = 2$	220.730261	-3.0465	50	97.4	CDMS	N	Y	N	Y	Y
	$J = 12-11, K = 1$	220.743011	-3.0372	50	76.0	CDMS	(Y) <sup>c</sup>	Y	Y	Y	Y
	$J = 12-11, K = 0$	220.747262	-3.0342	50	68.9	CDMS	N	Y	Y	Y	Y
CO	$J = 2-1$	230.538000	-6.1605	5	16.6	LAMDA	Y	Y	Y	Y	Y
N <sub>2</sub> D <sup>+</sup> <sup>b</sup>	$J = 3-2$	231.321828	-3.3586	63	22.2	CDMS	Y	(Y) <sup>c</sup>	Y	Y	Y
B6-2											
<i>c</i> -C <sub>3</sub> H <sub>2</sub>	$(J_{K_a, K_c}) = 7_{07}-6_{16}$ <sup>d</sup>	251.314367	-3.0704	45	50.7	CDMS	(Y) <sup>c</sup>	Y	Y	Y	Y
	$(J_{K_a, K_c}) = 6_{15}-5_{24}$	251.508708	-3.1708	13	47.5	CDMS	N	Y	Y	Y	Y
	$(J_{K_a, K_c}) = 6_{25}-5_{14}$	251.527311	-3.1706	39	47.5	CDMS	N	Y	N	Y	Y
C <sub>2</sub> H	$N = 3-2,$ $J = \frac{7}{2}-\frac{5}{2}, F = 4-3$	262.004260	-4.1152	9	25.2	CDMS	Y	Y	Y	Y	Y
	$N = 3-2,$ $J = \frac{7}{2}-\frac{5}{2}, F = 3-2$	262.006482	-4.1321	7	25.2	CDMS	Y	Y	Y	Y	Y
	$N = 3-2,$ $J = \frac{5}{2}-\frac{3}{2}, F = 3-2$	262.064986	-4.1521	7	25.2	CDMS	Y	Y	Y	Y	Y
	$N = 3-2,$ $J = \frac{5}{2}-\frac{3}{2}, F = 2-1$	262.067469	-4.1906	5	25.2	CDMS	Y	Y	Y	Y	Y
	$N = 3-2,$ $J = \frac{5}{2}-\frac{3}{2}, F = 2-2$	262.078935	-5.0619	5	25.2	CDMS	Y	Y	Y	Y	Y
HC <sub>3</sub> N	$J = 29-28$	263.792308	-2.8349	59	189.9	CDMS	N	Y	Y	Y	Y
HCN <sup>b</sup>	$J = 3-2, F = 3-2$	265.886434	-3.1292	7.0	25.5	CDMS	Y	Y	Y	Y	Y
	$J = 3-2, F = 3-3$	265.884891	-4.0322	7.0	25.5	CDMS	Y	Y	Y	Y	Y
	$J = 3-2, F = 2-2$	265.888522	-3.8861	5.0	25.5	CDMS	Y	Y	Y	Y	Y

**Notes.**

<sup>a</sup> Spectroscopic data are compiled from the CDMS (Müller et al. 2001, 2005; Endres et al. 2016), JPL (Pickett et al. 1998), and LAMBDA (Schöier et al. 2005) catalogs.

<sup>b</sup> See Cataldi et al. (2021) for the full list of hyperfine components.

<sup>c</sup> Tentatively detected with a  $3\sigma$ - $5\sigma$  significance (Cataldi et al. 2021; Ilee et al. 2021).

<sup>d</sup> Ortho/para blend; see Ilee et al. (2021) for the full line list.

flagged channels with velocities between  $-10$  and  $20$  km s<sup>-1</sup> (all sources have systemic velocities between  $4.5$  and  $5.8$  km s<sup>-1</sup>). In the SPW containing CO 2-1 toward HD 163296, we extended the flagged region to include its disk wind (Klaassen et al. 2013). Second, we averaged down the pseudocontinuum data into 125 MHz channels and imaged each execution block. We identified the continuum peak emission and used it to align the different executions to a common phase center.

We self-calibrated the aligned data, starting with short spacings (short-baseline data). The self-calibrated short-spacing data were then concatenated with the long-baseline data, and

the combined visibilities were self-calibrated together. In the self-calibration of the Band 3 short-spacing data and the combined data of both settings, we combined SPWs and scans to improve the signal-to-noise ratio (S/N). That was not necessary for the Band 6 short-spacing data due to their higher continuum brightness. We performed between one and six iterations of phase-only self-calibrations and then tried one amplitude self-calibration. We typically started with a solution interval of 900 s and then stepped down to 360, 180, 60, 30, and 18 s in each iteration. The reference antenna was chosen from the log based on its data quality and position in the array.

**Table 4**  
Correlator Setups in ALMA Bands 3 and 6

Setup	Center Freq. (GHz)	Line Targets <sup>a</sup>	Resolution (km s <sup>-1</sup> )	Bandwidth (MHz)
B3-1	86.054966	HC <sup>15</sup> N $J = 1-0$	0.492	58.59
	86.339918	H <sup>13</sup> CN $J = 1-0$	0.490	58.59
	86.754288	H <sup>13</sup> CO <sup>+</sup> $J = 1-0$	0.488	58.59
	87.310000	C <sub>2</sub> H $N = 1-0$	0.485	58.59
	88.631601	HCN $J = 1-0$	0.239	58.59
	89.188526	HCO <sup>+</sup> $J = 1-0$	0.237	58.59
	99.000000	Continuum band	3.419	1875
	100.076392	HC <sub>3</sub> N $J = 11-10$	0.211	58.59
	101.332991	H <sub>2</sub> CO ( $J_{K_a, K_c}$ ) = 6 <sub>15</sub> -6 <sub>16</sub>	0.209	58.59
	B3-2	97.980953	CS $J = 2-1$	0.216
100.000000		Continuum band	3.385	1875
109.782176		C <sup>18</sup> O $J = 1-0$	0.385	58.59
110.201354		<sup>13</sup> CO $J = 1-0$	0.384	58.59
110.381346		CH <sub>3</sub> CN $J = 6-5, K = 0-5$	0.383	117.19
112.359278		C <sup>17</sup> O $J = 1-0$	0.188	58.59
113.499644		CN $N = 1-0$	0.186	58.59
B6-1	217.238530	DCN $J = 3-2, ^{13}\text{CN } N = 2-1$	0.195	117.19
	218.222192	H <sub>2</sub> CO ( $J_{K_a, K_c}$ ) = 3 <sub>03</sub> -2 <sub>02</sub>	0.194	117.19
	219.560358	C <sup>18</sup> O 2-1	0.193	58.59
	220.398684	<sup>13</sup> CO 2-1	0.192	58.59
	220.709099	CH <sub>3</sub> CN $J = 12-11, K = 2-4$	0.192	58.59
	220.743097	CH <sub>3</sub> CN $J = 12-11, K = 0-2$	0.192	58.59
	230.538000	CO $J = 2-1$	0.092	58.59
	231.321828	N <sub>2</sub> D <sup>+</sup> $J = 3-2$	0.091	58.59
	234.000000	Continuum band	1.446	1875
B6-2	249.000000	Continuum band	1.359	1875
	251.314337	<i>c</i> -C <sub>3</sub> H <sub>2</sub> ( $J_{K_a, K_c}$ ) = 7 <sub>07</sub> -6 <sub>16</sub>	0.168	117.19
	251.527302	<i>c</i> -C <sub>3</sub> H <sub>2</sub> ( $J_{K_a, K_c}$ ) = 6 <sub>25</sub> -5 <sub>14</sub>	0.168	117.19
	262.040000	C <sub>2</sub> H $N = 3-2$	0.161	117.19
	263.792308	HC <sub>3</sub> N $J = 29-28$	0.160	117.19
	265.886431	HCN $J = 3-2$	0.159	234.38

**Note.**

<sup>a</sup> A full listing of line properties is found in Tables 2 and 3.

We applied the calibration table to spectrally averaged visibilities in each iteration and imaged the data with the `tclean` task using a Briggs robust parameter of 0.5 and an elliptical mask. The mask dimensions and position angle were selected based on the inclination and position angle of each disk. The resulting peak intensity and image S/N were used to determine whether to proceed with the next iteration or not; if the peak intensity increased and the S/N improved by a factor larger than 5%, we proceeded with the next iteration, choosing a shorter solution interval. After reaching the stopping criteria for phase self-calibration, we attempted one round of amplitude self-calibration and used the results if the peak S/N increased and the image quality visually improved. Finally, the resulting calibration tables were applied to the aligned but unflagged and spectrally nonaveraged visibilities. We used the task `uvcontsub` to subtract the continuum, providing a `.contsub` measurement set for each disk/setting. These data products, as well as the continuum+line measurement sets, are available for download from the ALMA Archive.<sup>29</sup>

The improvements in the continuum images following self-calibration were substantial for the Band 6 settings and smaller for the Band 3 settings. The CLEAN beam was typically

around 0''1 in Band 6 and 0''3 in Band 3, with an rms of 10–20 μJy beam<sup>-1</sup>. The continuum image properties are discussed in Sierra et al. (2021), and we refer the reader to that paper for more details on the MAPS continuum data.

### 3.3. Summary of Imaging Strategy and Products

The scope of MAPS and its range of line targets observed at high resolution required substantial development work to produce accurate and aesthetically pleasing imaging products. The MAPS imaging strategy and its motivations and verification are described in detail in Czekala et al. (2021). Here we summarize key aspects of the process. Prior to imaging, the data were split into individual measurement sets for each targeted line and regridded onto a common velocity grid using the task `cvel2` in CASA. A velocity spacing of 0.2 km s<sup>-1</sup> was used for the Band 6 data and 0.5 km s<sup>-1</sup> for the Band 3 data. Channels were centered on the systemic velocity of each disk (see Table 1) and extended out to 1.2× the empirically determined extent of the <sup>12</sup>CO 2–1 emission for each disk. This procedure was repeated for both the continuum-subtracted data and the data still containing continuum emission. The MAPS images were produced using the task `tclean` in CASA. Unless stated otherwise, we built CLEAN masks assuming

<sup>29</sup> <https://almascience.org/alma-data/lp/maps>

**Table 5**  
Overview of Spectral Image Cube Spatial Resolutions

B3-1	B3-2	B6-1	B6-2
0''22–0''32 <sup>a</sup>	0''21–0''28 <sup>a</sup>	0''10–0''13 <sup>a</sup>	0''09–0''11 <sup>a</sup>
		0''15 <sup>b</sup>	0''15 <sup>b</sup>
		0''2	0''2
0''3 <sup>b</sup>	0''3 <sup>b</sup>	0''3	0''3
0''5	0''5		

**Notes.**

<sup>a</sup> Resolution range refers to the minor beam axis when using `robust = 0.5`.

<sup>b</sup> These are the fiducial MAPS imaging products.

Keplerian rotation and the stellar masses, disk inclinations, and position angles listed in Table 1. The outer radii of these masks were set to generously incorporate all emission from <sup>13</sup>CO 2–1, which had the most extended emission structure except <sup>12</sup>CO 2–1, toward each disk. Because <sup>12</sup>CO 2–1 displays non-Keplerian structure in some of the disks, we used manual, hand-drawn masks for this line. Emission was cleaned down to  $4\times$  rms, estimated in a line-free region. See Section 5 of Czekala et al. (2021) for more details on this decision.

The Band 6 and Band 3 spectral line cubes were initially cleaned to achieve high spatial resolution while simultaneously achieving good image fidelity. Using a robust parameter of 0.5, we achieved beam minor and major axis FWHMs of 0''09–0''13 and 0''11–0''17, respectively, in Band 6 and 0''21–0''32 and 0''26–0''47, respectively, in Band 3. This corresponds to spatial resolutions of 10–20 au in Band 6 and 20–50 au in Band 3. We found that applying a small taper to the Band 6 images substantially improved the sensitivity to low surface brightness features and resulted in smoother images while minimally decreasing the resolution. For our fiducial images, we applied tapers that resulted in a circularized 0''15 beam for the Band 6 data. We also reimaged the Band 3 data with a circularized 0''3 beam, and these are the fiducial Band 3 images. Unless stated otherwise, these fiducial image cubes form the basis of the analysis within the MAPS collaboration. In addition, the Band 6 line image cubes were also tapered to achieve beams of 0''2 and 0''3, respectively. The latter facilitated imaging of the weakest lines, as well as comparisons between the Band 3 and Band 6 lines. To increase the S/N for the weakest Band 3 lines, we also tapered the Band 3 images to a resolution of 0''5. Table 5 summarizes the available image cube resolutions.

After generating the image cubes, image residuals were scaled by a factor  $\epsilon$ , equal to the ratio of the CLEAN beam and dirty beam effective areas, to account for the effects of non-Gaussian beams (resulting from joint configuration imaging) on the image quality and to provide a realistic image S/N (Jorsater & van Moorsel 1995). Throughout MAPS, we refer to this as the  $J\nu M$  correction, and it is needed because the dirty beam was highly non-Gaussian when combining the short- and long-baseline configurations (see Czekala et al. 2021, for further details). The applied  $J\nu M$  corrections to the image residuals are listed in Table 11 in Appendix B for our fiducial image line cubes, together with the measured rms (after application of the  $J\nu M$  correction). Figure 3(a) visualizes 40 of the channels belonging to the HD 163296 fiducial HCN 3–2 spectral image cube, i.e., a channel map. The Keplerian rotation of the disk is visible, as is some radial substructure.

### 3.4. Value-added Data Products

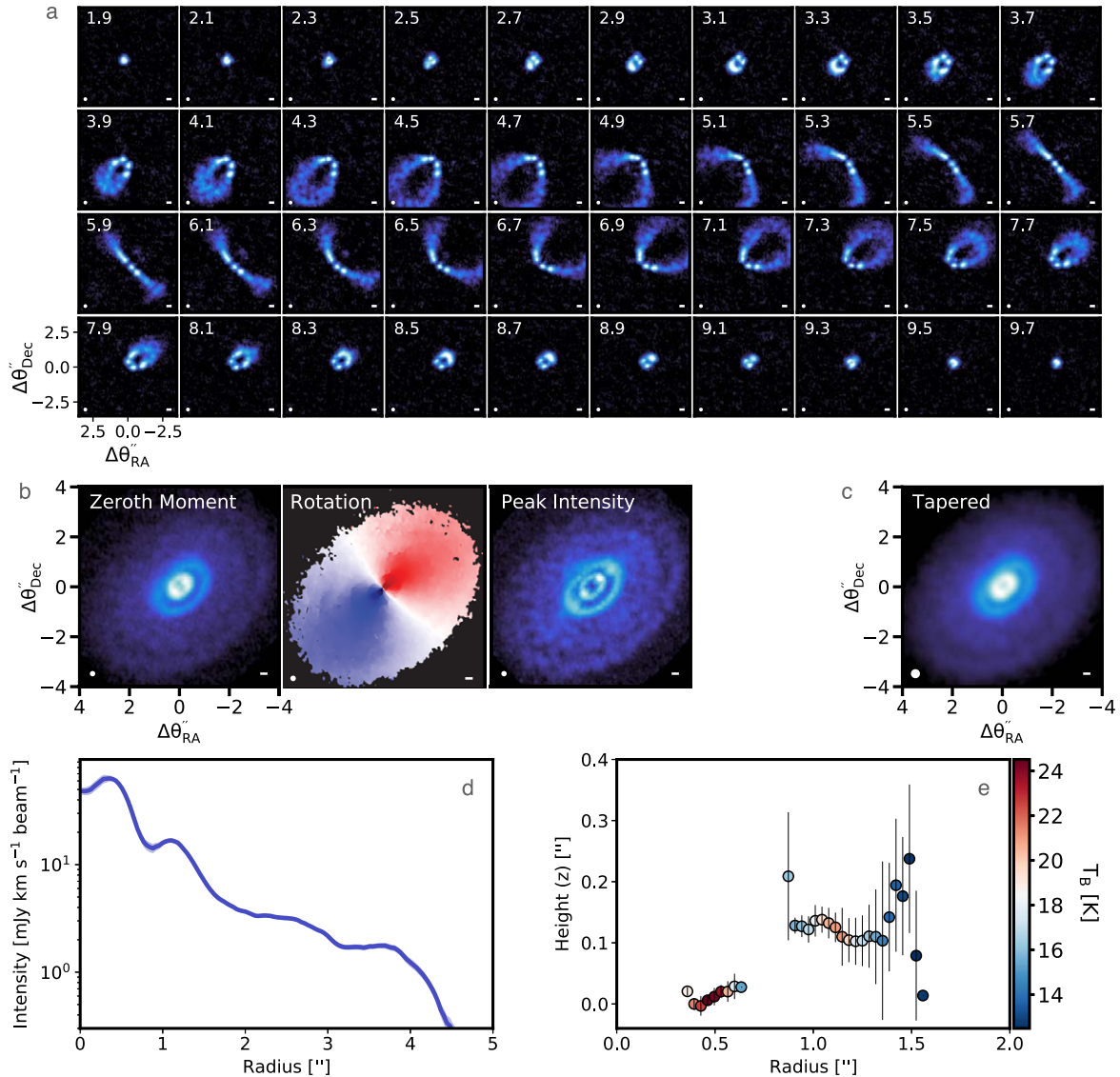
In addition to spectral image cubes, we have generated a range of higher-level image products and radial profiles, referred to collectively as value-added data products (VADPs). The process through which these were generated and their detailed descriptions can be found in Law et al. (2021a). Figure 3 shows some examples of these image products. In particular, Figure 3(b) shows the fiducial (0''15) zeroth-moment (integrated flux), rotation (velocity field), and peak intensity (spectral line maximum intensity) maps of the HD 163296 HCN 3–2 line. The zeroth-moment map clearly shows two small-scale rings, as well as one or two diffuse rings in the outer disk. The rotation map shows a characteristic Keplerian velocity field. Figure 3(c) shows the zeroth-moment map generated from the low-resolution 0''3 spectral image cube. Compared to the fiducial zeroth-moment map, the inner rings are less sharp, while the outer disk structure is more clearly visible, demonstrating the utility of imaging the same line and disk with different tapers. Note that most moment maps shown in MAPS papers have been optimized to visualize substructure and best show the quality of the data using “hybrid” masks, as described in Law et al. (2021a). For any quantitative science, we strongly recommend using either zeroth-moment maps generated without the hybrid masks or line image cubes or radial profiles.

The top-level image-derived products are radial profiles and emission surfaces. The radial profiles are generated from zeroth-moment maps constructed using only Keplerian masks (i.e., not from the “hybrid” zeroth-moment maps described above) and take into account the derived molecular emission heights when available (Law et al. 2021b). For lines with no empirical constraints on their emission surfaces, we assume that the emission originates from  $z/r=0$ , i.e., the midplane (Law et al. 2021a). In each case, the emission is deprojected using the disk inclinations and position angles listed in Table 1 and the python package `GoFish` (Teague 2019). The emission is then averaged over a range of wedge sizes along the major axis, as well as over the entire azimuth, to generate a series of radial profiles for each line (Law et al. 2021a). Figure 3(d) shows the radial profile extracted from the fiducial spectral image cube of HCN in the HD 163296 disk using a narrow wedge. Similar to the moment maps, the HCN radial profiles show two rings in the inner disk, a plateau or broad ring between 2'' and 3'' and a faint ring between 3'' and 4'', but with a clearer view of the relative fluxes of the different components compared to the moment maps.

Figure 3(e) shows an example of an emission surface, color-coded by brightness temperature. Following, e.g., Rosenfeld et al. (2013), Isella et al. (2018), and Pinte et al. (2018b), emission surfaces are extracted from the image cubes for molecular lines where the front and back sides of the disks can be resolved, resulting in a clearly observed emission asymmetry relative to the major axis. Practically, we used the `disksurf`<sup>30</sup> python package, which has implemented this method together with different data filtering and smoothing capabilities (Law et al. 2021b). This extraction method requires strong emission and high spatial resolution and is only carried out for the brightest emission lines, i.e., the CO 2–1 isotopologues, HCN 3–2, and C<sub>2</sub>H 3–2.

The described VADPs are generated for all lines, disks, and spatial resolutions.

<sup>30</sup> <https://github.com/richteague/disksurf>



**Figure 3.** Illustration of MAPS imaging and image-derived products using the HCN 3–2 line toward the HD 163296 disk as an example. (a) Forty channels of the fiducial-resolution ( $0''.15$ ) spectral line cube with LSRK velocities ( $\text{km s}^{-1}$ ) noted in the upper left corners. (b) Zeroth-moment, rotation, and peak intensity maps generated from the fiducial spectral line cube shown in panel (a). In the rotation map, darker colors correspond to higher absolute velocities. (c) Zeroth-moment map generated from a spectral line cube with a  $0''.3$  taper to enhance sensitivity to weak, large-scale emission. (d) Radial profile of the HCN fiducial zeroth-moment map extracted from a  $15^\circ$  wedge along the disk major axis. (e) The  $z$  vs.  $r$  distribution of HCN emission, where the color encodes the brightness temperature between 12 (blue) and 25 (red) K. The channel maps (panel (a)) and zeroth-moment and peak temperature brightness ( $T_B$ ) maps (panel (b)) are plotted with a power-law color stretch normalized to peak flux in each panel to visualize both weak and strong features. The synthesized beam is shown in the bottom left corner of each panel, and a 20 au scale bar is in the bottom right corner.

### 3.5. Image Repository Description

The image cubes and VADPs are available for download via the ALMA archive<sup>31</sup> or through the MAPS ALMA landing page.<sup>32</sup> An interactive browser for this repository is available on the MAPS project home page.<sup>33</sup> The spectral line cubes and associated products are described in detail in Czekala et al. (2021), and the VADPs are described in Law et al. (2021a, 2021b).

The data are structured hierarchically by [disk]  $\rightarrow$  [spectral setting]  $\rightarrow$  [molecule]  $\rightarrow$  [line], and then each line has available

the relevant windowed measurement set, image cubes (at each available resolution), corresponding VADPs, and scripts needed to replicate each stage of the imaging and VADP process for that line. The continuum-subtracted and non-continuum-subtracted data and products are separated at the spectral setting level. Both primary-beam-corrected and non-primary-beam-corrected images are available, as are the CLEAN masks used for each image. We provide both the  $JvM$ -corrected images (using the noted values of  $\epsilon$ ) and uncorrected images but recommend that the  $JvM$ -corrected images be used to do science.

Images are named

```
[disk]_[molecule]_[spectral setup] _
[line identifier (hyperfine/k-ladder)
```

<sup>31</sup> <https://almascience.nrao.edu/asax/>

<sup>32</sup> <https://almascience.org/alma-data/lp/maps>

<sup>33</sup> <http://www.alma-maps.info>

```
if needed)].[imaging resolution].clean.
[JvMcorr].image.[pbcor].fits,
```

where [JvMcorr] and [pbcor] are present if those corrections were made. Continuum subtraction is noted in the imaging resolution flag (e.g., “0.3arcsec\_wcont”). CLEAN masks are named similarly but with a .mask.fits extension. Radial profiles are named: [disk]\_[molecule]\_[spectral setup]\_[line identifier (hyperfine/k-ladder, if needed)].[imaging resolution].[wedge size]\_radialProfile.txt, where [wedge size] denotes the angular extent of the extraction wedge used (e.g., “15deg”) or “azimuthal” for the full azimuthally averaged profile.

### 3.6. Line Detections

The vast majority of the targeted lines were detected, resulting in  $\sim 200$  line detections across the five disks. Tables 2 and 3 note three cases: detections, tentative detections, and nondetections. We consider a line detected when its integrated emission, stacked spectra (Teague 2019), and/or peak matched filter response is  $>5\sigma$  (Loomis et al. 2018b). A small set of lines were not clearly detected in the image cubes and had a peak matched filter response of  $3\sigma$ – $5\sigma$ . We consider these tentatively detected, and they are labeled as (Y) in the tables.

We detect all targeted CO isotopologue lines (except for  $C^{17}O$ ); all targeted strong HCN,  $C_2H$ , DCN, and CN line components; and  $HCO^+$  1–0, CS 2–1, and  $H_2CO$   $3_{03-2_{02}}$  lines toward all disks. Lines from  $H^{13}CO^+$  1–0,  $HC_3N$  11–10 and 29–28,  $C^{17}O$  1–0,  $N_2D^+$  3–2, all three  $c$ - $C_3H_2$  lines, and the strongest  $CH_3CN$  lines were detected toward three or four disks each and often tentatively detected toward an additional disk. Some of the higher energy levels and therefore weaker  $CH_3CN$  lines were detected toward one to two disks, and two of the targeted  $CH_3CN$  lines were undetected toward all disks. A few additional lines, including  $H^{13}CN$  1–0,  $HC^{15}N$  1–0,  $^{13}CN$  3–2, and  $H_2CO$   $6_{15-6_{16}}$ , were also not detected toward any disks, except for one tentative  $H^{13}CN$  detection toward GM Aur.

Appendix C reports the approximate disk-integrated line intensities (or upper limits) for all disks and lines. Note that these values were generated using an automated script that calculates the flux within the Keplerian CLEAN mask described in Czekala et al. (2021). We hope that this overview is useful for, e.g., observation preparation but do not recommend that it be used for any quantitative analysis. For the latter, we refer the reader to the more precise disk-integrated values and radial disk profiles presented in the individual MAPS papers (Aikawa et al. 2021; Bergner et al. 2021; Cataldi et al. 2021; Guzmán et al. 2021; Ilee et al. 2021; Le Gal et al. 2021; Zhang et al. 2021). Still, these disk-integrated fluxes do provide some useful measures of the range of disk-integrated line fluxes across the sample. The CO 2–1 integrated fluxes are  $\sim 7.8$ – $45$  Jy km  $s^{-1}$ , while the  $^{13}CO$  2–1 and  $C^{18}O$  2–1 line fluxes range between  $\sim 2.3$ – $16$  and  $\sim 0.54$ – $5.8$  Jy km  $s^{-1}$ , respectively. The corresponding 1–0 lines are weaker at  $\sim 0.38$ – $3.6$  and  $\sim 0.073$ – $0.98$  Jy km  $s^{-1}$  for  $^{13}CO$  1–0 and  $C^{18}O$  1–0, respectively. Among the other Band 6 lines, HCN and  $C_2H$  3–2 line fluxes are the highest ( $\sim 1.8$ – $7.5$  and  $0.57$ – $3.5$  Jy km  $s^{-1}$ , respectively), while among the Band 3 lines, the  $HCO^+$  1–0 line is the strongest non-CO line at  $\sim 0.20$ – $1.1$  Jy km  $s^{-1}$ .

The line-emitting areas, characterized as the disk radius that encloses 90% of the flux, are presented in detail by Law et al. (2021a). Here we simply note a few statistics. The line emission

disk radii range from  $\sim 50$  to 500 au. The largest radii are seen for CO 2–1,  $HCO^+$  1–0, CS 1–0, CN 1–0, and  $H_2CO$   $3_{03-2_{02}}$ , which all have radii of 300–500 au in a majority of disks. By contrast,  $CH_3CN$  and  $HC_3N$  present small line emission radii between 50 and 100 au. For individual lines, we do see up to a factor of 5 differences in emission areas between disks.

## 4. Overview of MAPS Results

The purpose of this section is to provide an overview of the results from the 18 MAPS papers following this one and Czekala et al. (2021), and some guidance as to how the individual results fit together. The MAPS papers span a range of topics and are here roughly divided into papers focusing on (1) an empirical analysis of the radial and vertical distribution of line emission (MAPS III–IV), (2) retrieval of molecular column densities and abundances and their interpretation (MAPS V–XIII), and (3) disk dust and gas properties, including nonaxisymmetric structures and dynamics (XIV–XX). When citing any of these results, the reader is requested to reference the original papers: MAPS II–XX (Table 6).

### 4.1. Radial and Vertical Distributions of Molecular Emission

Zeroth-moment maps and radial line emission profiles, and vertical line emission surfaces are presented in Law et al. (2021a) and Law et al. (2021b), respectively, herein referred to as MAPS III and MAPS IV (see also Section 3.4 of this paper for information on how moment maps, emission surfaces, and radial profiles were extracted). Here we present some of the high-level results and illustrative examples.

Figure 4 shows a gallery of zeroth-moment images toward HD 163296. The amount of spatial diversity is astonishing; HD 163296 almost looks like a different disk in each molecular line. The degree of diversity is highlighted in Figure 5 (top row), which shows the zeroth-moment maps together with the radial profiles of five of the brighter molecular lines. Among these five lines, we see one centrally peaked disk with some superimposed shallow rings and gaps ( $^{13}CO$ ), three to four nested rings (HCN and  $C_2H$ ), one compact ring ( $HC_3N$ ), and two very broad rings ( $H_2CO$ ). Different lines clearly respond differently to the local disk environment, which suggests that there are multiple causes of line substructures. Indeed, MAPS III finds that while many of the chemical substructures coincide with dust substructures, pebble disk edges, or inferred snow line locations, others do not. This implies that many chemical substructures observed in disks are caused in whole or in part by additional processes, likely including UV photon fluxes, ionization, radially varying elemental ratios, and gas and dust temperatures.

The diversity of chemical structures observed toward HD 163296 is seen toward the MAPS sample as a whole. Across the full sample, more than 200 emission rings, gaps, and plateaus are detected at all disk radii, from  $\sim 10$  to 700 au. Table 7 lists the numbers of rings and gaps identified toward each disk, considering only the 18 bright lines analyzed in MAPS III, as well as median and lower and upper quartiles for gap and ring radii and widths. Median ring and gap radii vary by a factor of 2–3 between different disks. Ring and gap widths range between  $<10$  (unresolved) and 200 au, but a majority of substructures are  $<100$  au in width; the median widths are 56 and 26 au for rings and gaps, respectively. Finally, ring–gap contrasts vary substantially between lines, between different

**Table 6**  
MAPS Papers

MAPS	Reference	Title
I	This paper	Program Overview and Highlights
II	Czekala et al. (2021)	CLEAN Strategies for Synthesizing Images of Molecular Line Emission in Protoplanetary Disks
III	Law et al. (2021a)	Characteristics of Radial Chemical Substructures
IV	Law et al. (2021b)	Emission Surfaces and Vertical Distribution of Molecules
V	Zhang et al. (2021)	CO Gas Distributions
VI	Guzmán et al. (2021)	Distribution of the Small Organics HCN, C <sub>2</sub> H, and H <sub>2</sub> CO
VII	Bosman et al. (2021a)	Substellar O/H and C/H and Superstellar C/O in Planet-feeding Gas
VIII	Alarcón et al. (2021)	CO Gap in AS 209—Gas Depletion or Chemical Processing?
IX	Ilee et al. (2021)	Distribution and Properties of the Large Organic Molecules HC <sub>3</sub> N, CH <sub>3</sub> CN, and <i>c</i> -C <sub>3</sub> H <sub>2</sub>
X	Cataldi et al. (2021)	Studying Deuteration at High Angular Resolution toward Protoplanetary Disks
XI	Bergner et al. (2021)	CN and HCN as Tracers of Photochemistry in Disks
XII	Le Gal et al. (2021)	Inferring the C/O and S/H Ratios in Protoplanetary Disks with Sulfur Molecules
XIII	Aikawa et al. (2021)	HCO <sup>+</sup> and Disk Ionization Structure
XIV	Sierra et al. (2021)	Revealing Disk Substructures in Multiwavelength Continuum Emission
XV	Bosman et al. (2021b)	Tracing Protoplanetary Disk Structure within 20 au
XVI	Booth et al. (2021)	Characterizing the Impact of the Molecular Wind on the Evolution of the HD 163296 System
XVII	Calahan et al. (2021)	Determining the 2D Thermal Structure of the HD 163296 Disk
XVIII	Teague et al. (2021)	Kinematic Substructures in the Disks of HD 163296 and MWC 480
XIX	Huang et al. (2021)	Spiral Arms, a Tail, and Diffuse Structures Traced by CO around the GM Aur Disk
XX	Schwarz et al. (2021)	The Massive Disk around GM Aurigae

disk locations for the same line and disk, and between disks for the same line and disk radius. The deepest gaps are close to empty with ring–gap contrasts of >90%, but most gaps are more shallow, and the typical contrast is 10%–30%.

Figure 6 shows some examples of the gap and ring diversity observed across the disk sample. This variation is further highlighted in Figure 7 (bottom row), which shows the HCN 3–2 zeroth-moment maps and radial profiles toward the MAPS disks. The HCN emission ranges from faint and broad (IM Lup) to bright and compact (MWC 480) and from multi- to single-ringed. It is currently unclear why the emission morphology is so diverse between the different disks, but we note that we purposefully picked disks with different dust structures, ages, and stellar properties, and it is therefore perhaps not a surprise that the chemical structures are different as well.

Switching from the radial to the vertical dimension, MAPS IV presents the emission heights of CO 2–1 isotopologues, HCN and C<sub>2</sub>H 3–2; empirical 2D temperature models; and an inventory of vertical substructures. The extraction of emission surfaces was briefly described in Section 3.4. The resulting emission height uncertainties strongly depend on the overall line strength, as well as disk radius; the uncertainties are high in the inner disk, where we are resolution-limited, and the outer disk, where we are sensitivity-limited. At intermediate disk radii, the uncertainty can be <10% for the brightest lines, while it varies between 10% and 50% for HCN toward HD 163296 (Figure 3). The CO isotopologue emission heights vary substantially between the five disks, which implies a diverse set of disk vertical density and temperature structures. The HCN and C<sub>2</sub>H emission appears relatively flat, and toward the disks where emission surfaces could be constrained (AS 209, HD 163296, and MWC 480), the emission originates close ( $z/r \sim 0.1$ ) to the midplane. This suggests that the targeted HCN and C<sub>2</sub>H lines enable us to probe organic abundances close to the planet-forming midplane. Identified vertical substructures

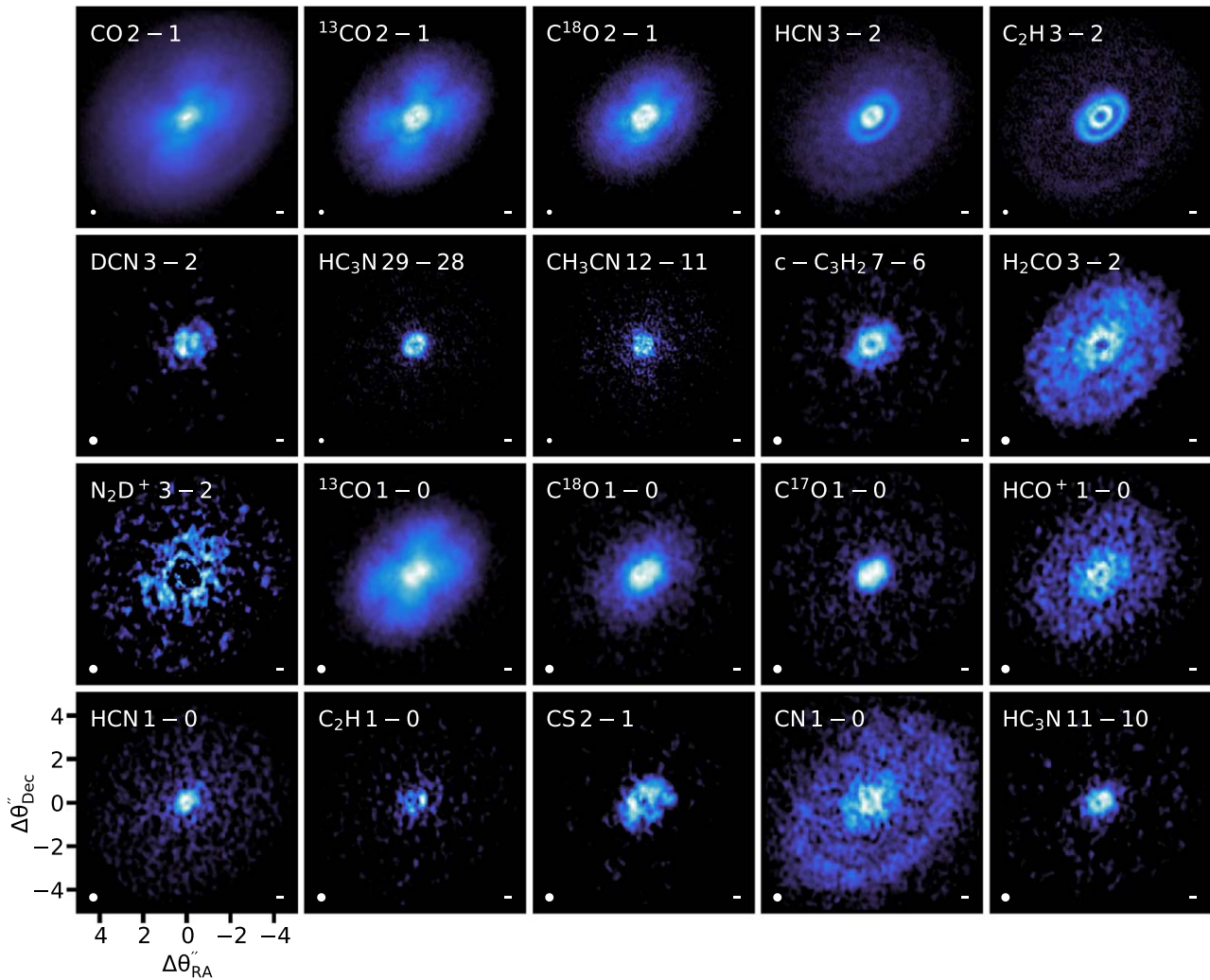
are often associated with disk pressure minima, suggesting that they may be tracers of ongoing planet formation.

#### 4.2. Radial Distributions of C, N, O, and S Carriers, Organics, Ions, and Deuterated Molecules

The most abundant C and O carrier observed by MAPS is CO. Its column density radial profile and inferred depletion patterns toward the five MAPS disks are reported in Zhang et al. (2021), herein MAPS V. CO is inferred to be depleted in the warm molecular layers in all disks, but the degree of depletion varies substantially across and between disks; the nature and distributions of C and O reservoirs may be highly disk-dependent. The CO column density profiles display gaps and cavities. In MAPS V, we use the measured CO gap depths to infer gas gap depths and, further, to compare the relative depths of gas and dust gaps with expectations from planet–disk interaction models. The results are mixed, with some gas-to-dust gap ratios in good agreement with models, while others are off by almost an order of magnitude.

C<sub>2</sub>H and HCN are potential probes of elemental ratios in disks; high C<sub>2</sub>H abundances are only expected when the C/O ratio is elevated (Bergin et al. 2016; Miotello et al. 2019), and HCN formation rates depend on both the gas-phase C/O and N/O ratios (e.g., Cleaves et al. 2018). Together with H<sub>2</sub>CO, C<sub>2</sub>H and HCN are also probes of the disk organic feedstock chemistry. Guzmán et al. (2021), or MAPS VI, present C<sub>2</sub>H, HCN, and H<sub>2</sub>CO column density profiles and use the combined data to evaluate the organic reservoir, with a focus on the inner 50 au of each disk. Our multitransition data constrain C<sub>2</sub>H to warmer disk layers and suggest that HCN is emitting from closer to the planet-forming midplane. There is substantial substructure in the column densities of all three molecules, including single and double rings, gaps, and plateaus, some of which can be associated with proposed planet locations.

In MAPS VII, Bosman et al. (2021a) use the CO and C<sub>2</sub>H results from MAPS V and MAPS VI, respectively, to constrain



**Figure 4.** Twenty molecular faces of the HD 163296 disk. These comprise a representative but nonexhaustive set of zeroth-moment maps toward HD 163296. For those lines with multiple hyperfine lines, the brightest component is shown. The images are shown with a 5–10 mJy km<sup>-1</sup> clip to minimize the visual contribution of noise and a power-law color stretch to emphasize the outer disk fainter structures. The color scale is normalized to the peak intensity in each panel. The synthesized beam (0.15'' or 0.3'') is indicated in the bottom left corner, and a 20 au scale bar is shown in the bottom right corner.

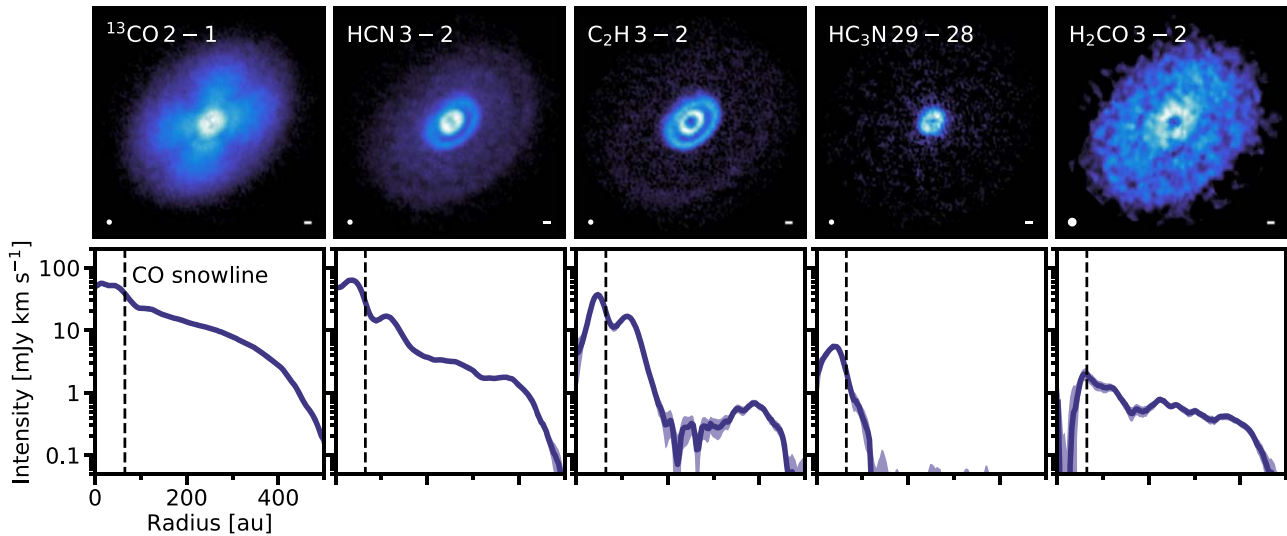
the C/O ratios in three MAPS sources (AS 209, HD 163296, and MWC480) with dust and/or kinematic signs for forming planets. Surprisingly, they find that gas-phase C/O  $\sim 2$  across most of the disks, which implies that CO is not the dominant C carrier in the warm molecular layer. Alongside the constraints on the CO abundance, this suggests that the putative gas giants assembling in these disks may be accreting envelopes with high C/O ratios and substellar O/H or metallicity, resulting in reducing atmospheres.

One of the major dust gaps in the AS 209 disk coincides with substantial CO depletion. The origin of the CO depletion and its implications for planets forming in the gap are explored in more detail by Alarcón et al. (2021) in MAPS VIII. By combining thermochemical models and constraints on the disk pressure profile, MAPS VIII finds that the observed CO depletion is mainly caused by CO chemical processing, rather than a local depletion of gas surface density. This limits the mass of the putative planet in the gap, as the scale of the H<sub>2</sub> surface density perturbations must be less than that seen in the CO surface density profile.

Complementary to MAPS VI, which focuses on small organics, MAPS IX (Ilee et al. 2021) presents the column

density and abundance distributions of the larger organics CH<sub>3</sub>CN, HC<sub>3</sub>N, and *c*-C<sub>3</sub>H<sub>2</sub>. Their column densities in the inner (<50 au) disk regions are  $\sim 10\%$  compared to HCN or C<sub>2</sub>H. Based on excitation temperatures of 20–40 K, CH<sub>3</sub>CN observations probe organic reservoirs that reach down into the planet-forming midplane and therefore provide constraints on the complex organic compositions of forming exocomets and exoplanets, including their prebiotically interesting nitrile budgets.

The origin of solar system nitriles, as well as the utility of deuterated molecules as chemical probes, are the topics of MAPS X, where Cataldi et al. (2021) explore the D/H ratios of HCN and N<sub>2</sub>H<sup>+</sup> in the MAPS disks. They find that the DCN/HCN ratio varies by orders of magnitude across the disk sample, from  $\sim 10^{-1}$  in the outer regions of most disks to  $10^{-3}$  in the inner tens of astronomical units of the MWC 480 disk. By contrast, N<sub>2</sub>D<sup>+</sup> is only detected outside of the CO snow line, and the N<sub>2</sub>D<sup>+</sup>/N<sub>2</sub>H<sup>+</sup> ratio is  $10^{-2}$ –1. The results are best explained by the presence of two distinct deuterium fractionation channels (based on H<sub>2</sub>D<sup>+</sup> and CH<sub>2</sub>D<sup>+</sup>) in disks, with implications toward the origin of deuterium enrichments within solar system bodies, including in comets.



**Figure 5.** Comparisons of emission morphologies between different molecules within the HD 163296 disk. In the top row, zeroth-moment maps are shown with a  $5 \text{ mJy km}^{-1}$  clip and a power-law color stretch to emphasize the outer disk fainter structures. The color scale is normalized to the peak intensity in each panel. For those lines with multiple hyperfine lines, the brightest component is shown. The synthesized beam is indicated in the bottom left corner, and a 20 au scale bar is in the bottom right corner. Bottom row: deprojected and azimuthally averaged radial normalized intensity profiles. The dashed lines mark the estimated CO snow line location.

**Table 7**  
Chemical Substructure Statistics

Source	Rings			Gaps		
	No.	Radius (au)	Width (au)	No.	Radius (au)	Width (au)
IM Lup	28	$146_{89}^{302}$	$93_{76}^{134}$	18	$194_{124}^{275}$	$42_{16}^{56}$
GM Aur	24	$61_{24}^{138}$	$36_{14}^{47}$	54	$98_{51}^{175}$	$24_{14}^{36}$
AS 209	28	$63_{39}^{106}$	$56_{42}^{72}$	15	$70_{42}^{87}$	$24_{18}^{28}$
HD 163296	44	$108_{40}^{233}$	$54_{40}^{100}$	29	$97_{87}^{203}$	$26_{19}^{34}$
MWC 480	25	$78_{67}^{190}$	$56_{42}^{75}$	17	$64_{55}^{164}$	$29_{21}^{43}$
Total	149	$81_{44}^{169}$	$56_{40}^{92}$	93	$97_{58}^{197}$	$26_{19}^{43}$

**Note.** The distributions of radius and width for rings and gaps are given as the lower quartile, median, and upper quartile. We note that the widths are affected by beam convolution. See MAPS III for more details and a full listing of chemical substructures.

The final MAPS paper on nitriles, Bergner et al. (2021), or MAPS XI, uses CN column density profiles and CN/HCN column density ratios to explore disk photochemistry. The CN/HCN ratios increase with disk radius, reaching  $\sim 100$ , such that CN is the dominant nitrile carrier at most disk radii. The CN/HCN ratio is also elevated in some gaps and appears to generally map out UV transparent disk regions. The high CN/HCN ratio observed across most of the disks suggests that photochemistry is key to understanding the overall disk chemical composition.

So far, we have been discussing constraints on the C, N, and O reservoirs, but a fourth important volatile element is sulfur (S), which in disks is most easily traced using CS. In MAPS XII, Le Gal et al. (2021) use CS together with upper limits on SO to independently constrain the C/O ratio to  $>0.9$  in the warm molecular layer (see MAPS VI and VII, which instead make use of  $\text{C}_2\text{H}$  and CO observations). The  $\text{H}_2\text{CS}/\text{CS}$  ratio is measured in the MWC 480 disk and found to be high (on the order of unity), This ratio exceeds model predictions by 2 orders of magnitude and indicates that sulfur participates in the disk organic chemistry at a higher level than expected.

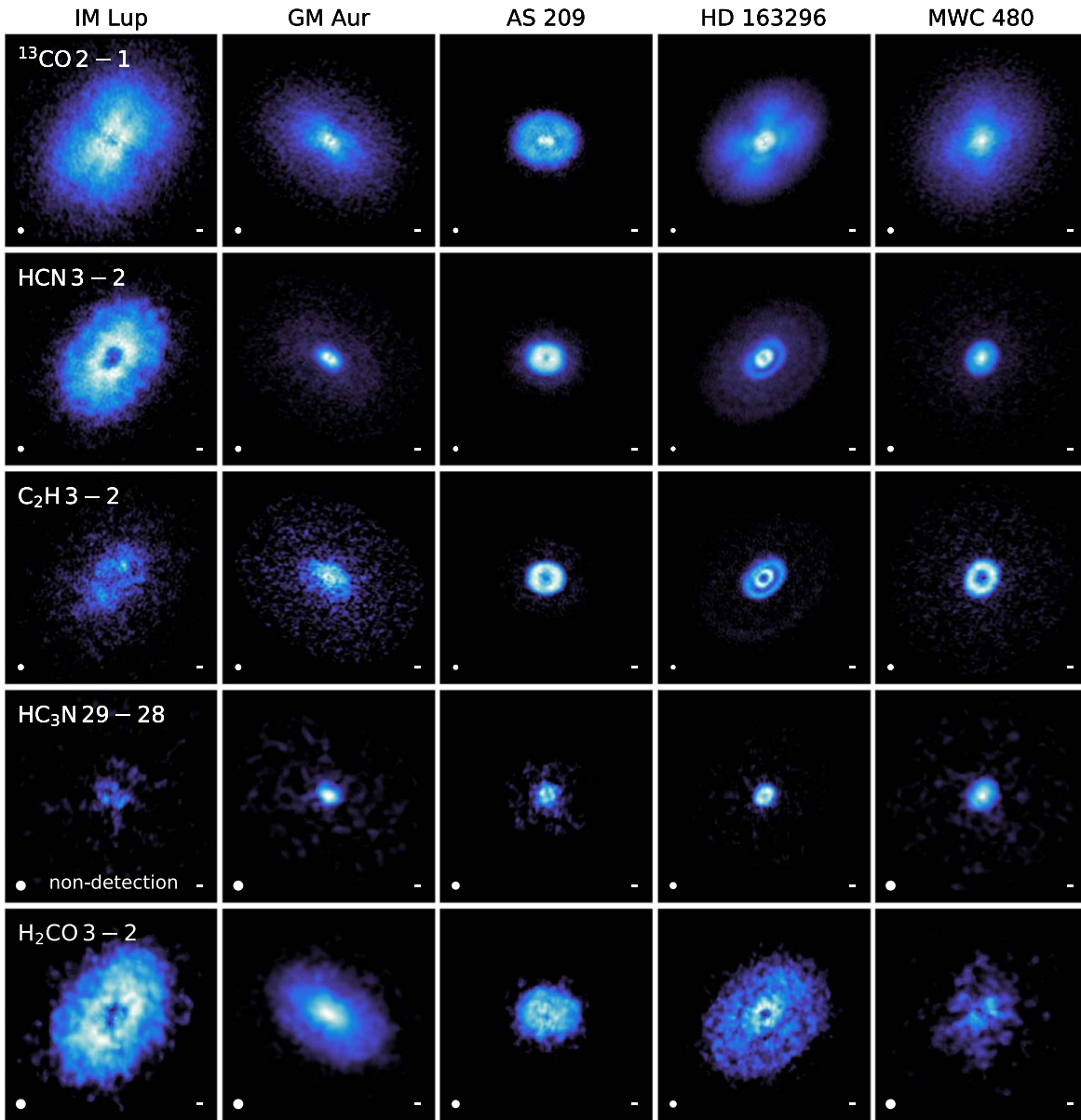
In the final paper in this section, Aikawa et al. (2021), or MAPS XIII, derive  $\text{HCO}^+$  disk column density profiles and combine

these data with  $\text{N}_2\text{H}^+$  and  $\text{N}_2\text{D}^+$  column densities from MAPS X to constrain the ionization fraction across the MAPS disks. The  $\text{HCO}^+$  abundance, and hence the ionization level in the warm molecular layer, is relatively constant across most of the disks. The  $\text{HCO}^+$  is enhanced in some of the more pronounced disk gas gaps (as traced by CO), however, which suggests a higher ionization level in gaps compared to surrounding disk material.

#### 4.3. Disk Dust and Gas Structures, Masses, and Kinematics

While MAPS focuses on gas in disks, our multiwavelength approach also resulted in new constraints on the dust population in the five MAPS disks. In MAPS XIV, Sierra et al. (2021) used multiband continuum observations to constrain the dust size distributions, opacities, and surface densities. The grain sizes often have local maxima in continuum rings, which is consistent with the prevailing theory of dust trapping due to pressure gradients. However, the inferred maximum grain sizes in the rings vary both between rings in the same disk and between disks. Three of the disks are optically thick in the inner disk regions, and in these cases, including scattering strongly affects





**Figure 6.** Zeroth-moment maps of  $^{13}\text{CO}$  2–1, HCN 3–2,  $\text{C}_2\text{H}$  3–2,  $\text{HC}_3\text{N}$  29–28, and  $\text{H}_2\text{CO}$  3–2 toward (left to right) IM Lup, GM Aur, AS 209, HD 163296, and MWC 480. For those lines with multiple hyperfine lines, the brightest component is shown. The angular box sizes are different for the different disks and have been chosen to show the disks on the same physical scales. The small horizontal bar in the lower right corner corresponds to 20 au along the disk major axis. The images are shown with a  $10 \text{ mJy km}^{-1}$  clip and a power-law color stretch to emphasize the outer disk fainter structures. The color scale is normalized to the peak intensity in each panel.

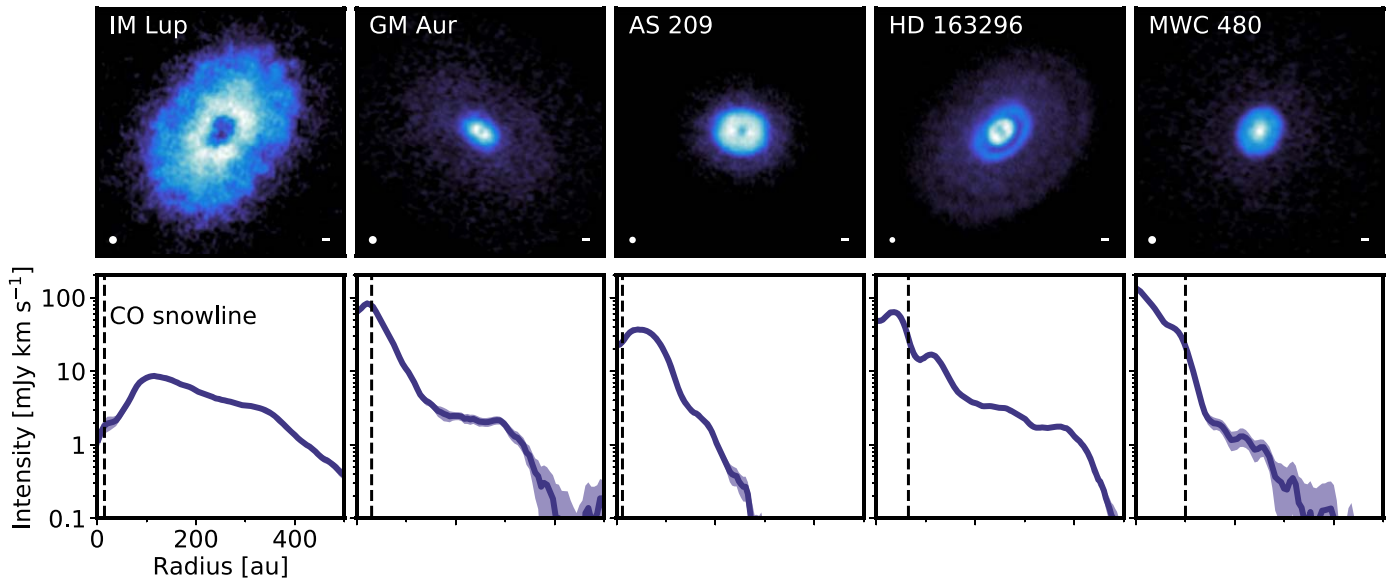
the conclusions, including the inferred degree of grain growth in the inner disk.

MAPS XV (Bosman et al. 2021b) explores the gas and dust in the inner 20 au of disks at 3 au resolution using kinematic information from CO isotopologue line profiles. They use this technique to characterize the dust gaps in the inner 20 au of the AS 209 and HD 163296 disks and found that both are gas-rich. The study also reveals that CO emission is substantially depleted in the inner 20 au of the IM Lup disk, which is best explained by high pebble fluxes from the outer to the inner disk. Such a high pebble flux should promote rapid formation of planetesimals through activation of the streaming instability, as well as efficient formation of planets through pebble accretion.

MAPS XVI (Booth et al. 2021) also constrains the properties of the innermost disk regions, but this time by characterizing

the large-scale outflow identified toward HD 163296 (Klaassen et al. 2013) using multiwavelength CO isotopologue observations. The emission is interpreted as an MHD-driven disk wind, which constrains the launch radius to 4 au. The angular momentum removed by this wind is sufficient to drive the current disk accretion rate, which removes the need to invoke turbulent viscosity in this region of the disk. This has profound implications for the physics and evolution of the inner (<10 au) planet-forming zone of the disk.

The HD 163296 disk is also studied by Calahan et al. (2021) in MAPS XVII. With a detailed model fit to all MAPS observations of CO isotopologues, MAPS XVII reveals the global thermal structure of the disk and constrains the planet-forming mass reservoir. The study also shows that the gaps associated with potential planets should be modestly warmer than their surroundings. This implies that we should expect



**Figure 7.** Comparisons of emission morphologies (top row) and radial intensity profiles (bottom row) of the same molecular line, HCN  $J = 3-2$ ,  $F = 3-2$ , between the five disks. The map sizes have been normalized to the same distance to facilitate comparison in morphology between sources. The dashed lines mark the estimated CO snow line locations toward each disk. The images are shown with a power-law color stretch to emphasize the outer disk fainter structures and normalized to the peak intensity in each panel. The synthesized beam is indicated in the bottom left corner, and a 20 au scale bar is in the bottom right corner.

subtle changes in line brightness temperatures in gas-depleted gaps carved out by massive planets as compared to gas-rich gaps.

MAPS XVIII explores the kinematic substructure of the disks around Herbig Ae stars HD 163296 and MWC 480 and uses the identified velocity patterns to infer the probable presence of nascent planets (Teague et al. 2021). In particular, MWC 480 presents a tightly wound spiral pattern and localized velocity perturbations, which can be explained by a gas giant at  $\sim 250$  au, i.e., well beyond the typical locations of gas-giant planet formation in models. The HD 163296 analysis further strengthens previous kinematic claims of multiple gas giants forming in this massive disk. As a whole, this study further develops the potential of millimeter gas observations as a tool to find and estimate the masses of the youngest planets.

Huang et al. (2021, hereafter MAPS XIX) presented the curious gas structures associated with the GM Aur disk. In addition to a large Keplerian disk, CO emission toward GM Aur presents spiral arms in the outer disk, a tail extending southwest, and diffuse structures surrounding the north side of the disk. One explanation for these large-scale, complex CO structures is late infall of a remnant envelope or cloud material, which may change the overall disk mass budget for planet formation. Further, ongoing interactions of disks with their natal clouds imply that planet-forming material may be of a range of chemical ages and therefore more chemically diverse than typically assumed.

MAPS XX presents a detailed model of the same GM Aur disk to constrain its gas mass and surface density (Schwarz et al. 2021). The analysis includes all MAPS CO data, as well as archival data, for a complete data set of 11 ALMA CO line image cubes and HD 1-0 from Herschel. The best fit is obtained if the disk is cold and massive,  $\sim 0.2 M_{\odot}$ . This would make the GM Aur disk one of the most massive disks discovered to date. The derived disk gas surface density suggests that the disk may be gravitationally unstable in one of the dust rings, between 70 and 120 au.

## 5. Discussion

MAPS observations cover disk scales from  $<10$  to  $\sim 1000$  au. All of these scales are relevant to planet formation. Winds extending thousands of astronomical units from the HD 163296 disk probe the physical conditions at their launch point in the innermost disk regions (MAPS XVI). Spirals extending hundreds of astronomical units beyond the pebble disk likely trace infalling material onto the GM Aur disk, which may affect the mass, chemical makeup, and stability of the pebble disk where planet formation is likely ongoing (MAPS XIX and XX). At intermediate disk radii of 10–200 au, resolved dust and molecular substructure allows us to assess the relationship between dust (MAPS XIV), gas (MAPS V, XV, and XVII), and chemical substructure (MAPS III–VIII) and how they all relate to ongoing planet formation (MAPS XVIII). These intermediate disk radii, which are well resolved in MAPS, are also ideal to explore how disk UV fields, temperatures, ionization, and elemental ratios affect chemistry that may later become incorporated into planet-building solids (MAPS IX–XIII). We note that the disk region most directly relevant to planet formation according to planet formation models is the inner tens of astronomical units of the disk midplane (e.g., Pollack et al. 1996; Raymond et al. 2014; Johansen & Lambrechts 2017). This coincides with the disk regions interior to the CO snow line, which is estimated to occur at 12–100 au in our disks (MAPS V). Interior to the CO snow line, we can, in theory, access the gas composition all the way down to the disk midplane, resulting in direct constraints on the chemistry of planet-forming material.

A detailed discussion of the respective results and their impact on our understanding of planet formation can be found in the individual MAPS papers. Here we provide some discussion relevant for the project as a whole on the chemistry of the planet-forming midplane and the disk organic reservoirs in the main planet-forming disk regions, interactions between planet formation and chemistry, and chemical probes of disk properties and nascent planets.

### 5.1. Chemistry in the Planet-forming Midplane

Planets form in the midplanes of disks, and observations that directly probe midplane material are therefore especially relevant for predicting planet and planetesimal compositions (though see Morbidelli et al. 2014; Teague et al. 2019a, for evidence that planets can also accrete material from elevated disk layers). An important question for a program on the chemistry of planet formation is then: how well can high-resolution millimeter observations probe the disk midplane?

Interior to the CO snow line, CO and related molecules are present in the gas phase at all disk heights, and observations of their respective molecular lines may, in principle, be used to assess the volatile molecular reservoirs and the local disk conditions down to the disk midplane. MAPS IV shows that  $C^{18}O$  generally originates at  $z/r < 0.1$ , close to the midplane in the inner 100 au of disks. In the three disks where the vertical distribution of HCN and  $C_2H$  could be constrained, they too emit from  $z/r \lesssim 0.1$  interior to the snow line. The vertical emission layers of molecules are also constrained by the molecular excitation temperature profiles, which can be used to map out their emitting regions if the overall temperature structure is known (see MAPS IX). Interior to the CO snow line, derived excitation temperatures place most molecules (HCN, DCN,  $C_2H$ , CS, and  $CH_3CN$ ) close to the midplane (MAPS VI, IX, X, and XII). The column densities reported in MAPS V–XIII interior to the CO snow line are then largely probing the chemical conditions in or in close vicinity to the planet-forming midplane.

Exterior to the CO snow line, there are few molecules left in the gas phase in the disk midplane. A handful of molecules, such as  $N_2H^+$ ,  $N_2D^+$  (probed by MAPS X), and  $H_2D^+$ , should still be in the gas phase, and their emission could be used to probe the outermost planet-forming disk regions, including the ongoing deuterium fractionation chemistry (Willacy 2007; Huang & Öberg 2015; Salinas et al. 2017; Aikawa et al. 2018, MAPS X) and ionization levels (MAPS XIII). The midplane elemental and organic compositions between the CO snow line and the pebble disk edge are, however, mostly hidden from view. In the outermost disk regions, beyond the pebble disk edge, UV radiation may penetrate all the way to the disk midplane, releasing some of the frozen-out molecules back into the gas phase (Cleeves et al. 2015; Öberg et al. 2015a) and providing renewed access to the disk chemical composition. This scenario is confirmed by MAPS X and XI. The relevance of these outer disk regions to planet formation is unclear, but the discovery of potential infall onto the outer disk from the surrounding environment in MAPS XIX suggests that the outer disk may not infrequently act as a chemical bridge between the natal cloud environment and the planet-forming regions of the disk.

### 5.2. Organic Reservoirs Interior to 50 au

Within MAPS, we observe a number of small and large organic molecules: HCN,  $C_2H$ ,  $H_2CO$ ,  $c-C_3H_2$ ,  $CH_3CN$ , and  $HC_3N$  (MAPS VI and IX). The total amount of these organics in the gas phase in the inner 50 au of the disks is substantial, up to half an Earth ocean (MAPS VI and IX). However, the true volatile organic reservoir should be considerably larger. First, ALMA can only detect a subset of the organics observed in the remnants of our own disk, i.e., in comets; 48 different organic molecules have been found toward comet 67P to date

(Altwegg et al. 2019), while only 12 (10 at millimeter wavelengths) have been detected in protoplanetary disks (McGuire 2018). Second, and more importantly, the gas organic reservoir directly probed by observations is likely small compared to the organic ice reservoir. Most of the organics are constrained to have excitation temperatures of 30–40 K. This is below the expected freeze-out temperatures of the same molecules, with the possible exception of  $C_2H$  (Wakelam et al. 2012, 2017; Bertin et al. 2017), which suggests that the main organic reservoir will be icy grains and pebbles.

Calculating the precise balance between gas and ice abundances at any one disk location would require a dedicated modeling effort that takes into account both thermal and nonthermal desorption mechanisms. In the meantime, we can use previous models to estimate the order of magnitude of the ice-to-gas ratio. Walsh et al. (2014) reported gas and grain-surface column densities for their fiducial disk as a function of radius and found  $H_2CO$  and  $CH_3CN$  ice-to-gas ratios of  $\sim 10^3$  and a  $HC_3N$  ratio of 4 at 20 au (taken here to be representative of the disk interior to 50 au). Ruaud & Gorti (2019) found higher ratios at 20–50 au of  $\sim 10^5$  for HCN,  $\sim 10^4$  for  $H_2CO$ ,  $\sim 10^7$  for  $CH_3CN$ , and  $\sim 10^5$  for  $HC_3N$ . Öberg et al. (2015a) found HCN ice-to-gas ratios of  $10^2$ – $10^6$  and  $CH_3CN$  ice-to-gas ratios of  $10^4$ – $10^8$ , dependent on the disk turbulence level. If we conservatively adopt an ice-to-gas ratio of  $10^3$  in the disk, we estimate a minimum volatile organic reservoir of 2–460 Earth oceans interior to 50 au in the MAPS disks (Table 8), including only the molecules that are covered by MAPS. The total reservoir of the prebiotically relevant nitriles (Patel et al. 2015) in the same disk region varies between 0.2 and 440 Earth oceans. The basic building blocks of a prebiotic origins-of-life chemistry are plentiful in the comet- and planet-forming regions of protoplanetary disks.

We can compare the abundances of organics to the young solar system by normalizing them to water. We estimate the total water mass  $< 50$  au from the models of each disk in MAPS V and list these estimates in Table 8. These should be seen as order-of-magnitude estimates, since they depend sensitively on the inferred surface densities in the inner regions of these disks, as well as on the fraction of the inherited water that was chemically converted into other species during the disks' lifetime. In our models, all disks start out with water abundances of  $1.8 \times 10^{-4} n_H$ , but after 1 Myr, the abundances vary between 0.25 and  $1.8 \times 10^{-4} n_H$ . In 4/5 disks, both the nitrile and total organics abundances are  $\sim 1\%$  compared to  $H_2O$ . For nitriles, this is in good agreement with solar system comet values (Mumma & Charnley 2011; Altwegg et al. 2019; Drozdovskaya et al. 2019). We note that the nitrile/(total organics) ratio in our disks is considerably higher than in most comets (67P excluded), which suggests that while the in situ production of nitriles in disks may account for much of the final nitrile budget, other sources are needed for oxygen-bearing organics. They may be in large part inherited from the previous star formation stages (Drozdovskaya et al. 2019; Öberg & Bergin 2021).

### 5.3. Links between Dust and Chemical Substructures

One of the fundamental questions targeted by MAPS is the link between ongoing planet formation, as traced by millimeter continuum substructures, and gas and chemical substructures. More specifically, with MAPS, we begin to address the following questions: How is the gas distributed across disks

**Table 8**  
Minimum Volatile Organic Reservoirs <50 au<sup>a</sup>

Source	Water [No. Earth Oceans]	Nitriles [No. Earth Oceans]	All Organics [No. Earth Oceans]	Nitriles [% H <sub>2</sub> O]	All Organics [% H <sub>2</sub> O]
IM Lup	240,000	0.20	2.0	$8.1 \times 10^{-5}$	$8.3 \times 10^{-4}$
GM Aur	25,000	150	170	0.60	0.69
AS 209	1300	21	47	1.6	3.5
HD 163296	49,000	340	390	0.70	0.79
MWC 480	96,000	440	460	0.46	0.48
Comet 67P				0.17 <sup>b</sup>	0.83 <sup>c</sup>

**Notes.**

<sup>a</sup> Assuming a 1000-to-1 ice-to-gas ratio of volatile organics.

<sup>b</sup> Summing up the abundances of all organics with a CN group in Drozdovskaya et al. (2019).

<sup>c</sup> Summing up the abundances of all volatile organics listed in Drozdovskaya et al. (2019).

with dust substructures? Is the chemistry in gaps distinct compared to the surrounding disks? Are line-emitting temperatures affected by dust gaps? Is there a link between snow lines and other chemical substructures?

Despite numerous pieces of theoretical and observational evidence for CO redistribution and depletion in disks (Reboussin et al. 2015; Miotello et al. 2017; Yu et al. 2017; Bosman et al. 2018; Dodson-Robinson et al. 2018; Schwarz et al. 2018; Zhang et al. 2019; Krijt et al. 2020), CO remains the overall best tracer of the gas distribution in disks (Molyarova et al. 2017). We find that there is some correlation between dust gaps and CO column density gaps, but there are also several deep dust gaps with no visible CO and, by inference, gas depletion in them (MAPS V). This suggests that not all dust gaps are created by the same mechanism, and that the inferred gas depth profiles could be used to constrain the origin of the dust gap, including the mass of any putative planet (Kanagawa et al. 2015; Zhang et al. 2018). The use of CO to trace the gas properties of dust gaps is complicated, however, by evidence of CO depletion. In particular, the large C<sub>2</sub>H abundances observed in several disks are best explained by a substantial CO removal from the gas. This implies that the observed CO column density decreases in some dust gaps may be due in part to chemical CO depletion rather than gas depletion (MAPS VII and VIII), which entails that the inferred gas depletions in dust gaps are really upper limits.

Based on theoretical models, the emitting temperature of gas in gaps may either be cold compared to nearby disk regions because of gas–dust decoupling, shadowing, or an emitting layer that is closer to the disk midplane (Jang-Condell 2008; Facchini et al. 2018; Alarcón et al. 2020) or warm because the gap heating–cooling balance is different compared to the surrounding disk (van der Marel et al. 2018; Teague et al. 2019b; Alarcón et al. 2020, MAPS XVII). In MAPS, most gaps are not associated with a change in temperature as measured by line intensities of optically thick lines (MAPS IV), but there are some exceptions. One of the gaps in the HD 163296 disk and one of the gaps in the MWC 480 disk are each characterized by a lower CO excitation temperature compared to the surrounding disk (MAPS IV, XVIII). Because of the relatively low resolution of Band 3 observations, we were unable to constrain changes in the excitation temperature across gaps using multiline analysis.

There is also no consistent association between dust gaps and rings and between the gaps and rings seen in molecular lines other than CO. At least, this is the case when comparing

dust and gas substructures, regardless of the contrast or width of the dust gap or ring. If we instead focus on the innermost dust gap of each disk that is clearly seen in the MAPS continuum data (D116 in IM Lup, D15 in GM Aur, D61 in AS 209, D49 in HD 163296, and D76 in MWC 480; see Huang et al. 2018b, for notation), a somewhat more coherent picture emerges, where dust depletion is associated with an excess of nitriles and hydrocarbons (MAPS III) indicative of oxygen-depleted gaps (MAPS VII). It is curious, however, that in, e.g., HD 163296, the very next major dust gap is instead associated with a gap in nitriles and hydrocarbons, indicating that gaps that appear similar in continuum may be diverse in their gas and chemistry. The cause of this diversity is unclear, and future dedicated modeling efforts are needed to better understand the link between dust sculpting and chemistry.

Snow lines may cause chemical substructures because they dramatically change the molecular abundance of the molecule in question, and also because they affect the gas elemental composition. The MAPS resolution enables us to probe chemical changes across the CO and N<sub>2</sub> snow lines. However, we only have independent constraints on CO snow line locations in the GM Aur and HD 163296 disks and on the N<sub>2</sub> snow line toward the GM Aur disk (Qi et al. 2015, 2019). With these caveats in mind, it is still noteworthy that we see no consistent link between inferred CO snow line locations and dust or chemical substructure (MAPS III). This is consistent with the previous results of Huang et al. (2018b) and Long et al. (2018) comparing dust substructure and inferred snow line locations toward larger samples of disks, as well as a recent in-depth chemical exploration of the transition disk around AB Aur (Rivière-Marichalar et al. 2020). These results together suggest that either our current estimates of snow line locations are inaccurate,<sup>34</sup> or the impact of snow lines on the radial chemical profiles is modest. The latter may point to a chemical disconnect between the midplane and warm molecular layers beyond the CO snow line. This is supported by the observation that many chemical substructures in the outer disk also do not coincide with dust substructures (MAPS III), which also are located in the midplane.

Since many chemical substructures cannot be explained by dust substructures or snow lines, we need to also consider other disk characteristics that can cause chemical substructures. For

<sup>34</sup> Temperature profiles of disks depend sensitively on assumptions about the small grain population that are not well constrained, and this, together with a range of possible CO freeze-out temperatures, makes snow line locations difficult to infer.

example, gradients in disk properties such as UV radiation flux (MAPS XI), ionization, and temperature may result in radial locations that are particularly favorable or unfavorable to the formation of a specific molecule, and chemical substructures may emerge as a powerful probe of such disk characteristics.

#### 5.4. Molecular Probes of Planet Formation

In addition to constituting probes of disk chemistry, molecular line emission can be used to constrain several disk properties that are important to planet formation, such as gas mass, kinematics, temperature, snow line locations, and ionization, and have been proposed to enable detections of nascent planets. Deploying disk kinematic planet detection methods (Disk Dynamics Collaboration et al. 2020), the MAPS data have resulted in the possible identification of a new planet in MWC 480 and additional dynamical data on the previously proposed planets in the HD 163296 disk (MAPS XVIII). On larger scales, MAPS XVI characterized the dynamics of the HD 163296 molecular wind, which also constrains the dynamics of the innermost regions of the disk. Toward GM Aur, MAPS XIX found evidence of an ongoing interaction between the disk and surrounding material with implications for the disk composition, structure, and dynamics. These interactions with the environment resemble what is seen toward younger sources (see Alves et al. 2020; Pineda et al. 2020, for recent examples). We note that all studies of dynamics in MAPS (XVI, XVIII, and XIX) are based on  $^{12}\text{CO}$  and  $^{13}\text{CO}$  lines. Whether it will be possible to identify forming planets and other dynamical phenomena using lines of less abundant molecules (e.g., Cleeves et al. 2015) remains to be seen, but it may very well require deeper observations than were pursued with MAPS or observations of other strong lines such as CN, CS, and  $\text{HCO}^+$  in Band 6 or Band 7.

The disk gas mass places fundamental constraints on what kind of planetary system can form in a disk, and statistics on gas masses are needed to provide an interpretive framework for exoplanet demographics. There is currently no single reliable tracer of disk gas mass; i.e., commonly used ones such as CO isotopologues (Williams & Best 2014; Miotello et al. 2016; Bergin & Williams 2017), HD (Bergin et al. 2013; McClure et al. 2016), and dust edge locations (Powell et al. 2019) all have their limitations. MAPS XX uses two of the above constraints together with a grid of thermochemical models to determine the GM Aur gas mass. With no far-IR mission currently planned, and considering that the number of disks for which Herschel HD constraints exist is small, we will need to develop additional disk mass tracers to obtain statistics on disk masses.

The disk temperature structure determines the locations of snow lines and affects the formation and migration of planets. Despite a long recognition of its importance, it has been elusive to constrain. Spatially resolved, optically thick CO lines have been used in a handful of case studies to constrain the disk temperature structure (Dartois et al. 2003; Zhang et al. 2017; Isella et al. 2018; Pinte et al. 2018b). In MAPS, we developed a semiautomatic workflow to map out 2D disk temperatures (MAPS IV). This works well and is an attractive approach to obtain model-independent disk temperature structures. We note that the utility of this method depends strongly on the inclination of the disk and the spatial resolution, which will limit how quickly we can build up a large library of such empirical disk temperatures. Once such a library exists, disk

thermochemical models are key to providing the interpretive framework, as is illustrated by MAPS XVII.

Snow lines can sometimes be probed using the volatile of interest (e.g., Schwarz et al. 2016), but most of the time, we rely on chemical tracers such as  $\text{N}_2\text{H}^+$  or  $\text{N}_2\text{D}^+$  for CO and  $\text{N}_2$  snow lines (Qi et al. 2013, 2019; Cataldi et al. 2021) and  $\text{HCO}^+$  for  $\text{H}_2\text{O}$  snow lines (Jørgensen et al. 2013; Visser et al. 2015; van 't Hoff et al. 2018a, 2018b; Leemker et al. 2021). These chemical tracers are needed to resolve ambiguities between snow lines and changes in gas surface densities and because many common disk volatiles are difficult or impossible to observe at millimeter wavelengths, including  $\text{H}_2\text{O}$ ,  $\text{CO}_2$ ,  $\text{NH}_3$ , and  $\text{N}_2$ .

Ionization levels in disks are most directly probed by observing the lines from major ions. MAPS included lines from two ions,  $\text{HCO}^+$  and  $\text{N}_2\text{D}^+$ , that are proposed to be major charge carriers in the warm molecular and cold midplane layers, respectively. We note that, based on MAPS,  $\text{N}_2\text{D}^+$  lines appear generally detectable in large disks with a few hours of integration, providing a window into ionization in the outer disk midplane. The 1–0 line of  $\text{HCO}^+$  was readily detected in all disks, while the  $^{13}\text{C}$  isotopologue was more challenging to observe but still detected in some disks (MAPS XIII). Together, the two isotopologues provided good constraints on ionization in the outer disk warm molecular layer. What remains to be constrained is the ionization level in the inner 20–40 au in disks, which will likely require additional observations of the brighter, higher-frequency  $\text{HCO}^+$  lines.

## 6. Conclusions

MAPS set out to survey the distributions of common molecules in five disks around three T Tauri and two Herbig Ae stars—IM Lup, GM Aur, AS 209, HD 163296 and MWC 480—in unprecedented detail with ALMA and to develop an interpretive framework for the observations. Our main findings are as follows.

1. The imaging process and the production of higher-level data products required substantial development compared to previous best practices, and we recommend that other projects pursuing high-resolution spectral imaging adopt and build on our integrated workflow, which is described in detail in MAPS II.
2. All molecules surveyed by MAPS at high spatial resolution (7–30 au) present some substructure, resulting in over 200 identified rings, gaps, and plateaus. This suggests that disk gas properties, including the chemical composition, vary substantially on small scales in disks, and therefore that planets may form in chemically distinct environments.
3. The MAPS spatial scales also enabled constraints on the vertical emission and temperature profiles. The resulting empirical 2D temperature structures are key to anchoring disk models and deriving the temperatures of the planet-forming disk midplanes.
4. The CO gas-phase abundances vary dramatically across the MAPS disks and are depleted by 1–2 orders of magnitude at most disk locations compared to the interstellar canonical value. The C/H and O/H ratios are therefore substellar. In addition, the C/O gas-phase ratio is elevated above unity in many of the disks, with implications for predicted planet envelope compositions. The MAPS molecular inventory

also includes probes of the N and S reservoirs, and we present some initial constraints, but more theoretical work is needed to derive quantitative abundance patterns.

5. MAPS covered six small and mid-sized organic molecules: HCN, C<sub>2</sub>H, H<sub>2</sub>CO, HC<sub>3</sub>N, CH<sub>3</sub>CN, and *c*-C<sub>3</sub>H<sub>2</sub>. Their radial distributions are different, indicating a changing organic inventory with disk radius. Within 50 au, the inferred organic inventory is large, corresponding to many Earth oceans, and planets forming in these disks are assembling in an organically rich environment.
6. MAPS included probes of deuterium fractionation, photochemistry, and ionization, which are all important to interpret the volatile reservoirs in the solar system and predict the volatile content of exoplanets. In particular, MAPS has enabled high-resolution constraints on the distribution of deuterium chemistry, photochemical products, and ionization levels, including their distributions at radii directly relevant for planet and comet formation.
7. While not an original motivation for MAPS, the MAPS CO data have revealed multiple pieces of evidence for the dynamic nature of these protoplanetary disk systems including disk winds, gas spirals, and azimuthal asymmetries that we could connect with ongoing planet formation. Furthermore, MAPS has enabled us to further develop kinematic planet detection methods and resulted in the possible localization of a planet in the MWC 480 disk.

Together, these results demonstrate the utility of deep, high-resolution ALMA observations of molecular lines in disks to explore the chemistry that affects and probes planet formation. Going forward, we will need to expand this approach to larger samples of representative disks around a range of stars, including the frequently planet-hosting M dwarfs, to obtain statistically meaningful constraints on the chemistry of planet formation.

The authors thank the anonymous referee for valuable comments that improved both the content and presentation of this work. This paper makes use of the following ALMA data: ADS/JAO.ALMA#2018.1.01055.L. ALMA is a partnership of ESO (representing its member states), NSF (USA) and NINS (Japan), together with NRC (Canada), MOST and ASIAA (Taiwan), and KASI (Republic of Korea), in cooperation with the Republic of Chile. The Joint ALMA Observatory is operated by ESO, AUI/NRAO and NAOJ. The National Radio Astronomy Observatory is a facility of the National Science Foundation operated under cooperative agreement by Associated Universities, Inc.

K.I.Ö. acknowledges support from the Simons Foundation (SCOL No. 321183) and an NSF AAG grant (No. 1907653). V.V.G. acknowledges support from FONDECYT Iniciación 11180904 and ANID project Basal AFB-170002. C.W. acknowledges financial support from the University of Leeds, Science and Technology Facilities Council of the United Kingdom (STFC), and UKRI (grant Nos. ST/R000549/1, ST/T000287/1, MR/T040726/1). Y.A. acknowledges support by NAOJ ALMA Scientific Research grant code 2019-13B and Grant-in-Aid for Scientific Research 18H05222 and 20H05847. E.A.B., A.D.B., and F.A. acknowledge support from NSF AAG grant No. 1907653. C.J.L. acknowledges funding from the National Science Foundation Graduate Research Fellowship under grant DGE1745303. S.M.A. and J.H. acknowledge funding support from the National Aeronautics and Space

Administration under grant No. 17-XRP17 2-0012 issued through the Exoplanets Research Program. J.B. acknowledges support by NASA through NASA Hubble Fellowship grant No. HST-HF2-51427.001-A awarded by the Space Telescope Science Institute, which is operated by the Association of Universities for Research in Astronomy, Inc., under NASA contract NAS5-26555. J.B.B. acknowledges support from NASA through NASA Hubble Fellowship grant No. HST-HF2-51429.001-A, awarded by the Space Telescope Science Institute, which is operated by the Association of Universities for Research in Astronomy, Inc., for NASA, under contract NAS5-26555. Y.B. acknowledges funding from ANR (Agence Nationale de la Recherche) of France under contract No. ANR-16-CE31-0013 (Planet-Forming-Disks). A.S.B. acknowledges the studentship funded by the STFC. J.K.C. acknowledges support from the National Science Foundation Graduate Research Fellowship under grant No. DGE 1256260 and the National Aeronautics and Space Administration FINESST grant, under grant No. 80NSSC19K1534. G.C. is supported by NAOJ ALMA Scientific Research grant code 2019-13B. L.I.C. gratefully acknowledges support from the David and Lucile Packard Foundation, Johnson & Johnson's WiSTEM2D Program, and NASA ATP 80NSSC20K0529. I.C. was supported by NASA through the NASA Hubble Fellowship grant HST-HF2-51405.001-A awarded by the Space Telescope Science Institute, which is operated by the Association of Universities for Research in Astronomy, Inc., for NASA, under contract NAS5-26555. J.H. acknowledges support for this work provided by NASA through NASA Hubble Fellowship grant No. HST-HF2-51460.001-A awarded by the Space Telescope Science Institute, which is operated by the Association of Universities for Research in Astronomy, Inc., for NASA, under contract NAS5-26555. J.D.I. acknowledges support from the STFC under ST/T000287/1. N.T.K. acknowledges support provided by the Alexander von Humboldt Foundation in the framework of the Sofja Kovalevskaja Award endowed by the Federal Ministry of Education and Research. R.L.G. acknowledges support from a CNES fellowship grant. Y.L. acknowledges the financial support by the National Science Foundation of China (grant No. 11973090). F.L. acknowledges support from the Smithsonian Institution as a Submillimeter Array (SMA) Fellow. F.M. acknowledges support from the ANR of France under contracts ANR-16-CE31-0013 (Planet-Forming-Disks) and ANR-15-IDEX-02 (through CDP "Origins of Life"). H.N. acknowledges support by NAOJ ALMA Scientific Research grant code 2018-10B and Grant-in-Aid for Scientific Research 18H05441. L.M.P. acknowledges support from ANID project Basal AFB-170002 and ANID FONDECYT Iniciación project No. 11181068. K.R.S. acknowledges the support of NASA through Hubble Fellowship Program grant HST-HF2-51419.001, awarded by the Space Telescope Science Institute, which is operated by the Association of Universities for Research in Astronomy, Inc., for NASA, under contract NAS5-26555. A.S. acknowledges support from ANID/CONICYT Programa de Astronomía Fondo ALMA-CONICYT 2018 31180052. R.T. acknowledges support from the Smithsonian Institution as a Submillimeter Array (SMA) Fellow. T.T. is supported by JSPS KAKENHI grant Nos. JP17K14244 and JP20K04017. Y.Y. is supported by IGPEES, WINGS Program, the University of Tokyo. M.L.R.H. acknowledges support from the Michigan Society of Fellows. A.R.W. acknowledges support from the Virginia Space Grant Consortium and the National Science Foundation Graduate

Research Fellowship Program under grant No. DGE1842490. K.Z. acknowledges the support of the Office of the Vice Chancellor for Research and Graduate Education at the University of Wisconsin—Madison with funding from the Wisconsin Alumni Research Foundation and the support of NASA through Hubble Fellowship grant HST-HF2-51401.001, awarded by the Space Telescope Science Institute, which is operated by the Association of Universities for Research in Astronomy, Inc., for NASA, under contract NAS5-26555.

*Facility:* ALMA.

*Software:* Astropy (Astropy Collaboration et al. 2018), *bettermoments* (Teague & Foreman-Mackey 2018), CASA (McMullin et al. 2007), *disksurf* (<https://github.com/richteague/disksurf>), *GoFish* (Teague 2019), *Matplotlib* (Hunter 2007), *NumPy* (van der Walt et al. 2011).

## Appendix A Observational Details

Tables 9 and 10 list all ALMA executions carried out as a part of MAPS. Table 9 lists the Band 3 executions, and Table 10 summarizes the Band 6 executions. These tables include observing dates, number of antennas, on-source integration times, baselines, observatory-estimated spatial resolution, maximum recoverable scale, and phase and flux calibrators. We note that GM Aur and MWC 480 were always observed in the same execution with the integration time split evenly between the two sources. The total number of executions was 90. Each execution included 36–52 minutes of on-source integration (with the exception of short 11–17 minute integrations).

**Table 9**  
Details of Band 3 Observations

Setting	Target	Date	No. Ant.	Int. (minutes)	Baselines (m)	Res.	Max. Scale	Phase Cal.	Flux Cal.
B3-1	IM Lup	2018 Oct 29	48	37	15–1398	0″60	8″5	J1610–3958	J1427–4206
		2019 Aug 20	43	38	41–3396	0″22	3″7	J1610–3958	J1517–2422
		2019 Aug 21	44	38	41–3638	0″22	3″6	J1610–3958	J1517–2422
GM Aur/MWC 480		2018 Dec 13	42	46	15–783	1″0	13″	J0438+3004	J0510+1800
		2018 Dec 15	42	47	15–740	1″0	12″	J0438+3004	J0510+1800
		2019 Aug 31	43	46	38–3396	0″23	3″8	J0459+3106	J0510+1800
		2019 Sep 2	43	52	38–3638	0″23	3″7	J0438+3004	J0510+1800
		2019 Sep 2	31	52	38–3638	0″23	3″8	J0512+2927	J0510+1800
		2019 Sep 4	43	50	38–3638	0″23	3″8	J0438+3004	J0510+1800
		2019 Sep 4	43	50	38–3638	0″23	3″8	J0438+3004	J0510+1800
AS 209		2018 Oct 26	49	36	15–1398	0″60	8″6	J1733–1304	J1517–2422
		2019 Aug 23	43	38	43–3396	0″23	3″3	J1653–1551	J1550+0527
		2019 Aug 24	44	38	43–3396	0″22	3″2	J1653–1551	J1517–2422
		2019 Sep 4	46	38	38–3144	0″23	4″0	J1653–1551	J1517–2422
		2019 Sep 4	48	38	38–3637	0″23	3″8	J1653–1551	J1517–2422
HD 163296		2018 Oct 22	48	36	15–1398	0″60	8″4	J1743–1658	J1924–2914
		2019 Aug 23	43	37	41–3144	0″23	3″7	J1755–2232	J1924–2914
		2019 Aug 24	45	37	41–3396	0″23	3″3	J1755–2232	J1517–2422
		2019 Aug 25	45	37	41–3396	0″23	3″8	J1755–2232	J1924–2914
		2019 Sep 4	46	37	38–3144	0″23	4″0	J1755–2232	J1924–2914
		2019 Sep 5	49	37	38–3638	0″22	3″8	J1755–2232	J1924–2914
B3-2	IM Lup	2018 Nov 6	47	37	15–1398	0″60	9″7	J1610–3958	J1427–4206
		2019 Aug 22	45	38	41–3638	0″23	3″6	J1610–3958	J1517–2422
		2019 Aug 22	46	38	41–3638	0″23	3″8	J1610–3958	J1517–2422
GM Aur/MWC 480		2018 Dec 15	45	34	15–740	1″0	12″	J0438+3004	J0510+1800
		2018 Dec 15	45	34	15–740	1″0	12″	J0438+3004	J0510+1800
		2019 Apr 15	44	34	15–783	1″0	14″	J0438+3004	J0510+1800
		2019 Aug 30	48	49	38–3396	0″24	3″9	J0438+3004	J0237+2848
		2019 Aug 30	48	49	38–3396	0″24	3″9	J0438+3004	J0510+1800
		2019 Aug 30	47	49	38–3396	0″23	3″9	J0438+3004	J0510+1800
		2019 Sep 1	47	11	38–3338	0″23	3″8	J0519+2744	J0510+1800
		2019 Sep 1	52	49	38–3638	0″23	3″8	J0438+3004	J0510+1800
AS 209		2018 Oct 27	48	36	15–1398	0″60	8″7	J1733–1304	J1517–2422
		2019 Aug 23	44	37	41–3638	0″23	3″9	J1653–1551	J1517–2422
		2019 Aug 23	44	37	41–3396	0″23	3″6	J1653–1551	J1924–2914
		2019 Sep 17	41	37	41–3638	0″24	3″9	J1653–1551	J1924–2914
HD 163296		2018 Oct 25	49	36	15–1398	0″61	9″0	J1743–1658	J1924–2914
		2019 Aug 19	47	37	41–3638	0″24	3″9	J1755–2232	J1924–2914
		2019 Aug 22	46	37	41–3638	0″23	3″6	J1755–2232	J1924–2914
		2019 Sep 6	46	37	41–3638	0″23	3″6	J1755–2232	J1924–2914

**Table 10**  
Details of Band 6 Observations

Setting	Target	Date	No. Ant.	Int. (minutes)	Baselines (m)	Res.	Max. Scale	Phase Cal.	Flux Cal.
B6-1	IM Lup	2018 Nov 28	44	37	15–1241	0 <sup>''</sup> 36	4 <sup>''</sup> 8	J1610–3958	J1427–4206
		2019 Aug 12	42	44	41–3638	0 <sup>''</sup> 10	1 <sup>''</sup> 6	J1610–3958	J1517–2422
		2019 Aug 12	43	44	41–3638	0 <sup>''</sup> 10	1 <sup>''</sup> 6	J1610–3958	J1517–2422
		2019 Aug 14	43	44	41–3638	0 <sup>''</sup> 10	1 <sup>''</sup> 7	J1610–3958	J1517–2422
	GM Aur/MWC 480	2018 Oct 30	48	40	15–1398	0 <sup>''</sup> 26	3 <sup>''</sup> 8	J0438+3004	J0510+1800
		2018 Nov 17	48	40	15–1398	0 <sup>''</sup> 26	3 <sup>''</sup> 8	J0438+3004	J0510+1800
		2018 Nov 23	49	40	15–1398	0 <sup>''</sup> 26	3 <sup>''</sup> 8	J0438+3004	J0510+1800
		2019 Aug 26	49	47	41–3638	0 <sup>''</sup> 10	1 <sup>''</sup> 6	J0438+3004	J0510+1800
		2019 Aug 26	49	48	41–3638	0 <sup>''</sup> 10	1 <sup>''</sup> 6	J0438+3004	J0510+1800
		2019 Aug 27	50	48	41–3638	0 <sup>''</sup> 10	1 <sup>''</sup> 6	J0439+3045	J0510+1800
		2019 Aug 28	50	48	38–3638	0 <sup>''</sup> 10	1 <sup>''</sup> 6	J0439+3045	J0510+1800
		2019 Aug 28	50	48	38–3638	0 <sup>''</sup> 10	1 <sup>''</sup> 6	J0439+3045	J0510+1800
	AS 209	2018 Dec 2	44	41	15–784	0 <sup>''</sup> 43	5 <sup>''</sup> 3	J1733–1304	J1751+0939
		2019 Aug 15	46	43	41–3638	0 <sup>''</sup> 10	1 <sup>''</sup> 7	J1653–1551	J1427–4206
		2019 Aug 16	46	43	41–3638	0 <sup>''</sup> 10	1 <sup>''</sup> 7	J1653–1551	J1517–2422
		2019 Aug 16	45	43	41–3638	0 <sup>''</sup> 10	1 <sup>''</sup> 6	J1653–1551	J1517–2422
HD 163296	2018 Dec 4	43	41	15–784	0 <sup>''</sup> 44	5 <sup>''</sup> 9	J1733–1304	J1924–2914	
	2019 Aug 16	45	43	41–3638	0 <sup>''</sup> 10	1 <sup>''</sup> 6	J1755–2232	J1924–2914	
	2019 Aug 16	47	43	41–3638	0 <sup>''</sup> 10	1 <sup>''</sup> 6	J1755–2232	J1924–2914	
	2019 Aug 17	47	43	41–3638	0 <sup>''</sup> 10	1 <sup>''</sup> 6	J1755–2232	J1924–2914	
B6-2	IM Lup	2019 Apr 7	43	16	15–500	0 <sup>''</sup> 57	6 <sup>''</sup> 1	J1610–3958	J1517–2422
		2019 Apr 9	43	36	15–500	0 <sup>''</sup> 56	6 <sup>''</sup> 0	J1610–3958	J1924–2914
		2019 Aug 21	44	47	41–3396	0 <sup>''</sup> 09	1 <sup>''</sup> 4	J1733–1304	J1924–2914
		2019 Aug 25	45	47	41–3396	0 <sup>''</sup> 09	1 <sup>''</sup> 4	J1755–2232	J1924–2914
		2019 Aug 26	45	47	41–3638	0 <sup>''</sup> 08	1 <sup>''</sup> 4	J1755–2232	J1924–2914
	GM Aur/MWC 480	2018 Oct 31	47	47	15–1398	0 <sup>''</sup> 22	3 <sup>''</sup> 4	J0438+3004	J0510+1800
		2018 Oct 31	47	47	15–1398	0 <sup>''</sup> 22	3 <sup>''</sup> 4	J0438+3004	J0510+1800
		2019 Aug 8	42	47	41–5894	0 <sup>''</sup> 08	1 <sup>''</sup> 2	J0438+3004	J0510+1800
		2019 Aug 15	48	47	41–3638	0 <sup>''</sup> 09	1 <sup>''</sup> 4	J0438+3004	J0510+1800
		2019 Aug 15	48	47	41–3638	0 <sup>''</sup> 09	1 <sup>''</sup> 4	J0438+3004	J0510+1800
		2019 Aug 18	43	47	41–3638	0 <sup>''</sup> 08	1 <sup>''</sup> 3	J0438+3004	J0510+1800
		2019 Aug 20	49	47	41–3638	0 <sup>''</sup> 08	1 <sup>''</sup> 2	J0438+3004	J0510+1800
	2019 Aug 21	43	47	41–3189	0 <sup>''</sup> 09	1 <sup>''</sup> 4	J0438+3004	J0510+1800	
	AS 209	2018 Dec 25	45	35	15–500	0 <sup>''</sup> 57	6 <sup>''</sup> 7	J1733–1304	J1517–2422
		2019 Aug 21	45	47	41–3396	0 <sup>''</sup> 09	1 <sup>''</sup> 3	J1733–1304	J1517–2422
		2019 Aug 21	45	47	41–3396	0 <sup>''</sup> 09	1 <sup>''</sup> 4	J1733–1304	J1517–2422
HD 163296	2019 Apr 7	43	35	15–500	0 <sup>''</sup> 57	6 <sup>''</sup> 1	J1733–1304	J1924–2914	
	2019 Aug 21	44	47	41–3396	0 <sup>''</sup> 09	1 <sup>''</sup> 4	J1733–1304	J1924–2914	
	2019 Aug 25	45	47	41–3396	0 <sup>''</sup> 09	1 <sup>''</sup> 4	J1755–2232	J1924–2914	
	2019 Aug 26	45	47	41–3638	0 <sup>''</sup> 08	1 <sup>''</sup> 4	J1755–2232	J1924–2914	

## Appendix B Noise and Noise Correction

Table 11 reports the so-called  $J\nu M$  (Jorsater & van Moorsel 1995) corrections ( $\epsilon$ ) of the image residuals and the measured rms per beam and channel of the  $J\nu M$ -corrected image cubes for each source and targeted molecular line. The  $J\nu M$  correction is equal to the ratio of the CLEAN beam and

dirty beam effective areas, and it is needed because the dirty beam was highly non-Gaussian when combining the short- and long-baseline configurations. See Czekala et al. (2021) for details of how  $\epsilon$  was derived. In cases where the hyperfine components were observed in the same SPW, we only report a single rms and  $\epsilon$  since neither should vary substantially across these narrow SPWs.



**Table 11**  
MAPS Sample rms and  $JvM \epsilon$

Setup	Molecule	Line(s)	IM Lup		GM Aur		AS 209		HD 163296		MWC 480		
			rms (mJy beam <sup>-1</sup> )	$\epsilon$	rms (mJy beam <sup>-1</sup> )	$\epsilon$	rms (mJy beam <sup>-1</sup> )	$\epsilon$	rms (mJy beam <sup>-1</sup> )	$\epsilon$	rms (mJy beam <sup>-1</sup> )	$\epsilon$	
B3-1	HC <sup>15</sup> N	$J = 1-0$	0.815	0.738	1.718	1.005	0.986	0.909	0.851	0.950	1.732	1.008	
	H <sup>13</sup> CN <sup>a</sup>	$J = 1-0$	0.769	0.734	1.631 <sup>a</sup>	1.004	0.915	0.901	0.798	0.947	1.848 <sup>b</sup>	1.000	
	H <sup>13</sup> CO <sup>+</sup>	$J = 1-0$	0.775	0.729	1.685	1.021	0.953	0.903	0.813	0.932	1.816	1.000	
	C <sub>2</sub> H	$N = 1-0,$ $J = \frac{3}{2}-\frac{1}{2}, F = 2-1$	0.746	0.725	1.522 <sup>c</sup>	1.017	0.904	0.893	0.795	0.944	1.700 <sup>d</sup>	0.990	
		$N = 1-0,$ $J = \frac{3}{2}-\frac{1}{2}, F = 1-0$	0.737	0.721	1.502 <sup>c</sup>	1.016	0.908	0.893	0.799	0.945	1.719 <sup>b</sup>	0.996	
		$F = 2-1, F = 0-1$	0.872	0.722	2.052 <sup>d</sup>	1.000	0.919	0.842	0.888	0.934	1.944 <sup>d</sup>	0.992	
	HCN <sup>a</sup>	$J = 1-0, F = 1-1;$ $F = 2-1, F = 0-1$	0.859	0.723	2.051	1.019	0.880	0.810	0.870	0.925	1.907	0.979	
	HCO <sup>+</sup>	$J = 1-0$	0.698	0.650	1.765	1.062	0.662	0.678	0.643	0.732	1.742	1.052	
	HC <sub>3</sub> N	$J = 11-10$	0.549	0.526	1.590	1.006	0.696	0.689	0.668	0.732	1.580	0.990	
H <sub>2</sub> CO	$(J_{K_a, K_c}) = 6_{15}-6_{16}$												
B3-2	CS	$J = 2-1$	0.640	0.639	1.258	1.036	0.646	0.671	0.546	0.582	1.266	1.039	
	C <sup>18</sup> O	$J = 1-0$	0.565	0.561	1.146	0.922	0.670	0.642	0.469	0.505	1.129	0.920	
	<sup>13</sup> CO	$J = 1-0$	0.552	0.560	1.115	0.927	0.471	0.511	0.457	0.502	1.113	0.926	
	CH <sub>3</sub> CN	$J = 6-5, K = 0-2$	0.538	0.560	1.081	0.922	0.457	0.510	0.438	0.509	1.086	0.929	
		$J = 6-5, K = 3$	0.553	0.560	1.091	0.921	0.460	0.510	0.441	0.509	1.094	0.928	
		$J = 6-5, K = 4$	0.543	0.560	1.076	0.920	0.458	0.510	0.443	0.510	1.081	0.925	
		$J = 6-5, K = 5$	0.541	0.560	1.078	0.922	0.457	0.510	0.438	0.509	1.081	0.924	
	C <sup>17</sup> O	$J = 1-0, F = \frac{3}{2}-\frac{5}{2};$ $F = \frac{7}{2}-\frac{5}{2}; F = \frac{5}{2}-\frac{5}{2}$	0.683	0.563	1.363	0.896	0.613	0.539	0.561	0.508	1.404	0.917	
		CN	$N = 1-0, J = \frac{3}{2}-\frac{1}{2},$ $F = \frac{3}{2}-\frac{1}{2}, F = \frac{5}{2}-\frac{3}{2}$	0.827	0.573	1.251	0.751	0.733	0.538	0.647	0.488	1.227 <sup>d</sup>	0.741
	$N = 1-0,$ $J = \frac{3}{2}-\frac{1}{2}, F = \frac{1}{2}-\frac{1}{2}$		0.806	0.573	1.233	0.752	0.688	0.513	0.640	0.489	1.215 <sup>d</sup>	0.741	
	$N = 1-0,$ $J = \frac{3}{2}-\frac{1}{2}, F = \frac{3}{2}-\frac{3}{2}$		0.831	0.575	1.260	0.752	0.700	0.513	0.676	0.514	1.233 <sup>d</sup>	0.741	
	B6-1	DCN <sup>a</sup>	$J = 3-2$	0.886	0.621	1.064	0.872	0.391	0.360	0.511	0.459	1.081	0.856
		<sup>13</sup> CN <sup>b</sup>	$N = 2-1, J = \frac{3}{2}-\frac{1}{2}$	0.876	0.619	1.063	0.874	0.437	0.448	0.508	0.459	1.074	0.854
		H <sub>2</sub> CO	$(J_{K_a, K_c}) = 3_{03}-2_{02}$	0.816	0.627	0.952	0.863	0.344	0.346	0.458	0.455	0.989	0.865
C <sup>18</sup> O		$J = 2-1$	0.732	0.600	0.878	0.809	0.339	0.347	0.415	0.436	0.914	0.823	
<sup>13</sup> CO		$J = 2-1$	0.977	0.575	1.210	0.804	0.471	0.347	0.581	0.436	1.261	0.819	
CH <sub>3</sub> CN		$J = 12-11, K = 0-2$	1.052	0.626	1.259	0.866	0.522	0.446	0.603	0.460	1.311	0.877	
		$J = 12-11, K = 3$	1.057	0.625	1.276	0.876	0.529	0.444	0.578	0.435	1.349	0.901	
CO		$J = 2-1$	1.051	0.594	1.318	0.800	0.562	0.363	0.639	0.445	1.305	0.798	
N <sub>2</sub> D <sup>+</sup> <sup>a</sup>		$J = 3-2$	1.265	0.605	1.225	0.738	0.576	0.343	0.665	0.436	1.210	0.729	
B6-2		<i>c</i> -C <sub>3</sub> H <sub>2</sub>	$(J_{K_a, K_c}) = 7_{07}-6_{16}$	0.303	0.269	0.649	0.559	0.390	0.296	0.376	0.339	0.893	0.697
	$(J_{K_+, K_-}) 6_{15}-5_{24}$		0.308	0.268	0.655	0.560	0.397	0.295	0.383	0.340	0.909	0.697	
	$(J_{K_+, K_-}) 6_{25}-5_{14}$		0.308	0.268	0.659	0.560	0.396	0.294	0.385	0.340	0.908	0.696	
	C <sub>2</sub> H	$N = 3-2, J = \frac{5}{2}-\frac{3}{2},$ $F = 3-2; F = 2-1; F = 2-2$	0.398	0.247	0.951	0.556	0.523	0.278	0.503	0.332	0.924	0.545	
		$N = 3-2, J = \frac{7}{2}-\frac{5}{2},$ $F = 4-3; F = 3-2$	0.407	0.247	0.974	0.556	0.534	0.278	0.509	0.331	0.946	0.545	
		HC <sub>3</sub> N	$J = 29-28$	0.291	0.241	0.740	0.557	0.399	0.277	0.326	0.282	0.747	0.552
	HCN <sup>a</sup>	$J = 3-2, F = 3-2;$ $F = 3-3; F = 2-2$	0.342	0.248	0.797	0.573	0.461	0.281	0.398	0.303	0.757	0.535	

**Notes.** Beams are  $0''.3 \times 0''.3$  for Band 3 and  $0''.15 \times 0''.15$  for Band 6 observations, except those noted, which have beams of  ${}^a 0''.33 \times 0''.33, {}^b 0''.315 \times 0''.314, {}^c 0''.33 \times 0''.326, {}^d 0''.315 \times 0''.315,$  and  ${}^e 0''.33 \times 0''.315$ .

<sup>a</sup> See Cataldi et al. (2021) for the full list of hyperfine components.

<sup>b</sup> See Table 3 for a full list of observed <sup>13</sup>CN hyperfine components.

### Appendix C Disk-integrated Line Fluxes

Table 12 reports the disk-integrated line fluxes or  $3\sigma$  upper limits, as well as the peak S/N. The integrated fluxes were generated from the  $0''.3$  image cubes using the relevant CLEAN masks for each disk. For weaker lines, we only used the CLEAN mask channels where C<sup>18</sup>O showed strong emission,  $>5\sigma$ .

In the case of hyperfine components, the S/N and fluxes are reported for each component if they are readily separable toward all disks. In most cases, there is some line overlap in at least one disk, however, and in these cases, the integrated flux includes all listed hyperfine components, and the peak S/N refers to the strongest line component in the cube. The listed uncertainties do not take into account calibration uncertainties of  $\sim 10\%$ .

**Table 12**  
Approximate Disk-integrated Line Fluxes and Upper Limits Extracted Using an Automated Procedure (See Text)

Setup	Molecule	Line(s)	IM Lup		GM Aur		AS 209		HD 163296		MWC 480	
			Peak (S/N)	Flux (Jy km s <sup>-1</sup> )	Peak (S/N)	Flux (Jy km s <sup>-1</sup> )	Peak (S/N)	Flux (Jy km s <sup>-1</sup> )	Peak (S/N)	Flux (Jy km s <sup>-1</sup> )	Peak (S/N)	Flux (Jy km s <sup>-1</sup> )
B3-1	HC <sup>15</sup> N	$J = 1-0$	4.7	<0.029	3.8	<0.022	4.9	<0.016	4.3	<0.031	3.8	<0.022
	H <sup>13</sup> CN	$J = 1-0$	4.4	<0.045	5.4	<0.035	3.8	<0.025	4.7	<0.048	5.7	<0.035
	H <sup>13</sup> CO <sup>+</sup>	$J = 1-0$	4.8	<0.027 <sup>a</sup>	4.7	0.026 ± 0.011	5.2	0.020 ± 0.008	3.7	<0.030 <sup>a</sup>	3.9	<0.022 <sup>a</sup>
	C <sub>2</sub> H	$N = 1-0, J = \frac{3}{2}-\frac{1}{2}, F = 2-1$	3.8	0.051 ± 0.013	5.7	0.047 ± 0.021 <sup>b</sup>	17.2	0.070 ± 0.008	11.4	0.107 ± 0.015	13.9	0.051 ± 0.010
		$N = 1-0, J = \frac{3}{2}-\frac{1}{2}, F = 1-0$	3.7	<0.027 <sup>a</sup>	3.9	<0.021 <sup>a</sup>	11.5	0.050 ± 0.008	6.6	0.062 ± 0.015	9.1	<0.021 <sup>a</sup>
	HCN	$J = 1-0, F = 1-1; F = 2-1, F = 0-1$	8.4	0.349 ± 0.027	7.0	0.207 ± 0.021	18.3	0.242 ± 0.015	18.2	0.713 ± 0.027	16.9	0.247 ± 0.022
	HCO <sup>+</sup>	$J = 1-0$	33.4	0.595 ± 0.016	27.0	0.580 ± 0.012	30.1	0.198 ± 0.009	33.4	1.092 ± 0.016	26.5	0.452 ± 0.013
	HC <sub>3</sub> N	$J = 11-10$	3.8	<0.035	7.8	0.047 ± 0.013	18.8	0.123 ± 0.010	18.4	0.144 ± 0.019	16.6	0.083 ± 0.013
	H <sub>2</sub> CO	$(J_{Ka,Kc}) = 6_{15}-5_{16}$	3.7	<0.038	3.8	<0.028	3.3	<0.021	3.9	<0.041	3.4	<0.028
B3-2	CS	$J = 2-1$	12.2	0.341 ± 0.016	20.9	0.271 ± 0.011	24.6	0.165 ± 0.009	20.5	0.307 ± 0.017	10.7	0.056 ± 0.011
	C <sup>18</sup> O	$J = 1-0$	9.6	0.161 ± 0.019	18.6	0.149 ± 0.013	5.8	0.073 ± 0.010	41.5	0.976 ± 0.020	36.2	0.410 ± 0.013
	<sup>13</sup> CO	$J = 1-0$	41.7	1.337 ± 0.018	48.3	0.836 ± 0.013	30.2	0.376 ± 0.010	78.1	3.573 ± 0.020	73.3	1.522 ± 0.013
	CH <sub>3</sub> CN	$J = 6-5, K = 0-2$	3.8	<0.063	3.8	<0.043 <sup>a</sup>	4.4	<0.032 <sup>a</sup>	6.0	<0.063 <sup>a</sup>	4.7	<0.044 <sup>a</sup>
		$J = 6-5, K = 3$	3.7	<0.037	3.9	<0.025	3.4	<0.019	4.9	<0.037	4.0	<0.026
		$J = 6-5, K = 4$	5.0	<0.036	3.8	<0.025	4.3	<0.019	3.9	<0.038	3.4	<0.026
		$J = 6-5, K = 5$	3.7	<0.036	3.7	<0.025	3.8	<0.019	3.5	<0.037	3.7	<0.026
	C <sup>17</sup> O	$J = 1-0, F = \frac{3}{2}-\frac{5}{2}; F = \frac{7}{2}-\frac{5}{2}; F = \frac{5}{2}-\frac{3}{2}; F = \frac{5}{2}-\frac{1}{2}$	5.1	<0.071 <sup>a</sup>	7.6	0.083 ± 0.024	4.6	<0.037 <sup>a</sup>	27.2	0.675 ± 0.036	20.7	0.296 ± 0.025
	CN	$N = 1-0, J = \frac{3}{2}-\frac{1}{2}, F = \frac{3}{2}-\frac{1}{2}; F = \frac{3}{2}-\frac{1}{2}$	8.8	0.581 ± 0.038	5.5	0.215 ± 0.029	19.3	0.406 ± 0.022	15.1	1.585 ± 0.043	21.0	0.479 ± 0.029
		$N = 1-0, J = \frac{3}{2}-\frac{1}{2}, F = \frac{1}{2}-\frac{1}{2}$	6.7	0.097 ± 0.027	6.0	0.064 ± 0.020	10.8	0.102 ± 0.015	7.7	0.343 ± 0.031	9.6	0.114 ± 0.021
		$N = 1-0, J = \frac{3}{2}-\frac{1}{2}, F = \frac{3}{2}-\frac{1}{2}$	5.0	0.106 ± 0.027	3.5	<0.041	10.7	0.131 ± 0.016	6.5	0.318 ± 0.031	8.2	0.121 ± 0.021
B6-1	DCN	$J = 3-2$	5.2	0.446 ± 0.125 <sup>b</sup>	5.2	0.279 ± 0.075 <sup>b</sup>	21.8	0.278 ± 0.030	7.6	0.751 ± 0.131 <sup>b</sup>	10.1	0.436 ± 0.090 <sup>b</sup>
	<sup>13</sup> CN	$N = 2-1, J = \frac{3}{2}-\frac{1}{2}$	4.8	<0.271	4.5	<0.151	4.9	<0.128	9.2	<0.227	5.2	<0.151
	H <sub>2</sub> CO	$(J_{Ka,Kc}) = 3_{03}-2_{02}$	14.4	0.852 ± 0.061	29.9	0.913 ± 0.039	16.0	0.299 ± 0.027	11.2	0.902 ± 0.062	6.2	0.151 ± 0.041
	C <sup>18</sup> O	$J = 2-1$	32.8	1.592 ± 0.060	52.0	1.092 ± 0.039	34.0	0.538 ± 0.027	85.8	5.783 ± 0.051	87.0	3.017 ± 0.041
	<sup>13</sup> CO	$J = 2-1$	54.3	8.370 ± 0.083	73.4	5.028 ± 0.048	58.6	2.269 ± 0.038	84.9	15.885 ± 0.080	103.7	8.361 ± 0.057
	CH <sub>3</sub> CN	$J = 12-11, K = 0-2$	5.1	<0.279 <sup>a</sup>	5.4	<0.177 <sup>a</sup>	5.3	<0.136 <sup>a</sup>	5.8	<0.271 <sup>a</sup>	5.2	<0.189 <sup>a</sup>
		$J = 12-11, K = 3$	4.9	<0.164	5.3	<0.105 <sup>a</sup>	5.0	<0.081	4.2	<0.162 <sup>a</sup>	4.9	0.234 ± 0.109 <sup>b</sup>
	CO	$J = 2-1$	89.7	22.342 ± 0.094	99.9	19.844 ± 0.074	118.4	7.790 ± 0.045	142.5	45.246 ± 0.102	217.6	23.226 ± 0.063
N <sub>2</sub> D <sup>+</sup>	$J = 3-2$	4.6	0.559 ± 0.187 <sup>b</sup>	3.9	<0.137 <sup>a</sup>	5.3	0.450 ± 0.083 <sup>b</sup>	5.9	0.637 ± 0.173 <sup>b</sup>	4.4	<0.138 <sup>a</sup>	
B6-2	<i>c</i> -C <sub>3</sub> H <sub>2</sub>	$(J_{Ka,Kc}) = 7_{07}-6_{16}$	5.5	<0.076 <sup>a</sup>	5.5	<0.110 <sup>a</sup>	27.1	0.268 ± 0.032	15.7	0.227 ± 0.054	15.1	0.489 ± 0.110 <sup>b</sup>
		$(J_{Ka,Kc}) = 6_{15}-5_{24}$	6.2	<0.077	4.0	<0.111 <sup>a</sup>	6.9	0.267 ± 0.058 <sup>b</sup>	6.1	0.250 ± 0.093 <sup>b</sup>	5.3	<0.115
		$(J_{Ka,Kc}) = 6_{25}-5_{14}$	5.1	<0.077	4.8	<0.112 <sup>a</sup>	15.1	0.162 ± 0.032	8.7	0.745 ± 0.106 <sup>b</sup>	10.0	0.464 ± 0.113 <sup>b</sup>
	C <sub>2</sub> H	$N = 3-2, J = \frac{5}{2}-\frac{3}{2}, F = 3-2; F = 2-1; F = 2-2$	9.5	0.473 ± 0.088	8.9	0.409 ± 0.133	55.8	1.904 ± 0.075	48.6	2.852 ± 0.125	39.3	1.210 ± 0.133
		$N = 3-2, J = \frac{7}{2}-\frac{5}{2}, F = 4-3; F = 3-2$	14.0	0.717 ± 0.072	12.9	0.573 ± 0.110	60.6	2.166 ± 0.060	57.8	3.467 ± 0.100	42.7	1.478 ± 0.110
	HC <sub>3</sub> N	$J = 29-28$	4.4	<0.077	8.4	0.395 ± 0.121 <sup>b</sup>	6.6	0.256 ± 0.060 <sup>b</sup>	24.6	0.173 ± 0.052	9.8	0.129 ± 0.064
	HCN	$J = 3-2, F = 3-2; F = 3-3; F = 2-2$	49.8	2.443 ± 0.073	48.6	1.835 ± 0.107	85.0	3.010 ± 0.061	124.5	7.472 ± 0.098	68.8	2.561 ± 0.110

**Notes.**

<sup>a</sup> These lines are detected when the flux extraction is optimized. See Zhang et al. (2021), Guzmán et al. (2021), Ilee et al. (2021), Cataldi et al. (2021), Bergner et al. (2021), Le Gal et al. (2021), and Aikawa et al. (2021) for the precise line fluxes.

<sup>b</sup> Only channels with at least 5 $\sigma$  flux in C<sup>18</sup>O were included to calculate these fluxes to reduce noise.

Note that because these line fluxes were generated using an automated pipeline, they should be viewed as approximations. The same pipeline also generates very conservative noise estimates compared to a detailed analysis. As a result, several lines that are reported as upper limits here are revealed to be low-S/N detections upon closer inspection and/or using tools such as matched filter analysis (Loomis et al. 2018b). For precise line fluxes, upper limits, and radial profiles, the reader is advised to consult Zhang et al. (2021) for CO isotopologues; Guzmán et al. (2021) for HCN, C<sub>2</sub>H, and H<sub>2</sub>CO lines; Cataldi et al. (2021) for DCN and N<sub>2</sub>D<sup>+</sup>; Ilee et al. (2021) for HC<sub>3</sub>N, CH<sub>3</sub>N, and *c*-C<sub>3</sub>H<sub>2</sub>; Bergner et al. (2021) for CN; Le Gal et al. (2021) for CS (as well as upper limits on other S-bearing molecules); and Aikawa et al. (2021) for HCO<sup>+</sup> and H<sup>13</sup>CO<sup>+</sup>.

### ORCID iDs

Karin I. Öberg  <https://orcid.org/0000-0001-8798-1347>  
 Viviana V. Guzmán  <https://orcid.org/0000-0003-4784-3040>  
 Catherine Walsh  <https://orcid.org/0000-0001-6078-786X>  
 Yuri Aikawa  <https://orcid.org/0000-0003-3283-6884>  
 Edwin A. Bergin  <https://orcid.org/0000-0003-4179-6394>  
 Charles J. Law  <https://orcid.org/0000-0003-1413-1776>  
 Ryan A. Loomis  <https://orcid.org/0000-0002-8932-1219>  
 Felipe Alarcón  <https://orcid.org/0000-0002-2692-7862>  
 Sean M. Andrews  <https://orcid.org/0000-0003-2253-2270>  
 Jaehan Bae  <https://orcid.org/0000-0001-7258-770X>  
 Jennifer B. Bergner  <https://orcid.org/0000-0002-8716-0482>  
 Yann Boehler  <https://orcid.org/0000-0002-8692-8744>  
 Alice S. Booth  <https://orcid.org/0000-0003-2014-2121>  
 Arthur D. Bosman  <https://orcid.org/0000-0003-4001-3589>  
 Jenny K. Calahan  <https://orcid.org/0000-0002-0150-0125>  
 Gianni Cataldi  <https://orcid.org/0000-0002-2700-9676>  
 L. Ilesdore Cleeves  <https://orcid.org/0000-0003-2076-8001>  
 Ian Czekala  <https://orcid.org/0000-0002-1483-8811>  
 Kenji Furuya  <https://orcid.org/0000-0002-2026-8157>  
 Jane Huang  <https://orcid.org/0000-0001-6947-6072>  
 John D. Ilee  <https://orcid.org/0000-0003-1008-1142>  
 Nicolas T. Kurtovic  <https://orcid.org/0000-0002-2358-4796>  
 Romane Le Gal  <https://orcid.org/0000-0003-1837-3772>  
 Yao Liu  <https://orcid.org/0000-0002-7616-666X>  
 Feng Long  <https://orcid.org/0000-0002-7607-719X>  
 François Ménard  <https://orcid.org/0000-0002-1637-7393>  
 Hideko Nomura  <https://orcid.org/0000-0002-7058-7682>  
 Laura M. Pérez  <https://orcid.org/0000-0002-1199-9564>  
 Chunhua Qi  <https://orcid.org/0000-0001-8642-1786>  
 Kamber R. Schwarz  <https://orcid.org/0000-0002-6429-9457>  
 Anibal Sierra  <https://orcid.org/0000-0002-5991-8073>  
 Richard Teague  <https://orcid.org/0000-0003-1534-5186>  
 Takashi Tsukagoshi  <https://orcid.org/0000-0002-6034-2892>  
 Yoshihide Yamato  <https://orcid.org/0000-0003-4099-6941>  
 Merel L. R. van 't Hoff  <https://orcid.org/0000-0002-2555-9869>  
 Abygail R. Waggoner  <https://orcid.org/0000-0002-1566-389X>  
 David J. Wilner  <https://orcid.org/0000-0003-1526-7587>  
 Ke Zhang  <https://orcid.org/0000-0002-0661-7517>

### References

Agúndez, M., Roueff, E., Le Petit, F., & Le Boulart, J. 2018, *A&A*, 616, A19  
 Aikawa, Y., Cataldi, G., Yamato, Y., et al. 2021, *ApJS*, 257, 13  
 Aikawa, Y., Furuya, K., Hincelin, U., & Herbst, E. 2018, *ApJ*, 855, 119  
 Aikawa, Y., & Herbst, E. 1999, *A&A*, 351, 233  
 Aikawa, Y., & Herbst, E. 2001, *A&A*, 371, 1107

Aikawa, Y., van Zadelhoff, G. J., van Dishoeck, E. F., & Herbst, E. 2002, *A&A*, 386, 622  
 Akimkin, V., Zhukovska, S., Wiebe, D., et al. 2013, Protostars and Planets VI Conf., 2S029  
 Alarcón, F., Bosman, A. D., Bergin, E. A., et al. 2021, *ApJ*, 257, 8  
 Alarcón, F., Teague, R., Zhang, K., Bergin, E. A., & Barraza-Alfaro, M. 2020, *ApJ*, 905, 68  
 Alcalá, J. M., Manara, C. F., Natta, A., et al. 2017, *A&A*, 600, A20  
 ALMA Partnership, Brogan, C. L., Pérez, L. M., et al. 2015, *ApJL*, 808, L3  
 Altwegg, K., Balsiger, H., & Fuselier, S. A. 2019, *ARA&A*, 57, 113  
 Alves, F. O., Cleeves, L. I., Girart, J. M., et al. 2020, *ApJL*, 904, L6  
 Andrews, S. M. 2020, *ARA&A*, 58, 483  
 Andrews, S. M., Huang, J., Pérez, L. M., et al. 2018, *ApJL*, 869, L41  
 Andrews, S. M., Wilner, D. J., Hughes, A. M., Qi, C., & Dullemond, C. P. 2009, *ApJ*, 700, 1502  
 Andrews, S. M., Wilner, D. J., Zhu, Z., et al. 2016, *ApJL*, 820, L40  
 Antonellini, S., Kamp, I., Lahuis, F., et al. 2016, *A&A*, 585, A61  
 Astropy Collaboration, Price-Whelan, A. M., Sipőcz, B. M., et al. 2018, *AJ*, 156, 123  
 Avenhaus, H., Quanz, S. P., Garufi, A., et al. 2018, *ApJ*, 863, 44  
 Banzatti, A., Pontoppidan, K. M., Salyk, C., et al. 2017, *ApJ*, 834, 152  
 Baruteau, C., Bai, X., Mordasini, C., & Mollière, P. 2016, *SSRv*, 205, 77  
 Beck, T. L., & Bary, J. S. 2019, *ApJ*, 884, 159  
 Bergin, E., Calvet, N., D'Alessio, P., & Herczeg, G. J. 2003, *ApJL*, 591, L159  
 Bergin, E. A., Cleeves, L. I., Gorti, U., et al. 2013, *Natur*, 493, 644  
 Bergin, E. A., Du, F., Cleeves, L. I., et al. 2016, *ApJ*, 831, 101  
 Bergin, E. A., & Williams, J. P. 2017, in Formation, Evolution, and Dynamics of Young Solar Systems, ed. M. Pessah & O. Gressel (Berlin: Springer), 1  
 Bergner, J. B., Guzmán, V. G., Öberg, K. I., Loomis, R. A., & Pegues, J. 2018, *ApJ*, 857, 69  
 Bergner, J. B., Öberg, K. I., Bergin, E. A., et al. 2019, *ApJ*, 876, 25  
 Bergner, J. B., Öberg, K. I., Guzmán, V. V., et al. 2021, *ApJS*, 257, 11  
 Bertin, M., Doronin, M., Fillion, J. H., et al. 2017, *A&A*, 598, A18  
 Birstiel, T., Andrews, S. M., & Ercolano, B. 2012, *A&A*, 544, A79  
 Birstiel, T., Ricci, L., Trotta, F., et al. 2010, *A&A*, 516, L14  
 Booth, A. S., Tabone, B., Ilee, J. D., et al. 2021, *ApJS*, 257, 16  
 Booth, A. S., Walsh, C., Ilee, J. D., et al. 2019, *ApJL*, 882, L31  
 Bosman, A. D., Alarcón, F., Bergin, E. A., et al. 2021a, *ApJS*, 257, 7  
 Bosman, A. D., Bergin, E. A., Loomis, R. A., et al. 2021b, *ApJS*, 257, 15  
 Bosman, A. D., Walsh, C., & van Dishoeck, E. F. 2018, *A&A*, 618, A182  
 Calahan, J., Bergin, E. A., Zhang, K., et al. 2021, *ApJS*, 257, 17  
 Calahan, J. K., Bergin, E., Zhang, K., et al. 2021, *ApJ*, 908, 8  
 Calvet, N., D'Alessio, P., Watson, D. M., et al. 2005, *ApJL*, 630, L185  
 Carney, M. T., Fedele, D., Hogerheijde, M. R., et al. 2018, *A&A*, 614, A106  
 Carney, M. T., Hogerheijde, M. R., Guzmán, V. V., et al. 2019, *A&A*, 623, A124  
 Cataldi, G., Yamato, Y., Aikawa, Y., et al. 2021, *ApJS*, 257, 10  
 Cazzoletti, P., van Dishoeck, E. F., Visser, R., Facchini, S., & Bruderer, S. 2018, *A&A*, 609, A93  
 Ceccarelli, C., Caselli, P., Bockelée-Morvan, D., et al. 2014, in Protostars and Planets VI, ed. H. Beuther et al. (Tucson, AZ: Univ. Arizona Press), 859  
 Ciesla, F. J., & Cuzzi, J. N. 2006, *Icar*, 181, 178  
 Cieza, L. A., González-Ruilova, C., Hales, A. S., et al. 2021, *MNRAS*, 501, 2934  
 Cleeves, L. I., Bergin, E. A., & Adams, F. C. 2014a, *ApJ*, 794, 123  
 Cleeves, L. I., Bergin, E. A., Alexander, C. M. O., et al. 2014b, *Sci*, 345, 1590  
 Cleeves, L. I., Bergin, E. A., & Harries, T. J. 2015, *ApJ*, 807, 2  
 Cleeves, L. I., Bergin, E. A., O'D. Alexander, C. M., et al. 2016a, *ApJ*, 819, 13  
 Cleeves, L. I., Öberg, K. I., Wilner, D. J., et al. 2016b, *ApJ*, 832, 110  
 Cleeves, L. I., Öberg, K. I., Wilner, D. J., et al. 2018, *ApJ*, 865, 155  
 Cridland, A. J., van Dishoeck, E. F., Alessi, M., & Pudritz, R. E. 2020, *A&A*, 642, A229  
 Czekala, I., Loomis, R. A., Teague, R., et al. 2021, *ApJS*, 257, 2  
 D'Alessio, P., Calvet, N., Hartmann, L., Franco-Hernández, R., & Servín, H. 2006, *ApJ*, 638, 314  
 D'Alessio, P., Calvet, N., Hartmann, L., Lizano, S., & Cantó, J. 1999, *ApJ*, 527, 893  
 Dartois, E., Dutrey, A., & Guilloteau, S. 2003, *A&A*, 399, 773  
 de Gregorio-Monsalvo, I., Ménard, F., Dent, W., et al. 2013, *A&A*, 557, A133  
 Disk Dynamics Collaboration, Armitage, P. J., Bae, J., et al. 2020, arXiv:2009.04345  
 Dodson-Robinson, S. E., Evans, N. J., II, Ramos, A., Yu, M., & Willacy, K. 2018, *ApJL*, 868, L37  
 Dominik, C., & Tielens, A. G. G. M. 1997, *ApJ*, 480, 647  
 Dong, R., Liu, S.-Y., & Fung, J. 2019, *ApJ*, 870, 72

- Drabek-Maunder, E., Mohanty, S., Greaves, J., et al. 2016, *ApJ*, **833**, 260
- Drozhdovskaya, M. N., van Dishoeck, E. F., Rubin, M., Jørgensen, J. K., & Altwegg, K. 2019, *MNRAS*, **490**, 50
- Du, F., Bergin, E. A., Hogerheijde, M., et al. 2017, *ApJ*, **842**, 98
- Du, F., Bergin, E. A., & Hogerheijde, M. R. 2015, *ApJL*, **807**, L32
- Dutrey, A., Guilloteau, S., & Guelin, M. 1997, *A&A*, **317**, L55
- Dutrey, A., Guilloteau, S., Piétu, V., et al. 2008, *A&A*, **490**, L15
- Dutrey, A., Guilloteau, S., Piétu, V., et al. 2017, *A&A*, **607**, A130
- Dutrey, A., Henning, T., Guilloteau, S., et al. 2007, *A&A*, **464**, 615
- Dutrey, A., Semenov, D., Chapillon, E., et al. 2014, in *Protostars and Planets VI*, ed. H. Beuther et al. (Tucson, AZ: Univ. Arizona Press), 317
- Dutrey, A., Wakelam, V., Boehler, Y., et al. 2011, *A&A*, **535**, A104
- Ellerbroek, L. E., Podio, L., Dougados, C., et al. 2014, *A&A*, **563**, A87
- Endres, C. P., Schlemmer, S., Schilke, P., Stutzki, J., & Müller, H. S. P. 2016, *JMoSp*, **327**, 95
- Españillat, C., D'Alessio, P., Hernández, J., et al. 2010, *ApJ*, **717**, 441
- Facchini, S., Pinilla, P., van Dishoeck, E. F., & de Juan Ovelar, M. 2018, *A&A*, **612**, A104
- Facchini, S., Teague, R., Bae, J., et al. 2021, *AJ*, **162**, 99
- Fairlamb, J. R., Oudmaijer, R. D., Mendigutía, I., Ilee, J. D., & van den Ancker, M. E. 2015, *MNRAS*, **453**, 976
- Favre, C., Cleeves, L. I., Bergin, E. A., Qi, C., & Blake, G. A. 2013, *ApJL*, **776**, L38
- Favre, C., Fedele, D., Maud, L., et al. 2019, *ApJ*, **871**, 107
- Fedele, D., Bruderer, S., van Dishoeck, E. F., et al. 2012, *A&A*, **544**, L9
- Fedele, D., Carney, M., Hogerheijde, M. R., et al. 2017, *A&A*, **600**, A72
- Fedele, D., Tazzari, M., Booth, R., et al. 2018, *A&A*, **610**, A24
- Flaherty, K. M., Hughes, A. M., Rose, S. C., et al. 2017, *ApJ*, **843**, 150
- Flaherty, K. M., Hughes, A. M., Rosenfeld, K. A., et al. 2015, *ApJ*, **813**, 99
- Flock, M., Ruge, J. P., Dzyurkevich, N., et al. 2015, *A&A*, **574**, A68
- Fogel, J. K. J., Bethell, T. J., Bergin, E. A., Calvet, N., & Semenov, D. 2011, *ApJ*, **726**, 29
- Gaia Collaboration, Brown, A. G. A., Vallenari, A., et al. 2018, *A&A*, **616**, A1
- Glassgold, A. E., Najita, J., & Igea, J. 1997, *ApJ*, **480**, 344
- Gundlach, B., & Blum, J. 2015, *ApJ*, **798**, 34
- Günther, H. M., Schmitt, J. H. M. M., Robrade, J., & Liefke, C. 2007, *A&A*, **466**, 1111
- Güttler, C., Blum, J., Zsom, A., Ormel, C. W., & Dullemond, C. P. 2010, *A&A*, **513**, A56
- Guzmán, V. V., Bergner, J. B., Law, C. J., et al. 2021, *ApJS*, **257**, 6
- Guzmán, V. V., Huang, J., Andrews, S. M., et al. 2018, *ApJL*, **869**, L48
- Guzmán, V. V., Öberg, K. I., Loomis, R., & Qi, C. 2015, *ApJ*, **814**, 53
- Hartmann, L. 2000, *SSRv*, **92**, 55
- Hartmann, L., Herczeg, G., & Calvet, N. 2016, *ARA&A*, **54**, 135
- Hayashi, C. 1981, *PThPS*, **70**, 35
- Helling, C., Woitke, P., Rimmer, P. B., et al. 2014, *Life*, **4**, 142
- Hendler, N., Pascucci, I., Pinilla, P., et al. 2020, *ApJ*, **895**, 126
- Henning, T., & Semenov, D. 2013, *ChRv*, **113**, 9016
- Henning, T., Semenov, D., Guilloteau, S., et al. 2010, *ApJ*, **714**, 1511
- Howard, C. D., Sandell, G., Vacca, W. D., et al. 2013, *ApJ*, **776**, 21
- Huang, J., Bergin, E. A., Öberg, K. I., et al. 2021, *ApJS*, **257**, 19
- Huang, J., Andrews, S. M., Cleeves, L. I., et al. 2018a, *ApJ*, **852**, 122
- Huang, J., Andrews, S. M., Dullemond, C. P., et al. 2018b, *ApJL*, **869**, L42
- Huang, J., Andrews, S. M., Dullemond, C. P., et al. 2020, *ApJ*, **891**, 48
- Huang, J., Andrews, S. M., Pérez, L. M., et al. 2018c, *ApJL*, **869**, L43
- Huang, J., & Öberg, K. I. 2015, *ApJL*, **809**, L26
- Huang, J., Öberg, K. I., & Andrews, S. M. 2016, *ApJL*, **823**, L18
- Huang, J., Öberg, K. I., Qi, C., et al. 2017, *ApJ*, **835**, 231
- Hughes, A. M., Andrews, S. M., Espaillat, C., et al. 2009, *ApJ*, **698**, 131
- Hughes, A. M., Wilner, D. J., Qi, C., & Hogerheijde, M. R. 2008, *ApJ*, **678**, 1119
- Hunter, J. D. 2007, *CSE*, **9**, 90
- Ilee, J. D., Walsh, C., Booth, A. S., et al. 2021, *ApJS*, **257**, 9
- Ingleby, L., Espaillat, C., Calvet, N., et al. 2015, *ApJ*, **805**, 149
- Isella, A., Guidi, G., Testi, L., et al. 2016, *PhRvL*, **117**, 251101
- Isella, A., Huang, J., Andrews, S. M., et al. 2018, *ApJL*, **869**, L49
- Isella, A., Testi, L., Natta, A., et al. 2007, *A&A*, **469**, 213
- Jang-Condell, H. 2008, *ApJ*, **679**, 797
- Johansen, A., & Lambrechts, M. 2017, *AREPS*, **45**, 359
- Jørgensen, J. K., Visser, R., Sakai, N., et al. 2013, *ApJL*, **779**, L22
- Jorsater, S., & van Moorsel, G. A. 1995, *AJ*, **110**, 2037
- Kama, M., Trapman, L., Fedele, D., et al. 2020, *A&A*, **634**, A88
- Kamp, I., & Dullemond, C. P. 2004, *ApJ*, **615**, 991
- Kamp, I., Tilling, I., Woitke, P., Thi, W. F., & Hogerheijde, M. 2010, *A&A*, **510**, A18
- Kanagawa, K. D., Muto, T., Tanaka, H., et al. 2015, *ApJL*, **806**, L15
- Kastner, J. H., Qi, C., Dickson-Vandervelde, D. A., et al. 2018, *ApJ*, **863**, 106
- Kastner, J. H., Zuckerman, B., Weintraub, D. A., & Forveille, T. 1997, *Sci*, **277**, 67
- Keane, J. T., Pascucci, I., Espaillat, C., et al. 2014, *ApJ*, **787**, 153
- Keppler, M., Benisty, M., Müller, A., et al. 2018, *A&A*, **617**, A44
- Keppler, M., Teague, R., Bae, J., et al. 2019, *A&A*, **625**, A118
- Klaassen, P. D., Juhász, A., Mathews, G. S., et al. 2013, *A&A*, **555**, A73
- Koerner, D. W., Sargent, A. I., & Beckwith, S. V. W. 1993, *Icar*, **106**, 2
- Kraus, A. L., & Hillenbrand, L. A. 2009, *ApJ*, **704**, 531
- Krijt, S., Bosman, A. D., Zhang, K., et al. 2020, *ApJ*, **899**, 134
- Kusakabe, N., Grady, C. A., Sitko, M. L., et al. 2012, *ApJ*, **753**, 153
- Law, C., Loomis, R. A., Teague, R., et al. 2021a, *ApJS*, **257**, 3
- Law, C., Teague, R., Loomis, R. A., et al. 2021b, *ApJS*, **257**, 4
- Le Gal, R., Brady, M. T., Öberg, K. I., Roueff, E., & Petit, F. L. 2019b, *ApJ*, **886**, 86
- Le Gal, R., Öberg, K. I., Loomis, R. A., Pegues, J., & Bergner, J. B. 2019a, *ApJ*, **876**, 72
- Le Gal, R., Öberg, K. I., Teague, R., et al. 2021, *ApJS*, **257**, 12
- Leemker, M., van't Hoff, M. L. R., Trapman, L., et al. 2021, *A&A*, **646**, A3
- Lewis, J. S. 1974, *Sci*, **186**, 440
- Liu, Y., Dipierro, G., Ragusa, E., et al. 2019, *A&A*, **622**, A75
- Lommen, D., Wright, C. M., Maddison, S. T., et al. 2007, *A&A*, **462**, 211
- Long, F., Pinilla, P., Herczeg, G. J., et al. 2018, *ApJ*, **869**, 17
- Loomis, R. A., Cleeves, L. I., Öberg, K. I., et al. 2018a, *ApJ*, **859**, 131
- Loomis, R. A., Öberg, K. I., Andrews, S. M., et al. 2018b, *AJ*, **155**, 182
- Loomis, R. A., Öberg, K. I., Andrews, S. M., et al. 2020, *ApJ*, **893**, 101
- Louvet, F., Dougados, C., Cabrit, S., et al. 2018, *A&A*, **618**, A120
- Lynden-Bell, D., & Pringle, J. E. 1974, *MNRAS*, **168**, 603
- Maccías, E., Espaillat, C. C., Ribas, Á., et al. 2018, *ApJ*, **865**, 37
- Marsh, K. A., & Mahoney, M. J. 1992, *ApJL*, **395**, L115
- Mathews, G. S., Klaassen, P. D., Juhász, A., et al. 2013, *A&A*, **557**, A132
- Mawet, D., Absil, O., Montagnier, G., et al. 2012, *A&A*, **544**, A131
- McClure, M. K., Bergin, E. A., Cleeves, L. I., et al. 2016, *ApJ*, **831**, 167
- McGuire, B. A. 2018, *ApJS*, **239**, 17
- McMullin, J. P., Waters, B., Schiebel, D., Young, W., & Golap, K. 2007, in *ASP Conf. Ser. 376, Astronomical Data Analysis Software and Systems XVI*, ed. R. A. Shaw, F. Hill, & D. J. Bell (San Francisco, CA: ASP), 127
- Meijerink, R., Aresu, G., Kamp, I., et al. 2012, *A&A*, **547**, A68
- Mendigutía, I., Brittain, S., Eiroa, C., et al. 2013, *ApJ*, **776**, 44
- Miotello, A., Facchini, S., van Dishoeck, E. F., et al. 2019, *A&A*, **631**, A69
- Miotello, A., van Dishoeck, E. F., Kama, M., & Bruderer, S. 2016, *A&A*, **594**, A85
- Miotello, A., van Dishoeck, E. F., Williams, J. P., et al. 2017, *A&A*, **599**, A113
- Molyarova, T., Akimkin, V., Semenov, D., et al. 2017, *ApJ*, **849**, 130
- Monnier, J. D., Harries, T. J., Aarnio, A., et al. 2017, *ApJ*, **838**, 20
- Montesinos, B., Eiroa, C., Mora, A., & Merín, B. 2009, *A&A*, **495**, 901
- Morbidelli, A., Szulágyi, J., Crida, A., et al. 2014, *Icar*, **232**, 266
- Mordasini, C., van Boekel, R., Mollière, P., Henning, T., & Benneke, B. 2016, *ApJ*, **832**, 41
- Müller, H. S. P., Schlöder, F., Stutzki, J., & Winnewisser, G. 2005, *JMoSt*, **742**, 215
- Müller, H. S. P., Thorwirth, S., Roth, D. A., & Winnewisser, G. 2001, *A&A*, **370**, L49
- Mumma, M. J., & Charnley, S. B. 2011, *ARA&A*, **49**, 471
- Muro-Arena, G. A., Dominik, C., Waters, L. B. F. M., et al. 2018, *A&A*, **614**, A24
- Nomura, H., Aikawa, Y., Tsujimoto, M., Nakagawa, Y., & Millar, T. J. 2007, *ApJ*, **661**, 334
- Nomura, H., Tsukagoshi, T., Kawabe, R., et al. 2021, *ApJ*, **914**, 113
- Notsu, S., Akiyama, E., Booth, A., et al. 2019, *ApJ*, **875**, 96
- Öberg, K. I., & Bergin, E. A. 2021, *PhR*, **893**, 1
- Öberg, K. I., Cleeves, L. I., Bergner, J. B., et al. 2021, *AJ*, **161**, 38
- Öberg, K. I., Furuya, K., Loomis, R., et al. 2015a, *ApJ*, **810**, 112
- Öberg, K. I., Guzmán, V. V., Furuya, K., et al. 2015b, *Natur*, **520**, 198
- Öberg, K. I., Murray-Clay, R., & Bergin, E. A. 2011a, *ApJL*, **743**, L16
- Öberg, K. I., Qi, C., Fogel, J. K. J., et al. 2010, *ApJ*, **720**, 480
- Öberg, K. I., Qi, C., Fogel, J. K. J., et al. 2011b, *ApJ*, **734**, 98
- Öberg, K. I., Qi, C., Wilner, D. J., & Hogerheijde, M. R. 2012, *ApJ*, **749**, 162
- Padgett, D. L., Cieza, L., Stapelfeldt, K. R., et al. 2006, *ApJ*, **645**, 1283
- Paneque-Carreño, T., Perez, L. M., Benisty, M., et al. 2021, *ApJ*, **914**, 88
- Panić, O., Hogerheijde, M. R., Wilner, D., & Qi, C. 2009, *A&A*, **501**, 269
- Patel, B. H., Percivalle, C., Ritson, D. J., Duffy, C. D., & Sutherland, J. D. 2015, *NatCh*, **7**, 301
- Pearce, B. K. D., Pudritz, R. E., Semenov, D. A., & Henning, T. K. 2017, *PNAS*, **114**, 11327
- Pegues, J., Öberg, K. I., Bergner, J. B., et al. 2020, *ApJ*, **890**, 142

- Pérez, L. M., Carpenter, J. M., Chandler, C. J., et al. 2012, *ApJL*, 760, L17
- Perez, S., Dunhill, A., Casassus, S., et al. 2015, *ApJL*, 811, L5
- Pickett, H. M., Poynter, R. L., Cohen, E. A., et al. 1998, *JQSRT*, 60, 883
- Piétu, V., Dutrey, A., & Guilloteau, S. 2007, *A&A*, 467, 163
- Piétu, V., Dutrey, A., Guilloteau, S., Chapillon, E., & Pety, J. 2006, *A&A*, 460, L43
- Pineda, J. E., Segura-Cox, D., Caselli, P., et al. 2020, *NatAs*, 4, 1158
- Pinilla, P., Pohl, A., Stammer, S. M., & Birnstiel, T. 2017, *ApJ*, 845, 68
- Pinte, C., Ménard, F., Duchêne, G., et al. 2018a, *A&A*, 609, A47
- Pinte, C., Padgett, D. L., Ménard, F., et al. 2008, *A&A*, 489, 633
- Pinte, C., Price, D. J., Ménard, F., et al. 2018b, *ApJL*, 860, L13
- Pinte, C., Price, D. J., Ménard, F., et al. 2020, *ApJL*, 890, L9
- Piso, A.-M. A., Pegues, J., & Öberg, K. I. 2016, *ApJ*, 833, 203
- Podio, L., Garufi, A., Codella, C., et al. 2020, *A&A*, 642, L7
- Pollack, J. B., Hubickyj, O., Bodenheimer, P., et al. 1996, *Icar*, 124, 62
- Pontoppidan, K. M., Salyk, C., Bergin, E. A., et al. 2014, in *Protostars and Planets VI*, ed. H. Beuther et al. (Tucson, AZ: Univ. Arizona Press), 363
- Pontoppidan, K. M., Salyk, C., Blake, G. A., et al. 2010, *ApJ*, 720, 887
- Powell, D., Murray-Clay, R., Pérez, L. M., Schlichting, H. E., & Rosenthal, M. 2019, *ApJ*, 878, 116
- Powner, M. W., Gerland, B., & Sutherland, J. D. 2009, *Natur*, 459, 239
- Price, E. M., Cleaves, L. I., & Öberg, K. I. 2020, *ApJ*, 890, 154
- Qi, C., D'Alessio, P., Öberg, K. I., et al. 2011, *ApJ*, 740, 84
- Qi, C., Öberg, K. I., Andrews, S. M., et al. 2015, *ApJ*, 813, L28
- Qi, C., Öberg, K. I., Espaillat, C. C., et al. 2019, *ApJ*, 882, 160
- Qi, C., Öberg, K. I., Wilner, D. J., et al. 2013, *Sci*, 341, 630
- Qi, C., Wilner, D. J., Aikawa, Y., Blake, G. A., & Hogerheijde, M. R. 2008, *ApJ*, 681, 1396
- Rab, C., Elbakyan, V., Vorobyov, E., et al. 2017, *A&A*, 604, A15
- Rab, C., Güdel, M., Woitke, P., et al. 2018, *A&A*, 609, A91
- Rab, C., Kamp, I., Dominik, C., et al. 2020, *A&A*, 642, A165
- Raymond, S. N., Kokubo, E., Morbidelli, A., Morishima, R., & Walsh, K. J. 2014, in *Protostars and Planets VI*, ed. H. Beuther et al. (Tucson, AZ: Univ. Arizona Press), 595
- Reboussin, L., Wakelam, V., Guilloteau, S., Hersant, F., & Dutrey, A. 2015, *A&A*, 579, A82
- Rich, E. A., Teague, R., Monnier, J. D., et al. 2021, *ApJ*, 913, 138
- Rich, E. A., Wisniewski, J. P., Sitko, M. L., et al. 2020, *ApJ*, 902, 4
- Rivière-Marichalar, P., Fuente, A., Le Gal, R., et al. 2020, *A&A*, 642, A32
- Rodenkirch, P. J., Rometsch, T., Dullemond, C. P., Weber, P., & Kley, W. 2021, *A&A*, 647, A174
- Ros, K., & Johansen, A. 2013, *A&A*, 552, A137
- Rosenfeld, K. A., Andrews, S. M., Wilner, D. J., Kastner, J. H., & McClure, M. K. 2013, *ApJ*, 775, 136
- Rosenfeld, K. A., Qi, C., Andrews, S. M., et al. 2012, *ApJ*, 757, 129
- Rosotti, G. P., Ilee, J. D., Facchini, S., et al. 2021, *MNRAS*, 501, 3427
- Ruud, M., & Gorti, U. 2019, *ApJ*, 885, 146
- Salinas, V. N., Hogerheijde, M. R., Mathews, G. S., et al. 2017, *A&A*, 606, A125
- Salyk, C., Herczeg, G. J., Brown, J. M., et al. 2013, *ApJ*, 769, 21
- Salyk, C., Pontoppidan, K. M., Blake, G. A., Najita, J. R., & Carr, J. S. 2011, *ApJ*, 731, 130
- Schöier, F. L., van der Tak, F. F. S., van Dishoeck, E. F., & Black, J. H. 2005, *A&A*, 432, 369
- Schwarz, K., Calahan, J. K., Zhang, K., et al. 2021, *ApJS*, 257, 20
- Schwarz, K. R., Bergin, E. A., Cleaves, L. I., et al. 2016, *ApJ*, 823, 91
- Schwarz, K. R., Bergin, E. A., Cleaves, L. I., et al. 2018, *ApJ*, 856, 85
- Seifert, R. A., Cleaves, L. I., Adams, F. C., & Li, Z.-Y. 2021, *ApJ*, 912, 136
- Semenov, D., Favre, C., Fedele, D., et al. 2018, *A&A*, 617, A28
- Semenov, D., Pavlyuchenkov, Y., Henning, T., Wolf, S., & Launhardt, R. 2008, *ApJL*, 673, L195
- Semenov, D., & Wiebe, D. 2011, *ApJS*, 196, 25
- Semenov, D., Wiebe, D., & Henning, T. 2006, *ApJL*, 647, L57
- Sierra, A., Pérez, L. M., Zhang, K., et al. 2021, *ApJS*, 257, 14
- Simon, M., Guilloteau, S., Beck, T. L., et al. 2019, *ApJ*, 884, 42
- Stevenson, D. J., & Lunine, J. I. 1988, *Icar*, 75, 146
- Strom, K. M., Strom, S. E., Edwards, S., Cabrit, S., & Skrutskie, M. F. 1989, *AJ*, 97, 1451
- Tazzari, M., Testi, L., Ercolano, B., et al. 2016, *A&A*, 588, A53
- Teague, R. 2019, *JOSS*, 4, 1632
- Teague, R., Bae, J., Aikawa, Y., et al. 2021, *ApJS*, 257, 18
- Teague, R., Bae, J., & Bergin, E. A. 2019a, *Natur*, 574, 378
- Teague, R., Bae, J., Bergin, E. A., Birnstiel, T., & Foreman-Mackey, D. 2018a, *ApJL*, 860, L12
- Teague, R., Bae, J., Birnstiel, T., & Bergin, E. A. 2018b, *ApJ*, 868, 113
- Teague, R., Bae, J., Huang, J., & Bergin, E. A. 2019b, *ApJL*, 884, L56
- Teague, R., & Foreman-Mackey, D. 2018, *Bettermoments: A Robust Method To Measure Line Centroids*, v1.0, Zenodo, doi:10.5281/zenodo.1419754
- Teague, R., Jankovic, M. R., Haworth, T. J., Qi, C., & Ilee, J. D. 2020, *MNRAS*, 495, 451
- Teague, R., Semenov, D., Guilloteau, S., et al. 2015, *A&A*, 574, A137
- Thi, W., van Zadelhoff, G., & van Dishoeck, E. F. 2004, *A&A*, 425, 955
- Tilling, I., Woitke, P., Meeus, G., et al. 2012, *A&A*, 538, A20
- Tsukagoshi, T., Momose, M., Kitamura, Y., et al. 2019, *ApJ*, 871, 5
- van der Marel, N., van Dishoeck, E. F., Bruderer, S., et al. 2016, *A&A*, 585, A58
- van der Marel, N., Williams, J. P., & Bruderer, S. 2018, *ApJL*, 867, L14
- van der Walt, S., Colbert, S. C., & Varoquaux, G. 2011, *CSE*, 13, 22
- van Dishoeck, E. F., Jonkheid, B., & van Hemert, M. C. 2006, *FaDi*, 133, 231
- van Dishoeck, E. F., Kristensen, L. E., Benz, A. O., et al. 2011, *PASP*, 123, 138
- van Kempen, T. A., Doty, S. D., van Dishoeck, E. F., Hogerheijde, M. R., & Jørgensen, J. K. 2008, *A&A*, 487, 975
- van 't Hoff, M. L. R., Harsono, D., Tobin, J. J., et al. 2020, *ApJ*, 901, 166
- van 't Hoff, M. L. R., Persson, M. V., Harsono, D., et al. 2018a, *A&A*, 613, A29
- van 't Hoff, M. L. R., Tobin, J. J., Trapman, L., et al. 2018b, *ApJL*, 864, L23
- van 't Hoff, M. L. R., Walsh, C., Kama, M., Facchini, S., & van Dishoeck, E. F. 2017, *A&A*, 599, A101
- van Terwisga, S. E., van Dishoeck, E. F., Cazzoletti, P., et al. 2019, *A&A*, 623, A150
- van Zadelhoff, G., van Dishoeck, E. F., Thi, W., & Blake, G. A. 2001, *A&A*, 377, 566
- Varga, J., Hogerheijde, M., van Boekel, R., et al. 2021, *A&A*, 647, A56
- Visser, R., Bergin, E. A., & Jørgensen, J. K. 2015, *A&A*, 577, A102
- Wada, K., Tanaka, H., Okuzumi, S., et al. 2013, *A&A*, 559, A62
- Wakelam, V., Herbst, E., Loison, J.-C., et al. 2012, *ApJS*, 199, 21
- Wakelam, V., Loison, J. C., Mereau, R., & Ruaud, M. 2017, *MolAs*, 6, 22
- Walsh, C., Loomis, R. A., Öberg, K. I., et al. 2016, *ApJL*, 823, L10
- Walsh, C., Millar, T. J., & Nomura, H. 2010, *ApJ*, 722, 1607
- Walsh, C., Millar, T. J., Nomura, H., et al. 2014, *A&A*, 563, A33
- Wang, J. J., Vigan, A., Lacour, S., et al. 2021, *AJ*, 161, 148
- Weidenschilling, S. J., & Cuzzi, J. N. 1993, in *Protostars and Planets III*, ed. E. H. Levy & J. I. Lunine (Tucson, AZ: Univ. Arizona Press), 1031
- Weintraub, D. A., Sandell, G., & Duncan, W. D. 1989, *ApJL*, 340, L69
- Whipple, F. L. 1972, in *Proc. Nobel Symp. 21, From Plasma to Planet*, ed. A. Elvius (New York: Wiley Interscience), 211
- Wichittanakom, C., Oudmaijer, R. D., Fairlamb, J. R., et al. 2020, *MNRAS*, 493, 234
- Willacy, K. 2007, *ApJ*, 660, 441
- Willacy, K., & Woods, P. M. 2009, *ApJ*, 703, 479
- Williams, J. P., & Best, W. M. J. 2014, *ApJ*, 788, 59
- Woitke, P., Kamp, I., & Thi, W. F. 2009, *A&A*, 501, 383
- Woitke, P., Min, M., Pinte, C., et al. 2016, *A&A*, 586, A103
- Yu, M., Evans, N. J., II, Dodson-Robinson, S. E., Willacy, K., & Turner, N. J. 2017, *ApJ*, 850, 169
- Zhang, K., Booth, A. S., Law, C. J., et al. 2021, *ApJS*, 257, 5
- Zhang, K., Bergin, E. A., Blake, G. A., Cleaves, L. I., & Schwarz, K. R. 2017, *NatAs*, 1, 0130
- Zhang, K., Bergin, E. A., Schwarz, K., Krijt, S., & Ciesla, F. 2019, *ApJ*, 883, 98
- Zhang, K., Bosman, A. D., & Bergin, E. A. 2020, *ApJL*, 891, L16
- Zhang, S., Zhu, Z., Huang, J., et al. 2018, *ApJL*, 869, L47